UNIVERSITA' DEGLI STUDI DI PARMA

Dottorato di Ricerca in Scienza e Tecnologia dei Materiali Innovativi

Ciclo XXVII (2012-2014)

ADVANCED TRANSMISSION ELECTRON MICROSCOPY ON NANOSTRUCTURED MAGNETIC MATERIALS

COORDINATORE:
Prof. ENRICO DALCANALE

SUPERVISOR:
Dr. LUCIA NASI

TUTOR:
Dr. GIANCARLO SALVIATI

DOTTORANDO:
MARCO CAMPANINI

March 2015

To my parents Fiorella and Antonio

Table of Contents

Introduction

One of the greatest challenges in materials science and engineering is unquestionably the research of new smart materials able to perform multitasking operations exploitable in a wide range of innovative applications, keeping a simple and clever design.

In the last twenty years, the advent of nanostructured materials has represented a great revolution covering all the branches of materials science and involving materials for electronics and photonics, materials for energy storage and harvesting, materials for sensors and healthcare. Nanostructured materials are systems in which at least one of the dimensions is reduced down to the nanometre scale, with typical lengths ranging from a few to tens nanometres.

The reduction of lateral size can profoundly affect the properties of the well-known materials commonly employed in their bulk form, opening new

possibility and perspectives never thought before, in many technological contexts. In particular, the effect of dimensionality reduction is to establish a new regime that, thanks to the lateral confinement, shows unique properties different from the ones of continuous bulk and discrete atoms.

These materials are gathering a lot of interest by the entire scientific community since the understanding of the mechanisms that rule the variation of their properties with the scaling of the dimensionality can permit a significant step forward in the comprehension of physical phenomena at the nanoscale.

Today, more than ever, a great expectation has been focused on the breakthrough of nanostructured materials, which could be easily implemented in common technological systems and therefore quickly spread in many fields of our everyday life.

Among different kinds of nanostructured materials, magnetic thin films and nanoparticles are very promising since the magnetism they exhibit is strongly affected by the dimensionality. In magnetic thin films, for example, the properties can change drastically for effect of the confinement and can be modified by changing the thickness; in nanoparticles, the reduced dimensionality, as well as the shape and size, determine the properties of the superparamagnetic regime induced by the lateral confinement.

A direct consequence of the low dimensionality and the complex behaviours of these nanostructured systems is that sophisticated characterizations techniques are requested to investigate the materials properties with a spatial resolution comparable or higher than their typical dimensions. State of the art transmission electron microscopes are able to accomplish these requirements, offering the inimitable capability of joining structural and morphological characterizations with analytical and magnetic characterizations at a very high spatial resolution, a combination not achievable by any other characterization technique.

This doctoral thesis is focalized on the employment of advanced transmission electron microscopy techniques in the investigation of the

properties of nanostructured magnetic materials with different dimensionality, i.e. magnetic nanoparticles and magnetic thin films. In particular, advanced transmission electron microscopy techniques are successfully employed to investigate the structural, morphological and magnetic properties of magnetite nanoparticles, which are very promising in the field of biomedicine, and to study the complex relationship between microstructure and magnetism in Ni_2MnGa shape memory alloy thin films, that represent the best candidates for new classes of actuators and energy harvesting systems. Moreover, transmission electron microscopy is successfully employed to study the structural, morphological and magnetic properties of a novel class of laterally confined nanostructures, obtained by reducing the dimensionality of martensitic thin films.

In Chapter 1, a description of the main topics involved in this doctoral work is presented. In particular, the materials and the experimental characterization techniques are introduced giving the most important tools necessary to the comprehension of the experimental results. In Chapter 2 the experimental results obtained on magnetite nanoparticles are discussed, focusing the attention on the effects of magnetic dipolar interactions on the performance of the nanoparticles as hyperthermic mediators. In Chapter 3 the results achieved in the study of martensitic microstructure of Ni_2MnGa thin films is presented and a model to describe the selective twin variants formation is proposed. In Chapter 4 a multi-scale investigation on Ni_2MnGa thin films displaying magnetic induced twin variants reorientation is carried out to correlate the material properties at the macroscopic scale to the structure and magnetism at the nanoscale. In Chapter 5, the effects of the lateral confinement on the structure and magnetism of the Ni_2MnGa martensitic phase are for the first time explored in the study of a new class of nanostructured materials, i.e. Ni_2MnGa nano-disks. The investigation is achieved by combining different transmission electron microscopy techniques and the actuation mechanisms that survive at the dimensionality reduction are studied.

1 Materials and methods

1.1 Introduction

In this Chapter, the materials investigated in this work and the experimental techniques employed in the characterization of the samples are presented and described.

In the first part of the Chapter an overview on the investigated materials is given. In particular, in Section 1.2 the structural and magnetic properties of the magnetite as well as the peculiar characteristics of magnetite nanoparticles are described. In Section 1.3, the main aspects related to the Ni_2MnGa shape memory alloy are discussed, giving basic information about its structure and magnetism. For both the materials some selected examples of promising applications are also briefly described.

In the second part of this Chapter, the main characterization techniques

employed for the realization of this doctoral thesis will be presented, focusing the attention to transmission electron microscopy (TEM), which represents the most widely used characterization technique. The structural, morphological and magnetic characterizations of the samples described in this work have been carried out combining different and complementary techniques, which consent to obtain information at different scale lengths. In particular, TEM experiments have been performed to characterize the crystal structure and the microstructural orientations, supported by X-ray diffraction (XRD). Moreover, the employment of analytical TEM techniques permits to obtain compositional information on the investigated materials.

The study of the morphological properties on a large scale has been conducted by means of atomic force microscopy (AFM). In order to characterize the magnetic properties of the samples from macro to micro/nanoscale, a combination of complementary techniques was employed. In particular, besides conventional magnetic characterizations, magnetic force microscopy (MFM) and electron holographic techniques permit to achieve a deep insight into the magnetic properties at a very fine scale.

In Section 1.4 the principles at the base of most common transmission electron microscopy techniques are briefly introduced, while a more detailed description of the less common electron holographic techniques is presented, with the aim to give to the readers the basic tools to comprehend the discussion of the experimental results. In Section 1.5, an overview of the other characterization techniques employed as complementary tools to transmission electron microscopy is presented. Finally, at the end of the Chapter, a quick description of the instrumental equipments employed to perform the different characterizations is given.

1.2 Magnetite nanoparticles

In the last decade a growing interest has been devoted to magnetic nanoparticles (NPs) for their peculiar properties which differ from the bulk ones and that can be exploited in many application fields, like nanomedicine [1-3], sensors [4-6] and magnetic recording [7-9].

Magnetic NPs, indeed, represent a very important class of nanostructured materials showing a strong size-dependent magnetic behaviour, which leads to remarkably different magnetic properties depending on their size and morphology. The superparamagnetic regime, in particular, is of fundamental importance for the biomedical applications in which stable colloidal suspensions are required in order to not compromise the cellular viability. This regime, which arises in magnetic NPs with size smaller than the critical value above which the magnetic moment of each particle is blocked, represents on the contrary one of the most limiting factors to the increase of the magnetic recording density.

Among biomedical applications of magnetic NPs, the most promising uses are as contrast agents to enhance the magnetic resonance imaging (MRI) signal [10-12], as transport vectors for drug delivery [13-15] and as heating agents in hyperthermia treatments [16-18].

In the superparamagnetic regime the magnetic NPs don't show a net magnetization if no external magnetic field is applied. Under an external magnetic field, on the contrary, the magnetic signal that the NPs are able to generate is strong enough to be easily detectable and a magnetic field gradient can therefore be exploited to drive the magnetic NPs toward a specific target.

Besides the request on the particle size, that has to be smaller enough to permit the establishing of the superparamagnetic regime, another important requirement for magnetic NPs concerns the size distribution of the NPS suspension: a monodispersed system, in fact, is highly preferable since it assures that the physical properties of each particle of the system are the

same; this last requirement is of particular importance, for example, in the imaging techniques, in which artefacts due to system inhomogeneity are preferably to be avoided, or in the drug delivery, in which an accurate control of the drug release position is necessary to avoid unpleasant side effects. Furthermore, in order to have a better performance under an applied magnetic field, a high value of saturation magnetization is required. The surface of the NPs can be functionalized with organic molecules in order to increase the biocompatibility or promote a selective interaction with other biological entities of relevant interest in the fields of magnetic separation [19, 20] and bio-sensoring [21, 22].

Among different materials, iron oxides NPs are very interesting for biomedical applications. In particular, magnetite NPs are very promising thanks to the magnetite ferrimagnetic behaviour with a high value of saturation magnetization (≈ 80 A/m) and its biocompatibility.

In the first part of this Section the peculiar properties of magnetite will be described, highlighting the structural aspects that are at the origin of the magnetic properties. Then, a concise description of the superparamagnetism will be provided. Finally, the most important biomedical applications of magnetic NPs will be described.

1.2.1 Crystal structure and magnetic properties

The magnetite, whose composition is Fe_3O_4, has an inverse spinel crystal structure in which 32 O^{2-} ions are organized in a cubic close packing (ccp) structure along the [111] direction of the unit cell. The magnetite lattice parameter is a = 0.8369 nm and the spatial group of crystal structure is Fd3m [23]. The O^{2-} ions packing gives rise to two different interstitial sites in the magnetite crystal structure characterized by two different symmetries, which are tetrahedral and octahedral respectively. The tetrahedral (A) sites are occupied by Fe^{3+} ions, while the octahedral (B) sites are occupied by the remaining amount of Fe^{3+} ions together with Fe^{2+} ones, randomly distributed.

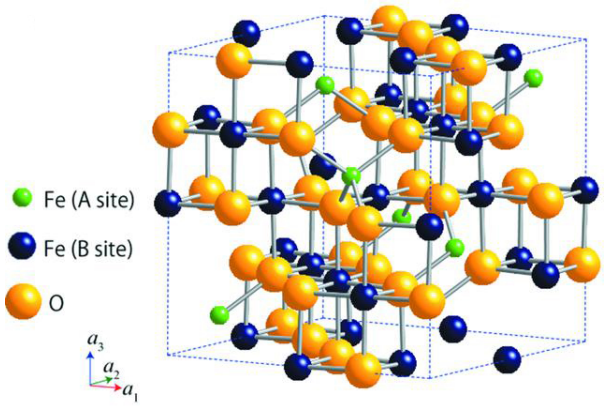

Fig. 1.1 Inverse spinel crystal structure of magnetite, where tetrahedral (A) and octahedral (B) interstitial sites are drawn in green and blue respectively. (From [24]).

The inverse spinel structure of magnetite can therefore be written as $Y[XY]O_4$, where X = Fe^{2+}, Y = Fe^{3+} and the brackets denote octahedral sites. In the stoichiometric magnetite the Fe^{3+} ions occupy entirely the smaller tetrahedral sites and half of the octahedral ones [23]. In Fig. 1.1 a scheme of the inverse spinel structure of magnetite is shown, where the O^{2-} ions are drawn in yellow while the tetrahedral and octahedral interstitial sites are drown in green and blue respectively.

Below the Curie temperature T_C = 850 K [25], the magnetite is ferrimagnetic. The two different sites of the structure, the tetrahedral (A) sites occupied by Fe^{3+} ions and the octahedral (B) sites occupied by both Fe^{3+} and Fe^{2+} ions, form two interpenetrated magnetic sub-lattices. The coupling between ions in each sub-lattice (A-A and B-B coupling) is ferromagnetic; however, thanks to a strong antiferromagnetic interaction among the spins in A and B sites, the coupling between the two different sub-lattices (A-B coupling) is antiferromagnetic. This antiferromagnetic coupling between the two sub-lattices gives rise to the global ferrimagnetic behaviour of magnetite. A schematic representation of the magnetic ordering in magnetite is shown in Fig. 1.2a. The easy magnetization axes of magnetite correspond to the 8 equivalent [111] directions of the crystal structure (Fig. 1.2b).

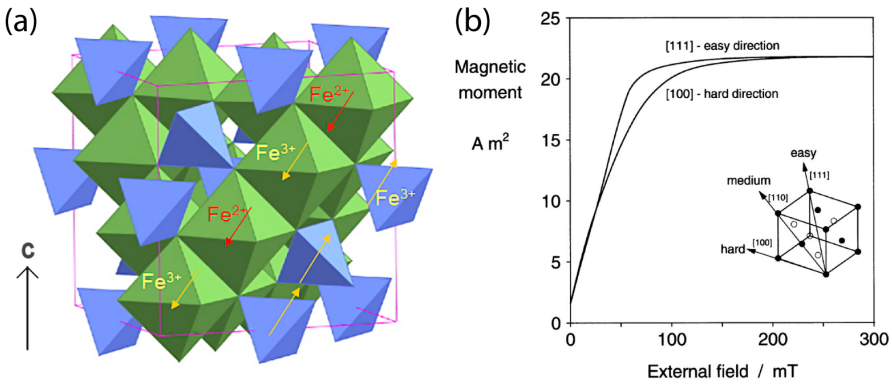

Fig. 1.2 (a) Magnetic coupling between two A and B sub-lattices in magnetite; (b) magnetization curves for a magnetite single crystal applying a magnetic field along the [100] and [111] crystallographic directions. (From [23])

1.2.2 Superparamagnetic regime

The reduction in the dimensionality of magnetic particles down to the nanometre scale can strongly affect the magnetic properties displayed by the particles. In fact, below a critical value of the particle size (usually in the range from few to tens nanometres) depending on the material, the magnetization of the particles is no more fixed along well-defined crystallographic orientations determined by the crystalline or shape anisotropy, since the thermal energy can be high enough to produce a rotation of the particles magnetization between different stable orientations.

The thermal fluctuations of the magnetic moment of a monodomain particle were described for the first time by Nèel [26]. In the case of non-interacting particles and in absence of magnetic anisotropy the moment of each particle, which can be ascribed to a giant moment equal to the sum of all the magnetic moments of the atoms within the particle, is oriented randomly. The described situation is completely similar to the case of a classical paramagnet, with the remarkable difference that the considered system must be described taking into account the moments of the particles instead of the atomic ones: for this reason the effect is called *superparamagnetism* and the saturation magnetization can be achieved at ordinary fields.

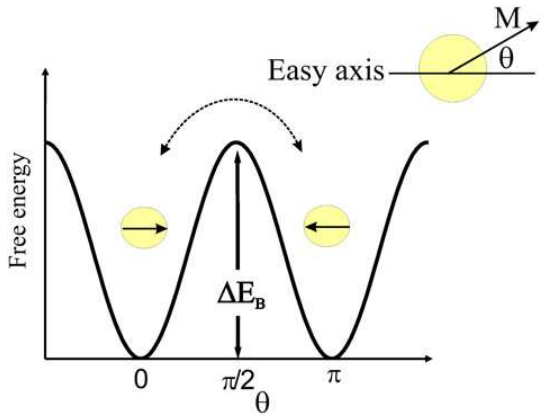

Fig. 1.3 Double-well potential model for the free energy of a superparamagnetic NP (from [27]).

The magnetic anisotropy induces preferential orientations among all the possible orientations of the magnetization of the NPs. In the simplest possible geometry, corresponding to the uniaxial anisotropy, only one preferential orientation exists for each NP; in this case, the energy of the system can be described by a double-well potential (Fig. 1.3) with two energy minima corresponding to two stable antiparallel orientations of the NP moment separated by an energy barrier $\Delta E_B = KV$, corresponding to the anisotropy energy [28]. At a given temperature T, the average time necessary to overcome this barrier and observe a reversal in the magnetization direction is called *Néel relaxion time* (τ) and is given by the Nèel-Arrhenius equation [29, 30]:

$$\tau = \tau_0 \exp(KV / k_B T) \qquad (1.1)$$

where τ_0 is a time characteristic of the probed material ($\tau_0 = 10^{-9} - 10^{-12}$ *s*) and k_B is the Boltzmann constant.

The magnetic characterization of NPs in the superparamagnetic state, however, does not only depend on the temperature T and the energy barrier ΔE_B. Each experimental characterization technique, in fact, has its own characteristic measurement time, τ_m. Depending on the measurement time, two different situations can occur and correspondingly two different behaviours can be visualized in the magnetization curve:

(i) $\tau_m << \tau$: the average time in which the jumps of the magnetization between the two antiparallel directions occur is larger than the measurement time. In this case the magnetic moment is "blocked" and the magnetic loop shows a hysteresis. This regime is called *blocked momentum regime*.

(ii) $\tau_m >> \tau$: the average time between the magnetization jumps is smaller than the measurement time; this implies that during the typical time needed to perform the experiment quick and spontaneous flips of the magnetization occur. As long as no external field is applied, a time-averaged zero moment is measured. This regime is the already mentioned *superparamagnetism*.

The temperature value at which the magnetic relaxation time is equal to the measurement time ($\tau = \tau_m$) is defined as the blocking temperature T_B:

$$T_B = \frac{KV}{k_B \ln(\tau_m / \tau_0)} \qquad (1.2)$$

For a given characterization technique, T_B permits therefore to distinguish between the blocked and the superparamagnetic regime displayed respectively in the temperature ranges $T < T_B$ and $T > T_B$. The two described situations are schematized in Fig. 1.4a and b, respectively.

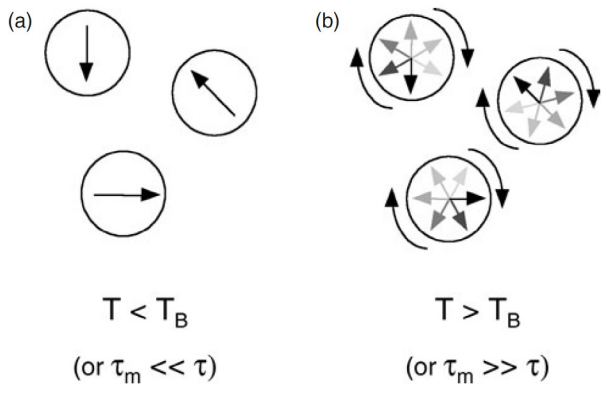

Fig. 1.4 Schematic representation of the two possible regimes for small superparamagnetic NPs: (a) blocked state, (b) superparamagnetic state (from [31]).

If an external magnetic field *H* is applied to the superparamagnetic NPs, their magnetic moments start to align along the applied field, similarly to what happen for paramagnetic materials. In particular, assuming that the thermal fluctuation energy is higher than the anisotropy energy, the orientation of the easy magnetization axes does not play any role in the magnetization process and, similarly to the case of the classic paramagnetic behaviour, the magnetization curve *M(H)* for an assembly of superparamagnetic NPs can be described by the Langevin curve:

$$M(H) \approx n\mu L(x) = n\mu\left[\coth\left(x\right) - \frac{1}{x}\right] \qquad (1.3)$$

where $x = (\mu_0 mH / k_B T)$, n is the suspension concentration, m the magnetic moment of each NP and μ_0 is the magnetic permeability of the vacuum. The salient properties of the magnetization curves attributable to the superparamagnetic regime are zero coercivity, zero remanence and the existence of a blocking temperature T_B.

If the NPs are dispersed in a solvent and form a colloidal suspension, another mechanism for the magnetization relaxation has to be taken into consideration, in addition to the Néel relaxation. In fact, a *Brownian relaxation* due to the viscous rotation of the particles inside the solvent can occur. The characteristic time of this relaxation process is given by:

$$\tau_B = \frac{3\eta V}{k_B T} \qquad (1.4)$$

and depends on the volume of particles V, the viscosity of the solvent η and the temperature T of the colloidal suspension.

The global relaxation rate for a colloidal suspension of magnetic NPs is therefore given by:

$$\frac{1}{\tau} = \frac{1}{\tau_N} + \frac{1}{\tau_B} \qquad (1.5)$$

where τ is the global relaxation time for the colloidal suspension and τ_N and τ_B are Néel and Brownian relaxation times, respectively. In Fig. 1.5 the trends of

the Néel, Brownian and global relaxation times for magnetite NPs are shown at a given temperature [32]. Thanks to a different dependence of the Néel and Brownian relaxation times on the particles volume, the behaviour of small magnetic NPs is governed by the Néel relaxation while a viscous rotation of the particles is the dominant process in the relaxation of big magnetic NPs. However, the critical size at which the dominant relaxation mechanism switches from the Nèel to the Brownian one depends in general on the material (since different materials are characterized by different anisotropy energies), the temperature and the viscosity of the solvent.

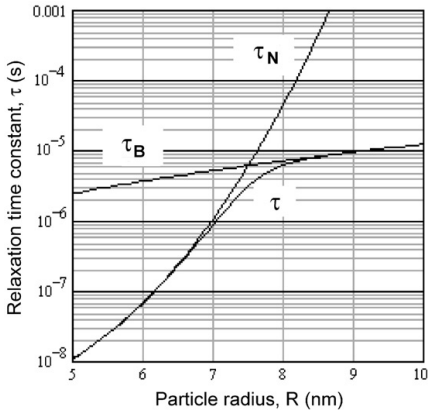

Fig. 1.5 Typical Néel and Brownian relaxation times, as a function of particle size, for magnetite NPs. (From [32]).

1.2.3 An overview of biomedical applications of magnetic NPs

1.2.3.1 Magnetic Separation

A challenging request, crossing many fields related to biomedicine, concerns the isolation of entities of interest from the other constituents of the complex system they are dispersed in. An efficient and promising method to achieve a very controlled and reliable separation is the *magnetic separation* process.

In fact, thanks to the possibility to functionalize the surface of magnetic NPs with small molecules able to selectively interact with the entities of interest, it

is possible to make the particles effective in the isolation of the requested entities from complex biological mediums. This very promising method relies on the capability of properly tailoring the particles sizes in order to make them comparable or even smaller than the typical biological entities.

The magnetic separation method is performed by a two steps process: the first step consists in marking the biological entities of interest by the magnetic NPs properly functionalized; then the marked objects can be isolated by applying a magnetic field gradient and the supernatant can be removed. The magnetic force that must be applied has to overcome the hydrodynamic shear force given by:

$$F_h = 6\pi\eta R\Delta v \tag{1.6}$$

where η is the medium viscosity, R is the NPs radius, v is the difference between the velocities of the medium and the marked entities within it. In Fig. 1.6, the two most common methods of magnetic separation are schematized: the process of magnetic separation in suspension permits to isolate the marked entities (black circles) from the medium by removing the supernatant, after the precipitation of the NPs (Fig. 1.6a); the magnetic separation in flow permits to isolate the marked entities which are caught by the applied magnetic field (Fig. 1.6b).

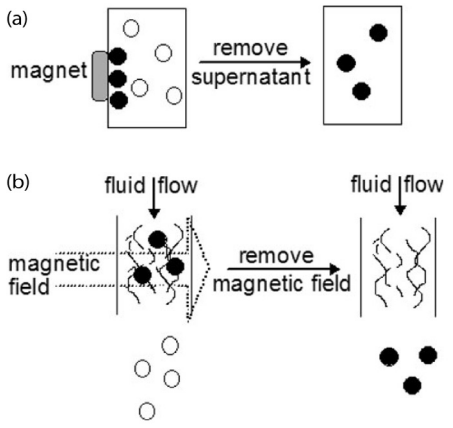

Fig. 1.6 Conventional magnetic separation methods: (a) in suspension, (b) in flow (From [31]).

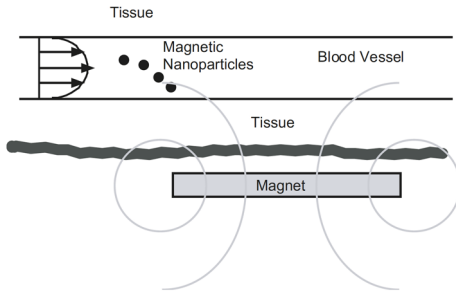

Fig. 1.7 Schematic representation of the magnetically driven drug delivery: the NPs travel within the circulatory system driven by the external magnetic field, reaching the target area (From [31]).

1.2.3.2 Drug delivery

Another challenging aspect to deal with in biomedical applications and, in particular, in cancer treatment is the research of new effective drugs able to destroy cancer cells avoiding heavy side effects on the patient. At this purpose, magnetic NPs properly functionalized can be used as carrying vectors to deliver the drugs in a well-defined target region within the body. The possibility of finely control the drug release in the desired target region permits to avoid the large-scale side effects and, at the same time, to reduce the total amount of drug used to efficiently treat the disease.

In order to make the magnetically-driven drug delivery possible, the magnetic vectors need to be small and highly stable against aggregation: in this way they can be injected into the circulatory system and, if an external field gradient is applied, reach the target area travelling within the blood vessels (Fig. 1.7).

1.2.3.3 Contrast agents in MRI

One of the most promising applications of magnetic NPs is in the field of the diagnostics; in particular, they can be employed as a contrast agent in imaging techniques.

The magnetic resonance imaging technique is based on the employment of a large magnetic field able to align the moments of hydrogen nuclei in the

water molecules. The magnetic moment of a proton is very small; however, since in a mm^3 of water there are about $7x10^{19}$ protons, the signal they are able to generate under a large applied magnetic field $B_0 \approx 1$ T is easy to detect by a resonant absorption experiment (Fig. 1.8).

In particular, applying an oscillating magnetic field with a frequency ω_0 (corresponding to the Larmor frequency for the precession of the moment *m* of the proton around B_0) in the perpendicular direction with respect to B_0, it is possible to excite the moments precession in the plane perpendicular to B_0, due to a resonant effect (Fig. 1.8a and b). When the oscillating magnetic field is removed, the longitudinal and transversal relaxations of the moments can be studied. If the static magnetic field B_0 is applied along the z direction, the signals generated by the longitudinal and transversal relaxations are respectively expressed by:

$$m_z = m\left(1 - e^{-t/T_1}\right) \tag{1.7}$$

$$m_{xy} = m\sin(\omega_0 t + \phi)\, e^{-t/T_2} \tag{1.8}$$

where T_1 and T_2 are the longitudinal and transversal relaxation times respectively and ϕ is the phase. The curves describing the m_{xy} and m_z behaviour as a function of the time (after the removal of the applied oscillating field) are reported in Fig. 1.8c and d, respectively. The longitudinal relaxation (T_1) is related to the loss of energy that flows from the system to the surrounding, and is a measure of the dipolar coupling between the protons moments and the other moments in the surrounding tissues; the transversal relaxation (T_2) is rapid and is related to the loss of phase coherence due to the magnetic interaction between the protons. Local inhomogeneity in the magnetic field can produce a shortening of the transversal relaxation time, whose value changes from T_2 to T_2^*:

$$\frac{1}{T_2^*} = \frac{1}{T_2} + \gamma\frac{\Delta B_0}{2} \tag{1.9}$$

where ΔB_0 represents the local variation of the magnetic field.

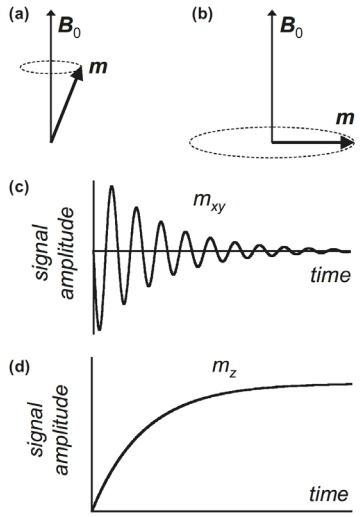

Fig. 1.8 Schematic representation of the basic concepts concerning the origin of MRI contrast: (a) precession of the magnetic moments around the applied field B_0; (b) precession of the moments in the plane perpendicular to B_0, due to the oscillating field perpendicular to B_0; time-dependent relaxations of the magnetic moments, in the (c) transversal and (d) longitudinal directions (From [31]).

Superparamagnetic NPs can reach saturation at ordinary fields, comparable to the typical ones used in an MRI apparatus, and can generate local fields that produce a reduction of T_2. Moreover, thanks to their reduced size the NPs (with diameters in the range 5-20 nm) can travel within blood vessels and can be captured by the endothelial system. Since the endothelial system of cancer cells is not so efficient as the one of healthy cells, the NPs amount gathered by the different cellular tissues is strongly different. Hence, the contrast agent does not alter the relaxation times of unhealthy cell, which only gather a low amount of NPs. In the images, a contrast between healthy and unhealthy tissues is therefore observable and the disease can be localized.

1.2.3.4 Magnetic hyperthermia

Among the many possible therapeutic approaches of cancer tissues, magnetic NPs can act as heat mediators in the *hyperthermia* treatment. In fact, the NPs can promote a heat transfer when a radio frequency AC magnetic field is applied. In this way, the local temperature of the tissue containing NPs can

be heated up to 42 °C for a clinical treatment time of 30 min. Since the cells constituting the diseased tissue are more sensitive to heat than healthy ones, this treatment is effective in causing a selective cancer cells death, while the healthy ones are not affected.

If we consider multi-domains magnetic NPs, the heat generation has its origin in the hysteresis losses, which are proportional to the area of the hysteresis loop and are related to magnetic domains wall movement. The amount of heat generated per unit volume P_{FM} is given by:

$$P_{FM} = \mu_0 f \oint H\,dM \tag{1.10}$$

where f is the frequency and the integral gives the area of the hysteresis loop. For ferromagnetic particles whose size is significantly larger the superparamagnetic critical size, an approximate value of P_{FM} can be estimated by quasi-static measurements of the hysteresis loop.

On the contrary, as previously described in Section 1.2.2, if no external magnetic field is applied on a colloidal suspension of superparamagnetic NP the relaxation of their magnetic moments can occur by both the Néel and Brownian relaxations, whose characteristic times were given in Eq. 1.1 and 1.4, respectively. In the most general case both the mechanisms are present (Eq. 1.5), but the global behaviour is governed by the faster relaxation mechanism. Within the validity of the linear response theory (LRT), e.g. for low-amplitude fields, the power loss density P (in Wm^{-3}) for an assembly of randomly oriented magnetic NPs is given by [33]:

$$P = 2\mu_0 \pi\, \chi''(t) f\, H_0^2 = \frac{\mu_0^2 M_s^2 V H_0^2}{3k_B T \tau} \cdot \frac{(2\pi f \tau)^2}{1+(2\pi f \tau)^2} \tag{1.11}$$

where χ'' is the imaginary part of the susceptibility, H_0 and f are the applied AC field amplitude and frequency respectively, M_s is the saturation magnetization, V is the particles volume, T is the temperature, τ is the global relaxation time, μ_0 is the vacuum permeability and k_B is the Boltzmann constant. The *specific power absorption* (SPA) is defined as:

$$SPA = P / \rho \tag{1.12}$$

where ρ is the mean density of the particles and the SPA value is expressed in [Wg^{-1}]. From the above equations, we can conclude that an optimum particle size exists that yields to a maximum heating, which depends also on the applied magnetic field intensity and frequency. This optimal size also depends on the material through the anisotropy constant.

Another possible heating mechanism is related to eddy currents. In fact, under an applied oscillating magnetic field, eddy currents can be generated on the particles surface. The heat production for this mechanism is related to the power dissipation due to the resistance of the material. These currents, however, depend on the degree of penetration of the field into the particles. The eddy currents have been shown to be negligible for small particles (less than 100 nm in diameter), if the frequency of the alternating field is less than 10 GHz [34].

1.3 NiMnGa shape memory alloy

Magnetic shape memory (MSM) alloys are magnetoelastic multiferroic materials that exhibit both a ferromagnetic and a ferroelastic (martensitic) phase transformation and are characterized by a strong coupling between the magnetic and structural degrees of freedom [35].

The attentions devoted to MSM alloys have increased continuously since their discovery in the 1996 [36]. In particular, in the recent years the ongoing research for new active materials employable in actuation devices has focus on MSM alloys, which permit to combine macroscopic strains higher than 10% [37] with a high cycling frequency, making these materials the favourite candidate for a new generation of actuation devices and energy harvesters. In the field of machining, active piezoelectric materials commonly used in the current microsystems applications can achieve strains that are one order of magnitude smaller compared to the ones achievable by MSM alloys; nevertheless, the realization of actuation devices based on piezoelectric

materials often requires the integration of additional gear mechanisms, with a further increase of the system complexity [38]. In the field of energy harvesters, MSM alloys have exhibited a significant capability in harvesting mechanical energy by cycling the martensite variant reorientation [39, 40].

The conventional *shape memory effect* in MSM alloys is based on the thermoelastic transformation between a high temperature cubic phase, called "*austenite*", and a low temperature phase characterized by a lower symmetry, called "*martensite*", producing a change in their macroscopic shape that is reversible upon heating and cooling [41]. A remarkable property of the MSM alloys is that if the material is deformed in the martensitic phase, the original shape can be restored by heating the material to the austenitic phase.

In addition to the conventional shape memory effect, which is controlled by the temperature, other actuation mechanisms are possible in MSM alloys. In fact, thanks to the strong coupling between their magnetic and structural orders, MSM alloys are intrinsically multifunctional materials and external magnetic fields can significantly alter the structure of the martensitic phase.

In particular, applying a magnetic field it is possible to induce boundaries motion in the martensitic phase [42, 43], leading to an increase in the amount of variants with their easy magnetization axis aligned parallel to the applied magnetic field at the expense of the variants with different orientations. This effect, called "*magnetic shape memory effect*" or "*magnetic field induced reorientation*" (MIR), permits to obtain very large magnetic field induced strains in the material. Thanks to this effect strains up to 12% [37] have been observed in bulk single crystals of Ni_2MnGa, making this material a great candidate for actuation devices that are able to operate at frequency up to 250 Hz [44].

Another actuation mode in MSM alloys derives from the coupling between the crystal structure and the magnetization, but it does not involve boundaries motion. In fact, cooling down the austenitic phase under an applied magnetic field, the phase with the higher magnetic moment is the one energetically favoured. This effect produces a *magnetically induced martensite* (MIM) that can be applied for actuation in the proximity of the transformation

temperature [45, 46].

The peculiar aspects of the crystal structure and the magnetic properties of the Ni_2MnGa alloy will be described in the following Section, giving to the reader the necessary tools necessary to comprehend the analysis that will be conducted in the discussion of the experimental results on Ni_2MnGa thin films. The MIR effect, demonstrated in the Ni_2MnGa bulk single crystals, will be also briefly introduced in Section 1.3.2. In Section 1.3.3 the basic aspect related to the epitaxial growth of Ni_2MnGa alloy thin films are introduced and finally, in Section 1.3.4, few selected examples of applications of Ni_2MnGa thin films are briefly reported.

1.3.1 Crystal structure and magnetic properties

The ternary metallic compound Ni_2MnGa, commonly named Ni-Mn-Ga and in the following indicated with 'NiMnGa' for simplicity, is a Heusler alloy. The Heusler alloys, whose general formula for the stoichiometric composition is (X_2YZ), are ferromagnetic metallic alloys characterized by a $L2_1$ crystal structure [47] with Fm-3m space group, consisting in four interpenetrated face centred cubic (fcc) lattices with position (0, 0, 0,) and (½, ½, ½) for X atoms, (¼, ¼, ¼) for Y atoms and (¾, ¾, ¾) for Z atoms. A schematic representation of the $L2_1$ structure of a Heusler alloy is given in Fig. 1.9a, in which the two sub-lattices of X atoms are drawn in blue and black, while the sub-lattices of Y and Z atoms are drawn in green and the red, respectively. For the NiMnGa alloy, X = Ni, Y = Mn, Z = Ga. The lattice parameter of NiMnGa cubic cell is a = 0.5821 nm [48].

The stoichiometric alloy exhibits a ferromagnetic phase transition with a Curie temperature $T_C \approx 370$ K; at lower temperature, NiMnGa undergoes a martensitic phase transformation from the highly symmetric cubic phase, i.e. austenite, to a low symmetry phase, i.e. martensite. The martensitic phase transformation temperature (T_M) is around 210 K for the stoichiometric compound [49].

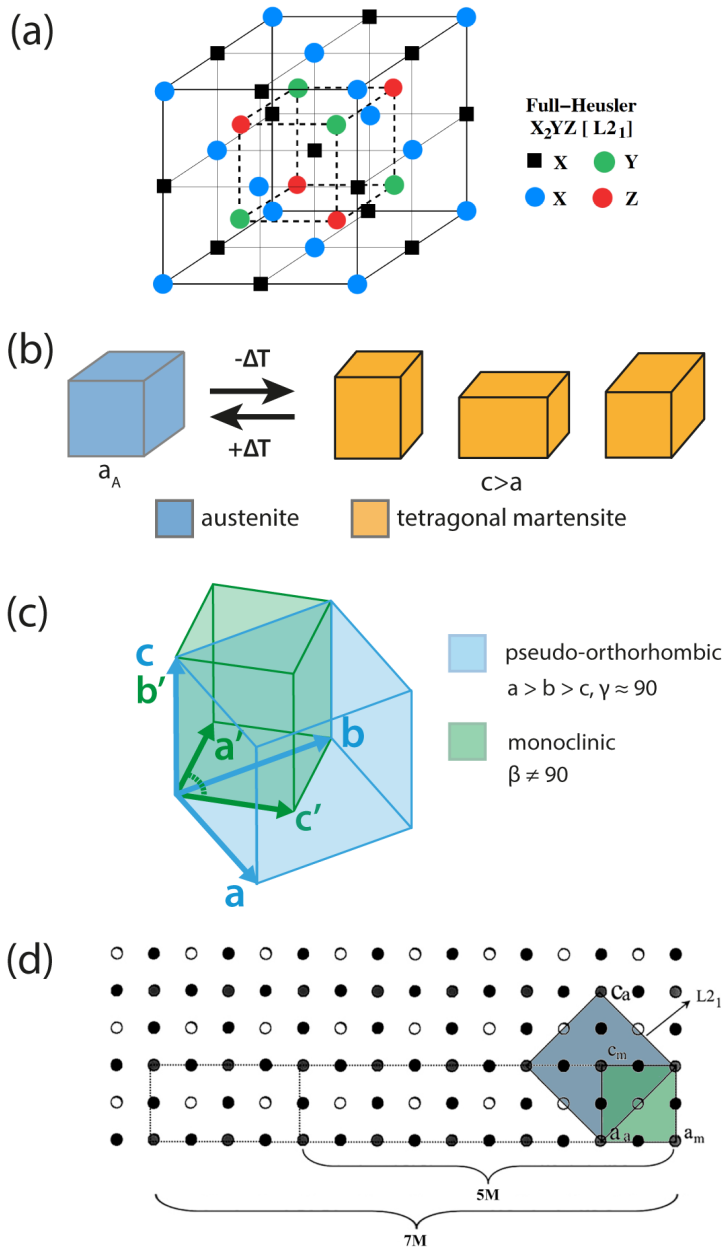

Fig. 1.9 (a) $L2_1$ cubic crystal structure of Heusler alloys (X_2YZ). For the NiMnGa alloy, X = Ni, Y = Mn, Z = Ga. (b) Tetragonal distortion of the austenitic phase. (c) Monoclinic and corresponding *pseudo*-orthorhombic cells for the distorted martensitic structure. (d) Lattice relationships between the cubic $L2_1$ (blue) and the martensitic (green) cells: the typical extent of commensurate 5M and 7M modulated lattices are also shown ((d) is adapted from [56])

However, in non-stoichiometric NiMnGa compounds the transformation temperatures as well as the observed martensitic phases are strongly dependent on the alloy's composition [50, 51].

The martensitic phase transformation is a first order displacive solid-state transition that results from a lattice distortion, the so-called Bain distortion, of the high-temperature austenitic phase into a low temperature martensitic phase. The Bain distortion is a lattice deformation that causes an expansion of the cell in one of the crystallographic directions and, correspondingly, a contraction in the two orthogonal ones, reducing the symmetry of the system from cubic to tetragonal (Fig. 1.9b). The low temperature martensite can even display additional distortions, with a further reduction of the symmetry from tetragonal to orthorhombic (the axes are distorted giving a > b > c) or monoclinic (if a monoclinic angular distortion is also observed) [52].

It is worth noting that, even in the case of the lower monoclinic symmetry, the martensitic phase is commonly described by the community working on MSM alloys by using a *pseudo-orthorhombic* setting and assuming a slight distortion of the γ angle in the orthorhombic cell with a > b > c, being this angle slightly different from 90°. The situation is schematized in Fig. 1.9c, in which the pseudo-orthorhombic cell is drawn in light blue; the monoclinic cell corresponding to this pseudo-orthorhombic cell is schematized in green. In particular, in the monoclinic setting the martensitic transformation product phase is properly described by an I-centred unit cell having two of its fundamental axes along different directions compared to the austenitic/pseudo-orthorhombic axes. In fact the a_m, b_m and c_m (in the following indicated by a', b' and c' for simplicity) monoclinic axes are parallel to the [110], [010] and [-110] directions of the pseudo-orthorhombic structure respectively, as schematized in Fig. 1.9c.

The use of a pseudo-orthorhombic cell is not strictly correct and does not reflect the real symmetry of the martensitic phase. However, it offers the great advantage to permit a direct and easy comparison between the martensitic phase and the parent austenitic phase, since it can be considered as directly

generated by the cubic phase for effect of the lattice invariant Bain distortion plus a lattice variants deformation, while maintaining its axes parallel to the austenitic ones.

Moreover, many authors have reported diffraction experiments in which additional weak reflections corresponding to satellite peaks are present, thus proving the existence of structural modulated martensitic phases. This kind of distortions are generated by an instability in the parent cubic structure that induces a shuffling of atomic layers along the martensitic c' short axis.

After Webster et al. [49], which observed a five-fold superstructure (named '5M') involving five consecutive martensitic unit cells, also other authors have reported different superstructures constituted by 5, 6, 7, 10 and 12 cells and named 5M, 6M, 7M, 10M and 12M respectively [53-55]. In Fig. 1.9d, the dashed lines draw the extension ranges on which the most common 5M and 7M modulated structures occur. Recent works have also demonstrated the occurrence of incommensurate modulated structures [56-58] in stoichiometric and non-stoichiometric NiMnGa alloys.

The peculiar property of martensites is that the high strain related to the phase transformation is accommodated at the austenite-martensite interface, the "*habit-plane*", by the formation of ferroelastic domains called "*martensitic variants*" through a lattice invariant deformation that leaves the habit-plane undistorted and un-rotated [59]. This lattice deformation can occur by introduction of defects (slip dislocations) in the crystal structure or by twinning. In the latter case, the generated martensitic variants are also called "*twin variants*".

To be suitable for the above-mentioned applications, NiMnGa alloys have to satisfy two requirements. The first request is that the martensitic phase transformation temperature must be above room temperature (RT), since only the martensitic phase displays the MSM effect. Second, a low twinning stress is necessary for the twin boundaries movement to occur at low applied magnetic fields [60]. This low twinning stress is usually achieved in the modulated martensitic phases.

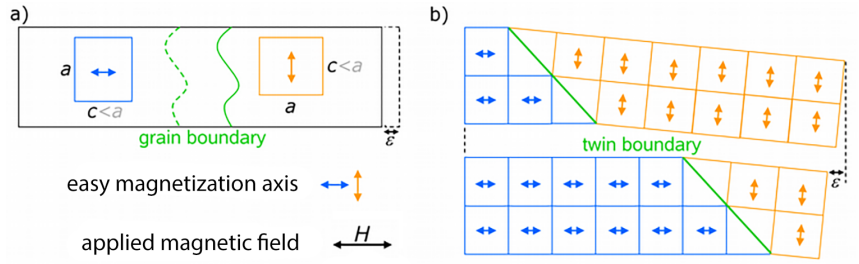

Fig. 1.10 Scheme of the MIR effect. (a) The two martensitic variants are drawn in blue and orange, respectively; the arrows give their respective easy axes. (b) When an external magnetic field is applied, the boundary moves and the amount of the blue variant increases.

1.3.2 MIR effect in bulk crystals

The strong coupling between structural and magnetic ordering is at the origin of the magnetic-induced reorientation of twin variants, which is the key effect at the base of the magnetic field induced strain.

Thanks to the high magnetic anisotropy, in bulk crystals the magnetization in the pseudo-orthorhombic structure of NiMnGa is favourably aligned along the short c axis of the unit cell, which corresponds to the b' long axis in the monoclinic setting [61]. In the tetragonal phase (c > a), an easy-plane behaviour is instead observed [62, 63]. The direct consequence of this preferential orientation is that the domains oriented with their easy magnetization axis parallel to the applied field are the most stable; the domains with their easy axis in a different orientation are in an unstable configuration and, providing that the magnetic energy across the domains boundary is higher than the mechanical energy needed for boundaries motion, a reorientation of the martensitic variants can occur [64]. The described situation is schematized in Fig. 1.10, in which two martensitic variants are drawn in blue and orange respectively. When an external magnetic field is applied, the reorientation of the variants occurs with an increase of the most stable one. In this process, a deformation of the shape is also observed. The microstructural twin variants reorientation induced by the applied magnetic field is accompanied by a large and sudden change in the magnetization.

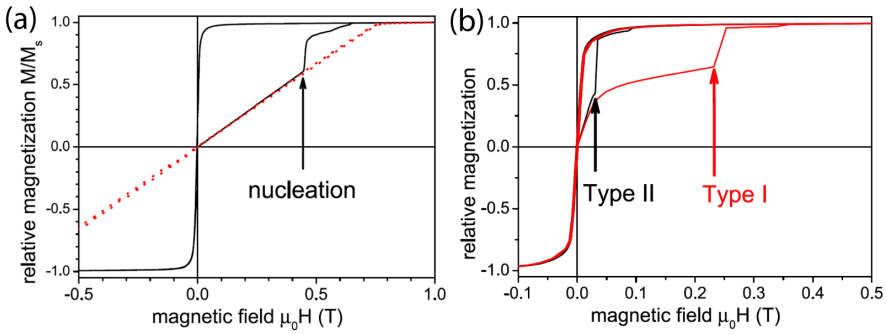

Fig. 1.11 (a) Magnetization curve for single variant samples: a curve of a sample displaying MIR effect is compared to the curve of a sample in which the MIR is not displayed. The arrows highlight the point in which the stable variant nucleate. (b) Magnetization curves for two samples displaying MIR effect but characterized by a different kind of twins: the red curve is relative to a type-I twin, the black curve is relative to a type-II twin. (From [64])

In Fig. 1.11a the magnetization curve for a single variant martensite exhibiting MIR effect is compared to the one of a martensite that does not display MIR: the nucleation of a differently oriented twin variant and the onset of the twin boundary motion are marked by a sharp increase in the magnetization of the sample displaying the MIR [64].

Recently, Straka et al. [65] showed that two different kinds of mobile twin boundaries, called type-I and type-II respectively, exist in modulated martensite. A strong difference in the twinning stresses exists for the two kinds of twins, being the twinning stress of type-II twins 10x lower than the one of type-I twins. This remarkable difference strongly affects the twin boundary mobility and, hence, the critical field values at which the MIR effect establishes. In Fig. 1.11b the magnetization curves for two samples containing just a single twin boundary but of different kinds, are shown. When a magnetic field is applied, the twin boundary can move producing a decrease of the martensitic variant with its magnetization axis oriented not parallel to the external field. The field needed to start the twin boundary motion is very different for type-I or type-II twins. In particular, the low twinning stress of type-II twin is related to the irrational character of the involved twinning plane, which does not correspond to an exact crystallographic plane, thus permitting an easier

motion of the twin boundary with respect to the rational type-I twins [64]. The typical fields values necessary to move type-II twins are usually lower than 0.2 T.

1.3.3 NiMnGa thin films: microstructure and MIR effect

In the last years, great attention has been devoted to NiMnGa thin films, since they represent the best choice for the realization of integrated devices [66]. The presence of a substrate, however, represents a strong constrain, which can significantly affect the martensitic film properties.

The most common way to prepare single crystalline NiMnGa thin films is the epitaxial growth [67] on a single crystalline substrate. NiMnGa films have been successfully grown on various substrates, e.g. GaAs(001) [68, 69], Al_2O_3(110) [70, 71], $SrTiO_3$(100) [72] and MgO(100) [73, 74]. The large variety of suitable substrates for the epitaxial growth indicates the easy adaptation of NiMnGa, due to the facility of its structure to deform in order to fit different stress conditions. In the present work, the case of MgO(100) substrate is considered.

The mismatch between the austenitic NiMnGa cell and MgO one (a_{MgO} = 0.4213 nm [75]) is 27.8% if a cube-on-cube growth is assumed. The mismatch reduces to 2.4% if the NiMnGa cell is rotated of 45° with respect to the substrate edges. This epitaxial relationship, indeed, is the one observed experimentally [74] and is schematized in Fig. 1.12. Besides the lattice misfit, also the difference of the thermal expansion coefficients between substrate and film can lead to a residual stress in the NiMnGa [76]. Since also the stress can affect the martensitic phase transformation, this stress substantially increases the martensitic transformation temperature in thin films compared to bulk samples.

During the cooling of the NiMnGa austenitic thin films, the transformation to the martensitic phase occurs at temperatures higher than RT. Since the austenite orientation is fixed by the epitaxial constrains, the tetragonal or orthorhombic phase (we can neglect for a while the monoclinic distortion that

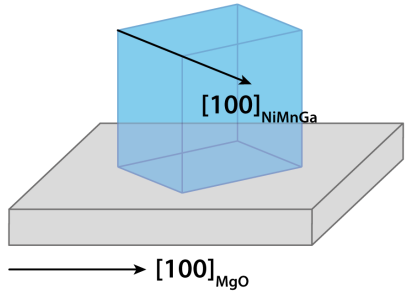

Fig. 1.12 (a) Scheme of the epitaxial relationship for the cubic cell of NiMnGa austenite on MgO substrate.

can be ascribed as a further slight distortion of the orthorhombic phase), has to adapt to this orientation. The direct effect of this requirement is that a complex martensitic microstructure constituted by well-defined orientations of twinning planes is generated in the epitaxial thin films. In particular, two microstructures are commonly observed in NiMnGa martensitic thin films. These two different microstructures are characterized by different geometries of the twinning planes, which intersect the film surface at 90° and 45° with respect to the [100] direction of MgO (Fig. 1.13a and b) and called in the following "*90° twinning planes*" and "*45° twinning planes*". The twin variants they generate will be called "*90° lamellae*" and "*45° lamellae*", respectively.

Usually, in martensitic thin films a complex microstructure generated by the co-presence of 90° and 45° lamellae is observed. 90° lamellae can be oriented along both the equivalent [100] and [010] directions of the MgO substrate, while 45° lamellae along both [110] and [1-10] directions of MgO. The exemplificative scheme in Fig. 1.13c represents a portion of a film displaying 90° lamellae oriented along both [100] and [010] MgO directions and 45° lamellae only along [110] direction; the portions of the film constituted by the same kind of martensitic lamellae and with the same orientation with respect the reference system (given by the principal directions of the MgO substrate), are called "*twin plates*". By using the introduced nomenclature, the morphological,

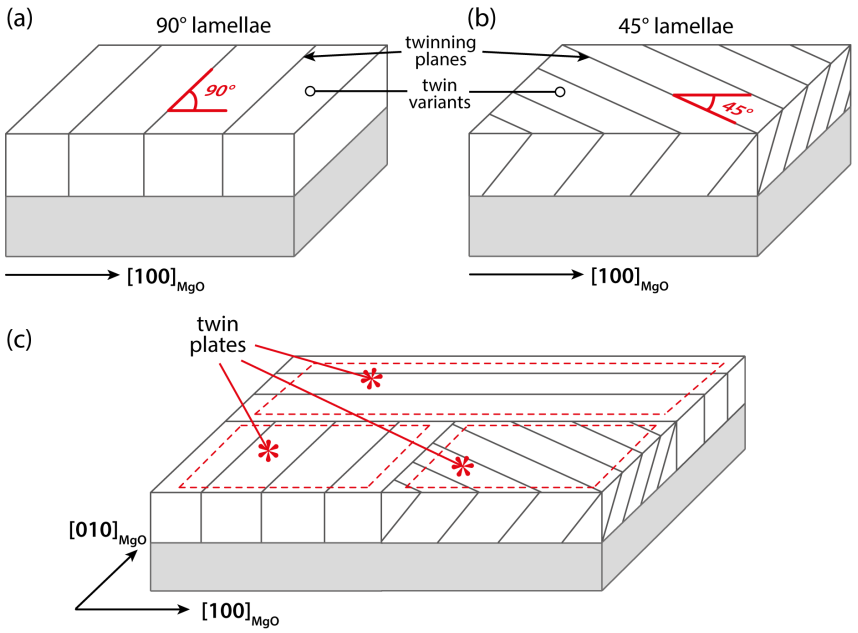

Fig. 1.13 Typical morphologies observed in NiMnGa thin films, showing 90° (a) and 45° (b) lamellae (the angular values are expressed with respect to the [100] MgO). (c) Example of complex morphology like the typical ones displayed by the martensitic films, usually showing the presence of differently oriented twin plates constituted by different twin variants.

structural and magnetic properties of the martensitic phase will be correlated to the martensitic twin plates and twin variants in the Chapter 3, 4 and 5, in which experimental results on martensitic thin films and nano-disks will be discussed.

As already described in the previous Sections, the relative stabilities of differently oriented martensitic variants under an applied magnetic field can induce the variant reorientation, with an increase of the variants with their easy magnetization axis oriented parallel to the external magnetic field. In thin films, the MIR effect has been observed by means of magnetic measurements that show the same features typically displayed for the MIR effect in bulk crystals (Section 1.3.2). However, in thin films the MIR effect has to occur preserving the film shape, because of the strong epitaxial constraints. Hence, the MIR effect in thin films has to happen without any evident change in the

macroscopic film size.

The effective employment of the NiMnGa thin films for the realization of actuation devices therefore strongly relies on the release of the film from the epitaxial constraints imposed by the substrate. This can be done, for example, by growing the film on a soluble substrate (e.g. NaCl [77]) or by employing a sacrificial buffer layer. A buffer layer of Cr is the most common choice at this purpose [78]. In this thesis the case of Cr under-layer grown on MgO will be described.

1.3.4 Actuation devices and energy harvesters based on NiMnGa films

In this Section, two examples relative to the realization of an actuation device and an energy harvester based on NiMnGa thin films are reported. Besides the pioneering works proposing these model systems, a lot of work is still required to enhance the efficiency and optimize the design of such technological devices.

1.3.4.1 Micro-cantilever based on NiMnGa thin film

The basic implementation of a micrometric actuator based on NiMnGa thin film was firstly proposed by Jenkins et al. [79]. In their work, the authors realised a cantilever starting from a martensitic NiMnGa thin film. In particular, they produced a free-standing cantilever with a total length of 20 μm, by means of focused ion beam (FIB) processing. A scanning electron microscopy (SEM) image of the cantilever is shown in Fig. 1.14a.

Once the cantilever was released, a field of 0.6 T was applied parallel to the long direction of the cantilever. In the atomic force microscopy image (Fig. 1.14b) taken in remnant condition after the removal of the applied magnetic field, an angle of 86.8° was observed between the 90° lamellae oriented along the two different directions (black lines in Fig. 1.14b). Afterward, a magnetic field is applied in the plane of the film but perpendicularly to the long direction of the cantilever.

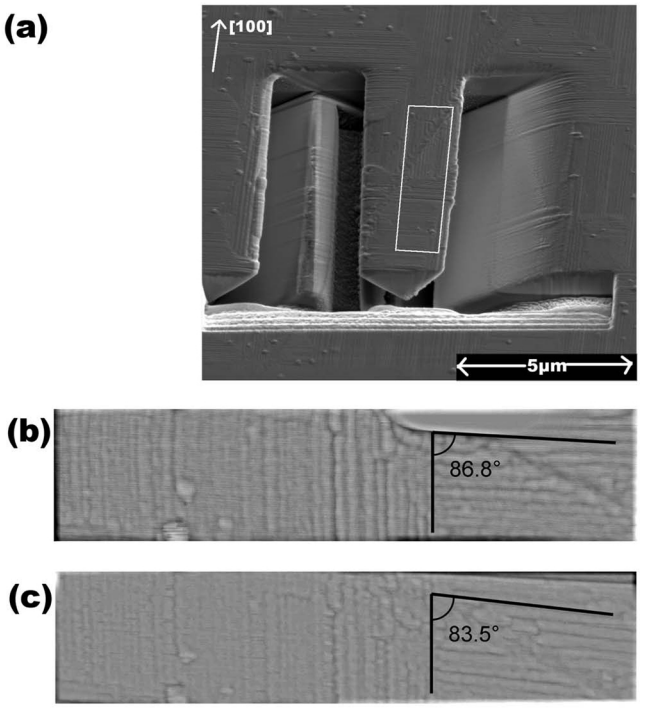

Fig. 1.14 (a) SEM image of the free-standing cantilever prepared by means of FIB. (b) AFM image (the area correspond to the white rectangle in (a)) taken in remnant condition after the application of an in-plane magnetic field (0.6 T) along the long axis of the cantilever. (c) AFM image in a remnant condition after the application of an in-plane magnetic field (0.6 T) directed perpendicular to the long axis of the cantilever. (From [79]).

In the AFM image (Fig. 1.14c) taken in a remnant condition, an angle of 83.5° was observed between the same lamellae. The authors explained this angular variation by assuming that a rearrangement occurs, due to a local reorientation of the variants close to the boundary between the plates. The observed effect was however remarkably small and the experimentally observed deformation was far away from the huge strain values expected for the twin variant reorientation typical of this kind of martensitic thin films.

Moreover, the small effect observed by the authors is irreversible thus demonstrating that a proper tailoring of the film properties and the optimization of free-standing structures preparation procedures are strongly necessary to obtain functional devices.

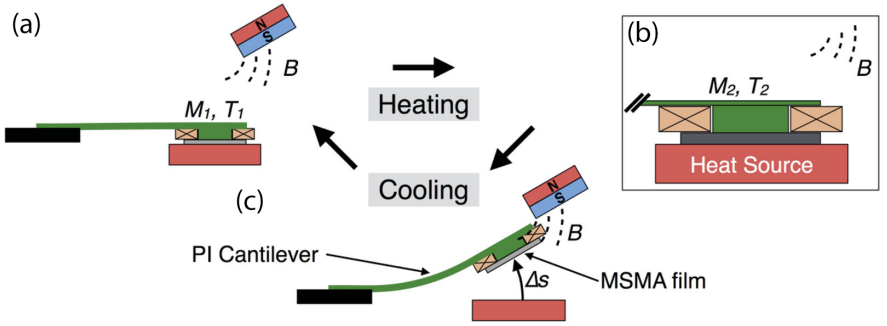

Fig. 1.15 Model for an energy harvesting system based on MSM alloy thin film. When the MSM film is contact with the heat source its temperature change from T_1 to T_2 and its magnetization from M_1 to M_2, as shown in (a) and (b). The change in the magnetization ΔM causes a magnetic attraction force towards the external permanent magnet (c) and induces a current in the pickup coils placed below the film. The MSM film is no more in contact with the heat source and is cooled below the T_M temperature: the magnetic force thus vanishes and the elastic force of the polymeric cantilever restores the initial state of the device. (From [83])

1.3.4.2 High-frequency energy harvester based on MSM thin films

The availability of miniature energy harvesters would be of great benefit to the development of novel self-sustaining integrated microsystem, where power supply or energy storage devices cannot be implemented.

Up to now, various concepts related to energy harvesting in microsystems have been developed on piezoelectric, electromagnetic induction, electrostatic and thermoelectric principles [80-82].

Regarding the aforementioned principles, unavoidable problems arise when they are applied in the miniaturization of the harvesting systems. MSM alloy are very promising thanks to the possibility to control their structure by means of different control mechanisms, which are, as already described, temperature, magnetic field and stress. Their intrinsically multifunctional properties would permit to exploit multitasking processes keeping a simple design and obtain energy harvesting devices with high cycling frequencies.

Gueltig et al. [83] have very recently proposed a model energy harvesting system based on MSM alloy thin films and have realized demonstrator devices. The model system is schematized in Fig. 1.15, in which a MSM film is at the free edge of a polymer cantilever, with a pickup coil mounted above it. A miniature

permanent magnet is placed close to the system, in order to have a field gradient at the edge of the cantilever. When the MSM film is in contact with the heat source its temperature change from T_1 to T_2 and its magnetization from M_1 to M_2: this step is represented in Fig. 1.15a and b. The change in the magnetization causes a magnetic attractive force on the cantilever edge towards the external permanent magnet (Fig. 1.15c); the magnetization change induces a current in the pickup coils placed above the film. In this last step, the MSM film is no more in contact with the heat source and is cooled below the martensitic phase transition temperature by heat conduction and convection: the magnetic force thus vanishes and the elastic force of the polymeric cantilever restores the initial state of the device.

The results obtained on the test devices prepared by the authors (here not reported) have demonstrated that the exploitation of MSM alloys as energy harvesters is possible. However, large improvements concerning the optimization of the MSM films (in order to increase ΔM for the phase transformation and reduce the thermal hysteresis of the transformation, in order to minimize the heating time), the optimization of the interface between MSM films and heat source (in order to improve the heat transfers) and the optimization of the electrical circuit are necessary.

1.4 Transmission electron microscopy

Transmission electron microscopy is a very powerful characterization tool, which permits to gain information about structure, morphology and composition of materials from atomic to micrometre scale. Differently to the case of optical microscopy, in which we use light to create a magnified image of the sample, in transmission electron microscopy the probe is an electron beam. The great advantage deriving from the employment of such kind of probing particles relies in the dual nature of the electrons, which behave as a

wave and, at the same time, as charged particles making possible the exploitation of imaging and diffraction techniques as well as, thanks to a strong interaction with the analysed sample, analytical characterizations. Moreover, the employment of charged particles, which are sensitive to magnetic fields, enables to extract information on the magnetic properties of the specimens. Remarkably, thanks to relativistic wavelengths of the electrons, which are in the picometre range at the working accelerating voltages, it is possible to realise such characterizations at a very fine scale, not reachable by other conventional techniques.

The electrons of the beam, travelling across the specimen, are subjected to scattering processes due to electrostatic interactions with the electrons and nuclei of the atoms inside the specimen. The scattering processes can be grouped in two classes, elastic and inelastic ones, depending on whether the electrons lose part of their energy or not. Another classification of the scattering processes can be outlined separating the scattering events in two groups, the coherent scattering phenomena and the incoherent ones (Fig. 1.16a). In particular, the scattering process is classified as coherent if the phase relationship with the electrons of the incident beam is preserved, while incoherent if it is lost.

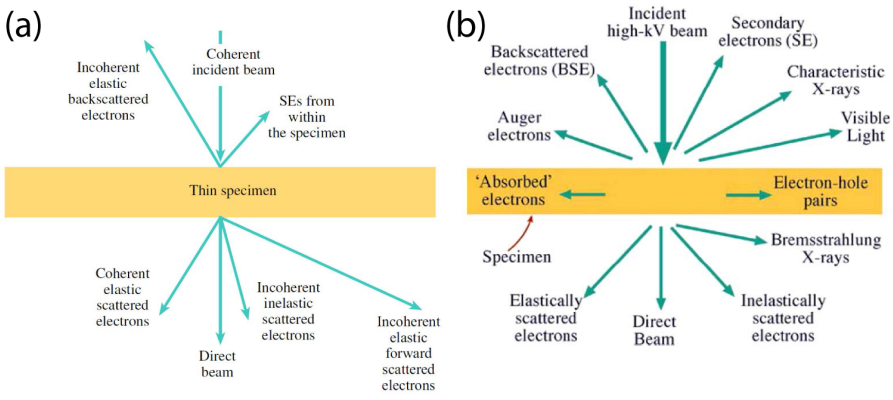

Fig. 1.16 (a) Scattering processes and (b) the secondary signals arising from the interaction between the electron beam and a thin specimen in a TEM. (From [84])

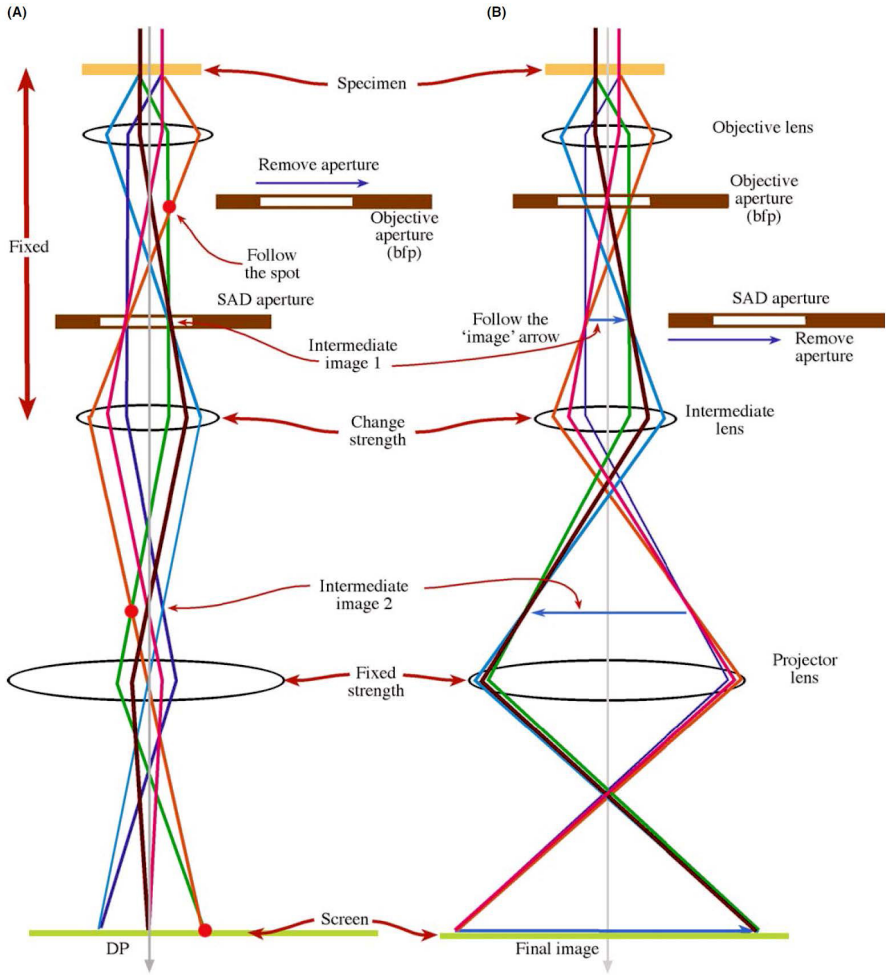

Fig. 1.17 Schematic representation of the imaging (a) and diffraction (b) working modes in a TEM. (From [84])

Depending on the scattering process, different imaging techniques can be exploited [84]. In particular the coherent elastic scattering (*Bragg scattering*) is at the base of the conventional imaging techniques and electron diffraction, while the incoherent elastic scattering (*Rutherford scattering*) is exploited for Z-contrast imaging.

In addition, thanks to the inelastic scattering processes, a wide range of secondary signals is produced as a consequence of the interaction between

the beam and the specimen, as schematized in Fig. 1.16b. In particular, characteristic X-rays and inelastically transmitted electrons are usually employed to obtain analytical information (chemical composition, coordination state, etc.), and the relative spectroscopic techniques are respectively called *energy dispersive X-Ray spectroscopy* (EDXS) and *electron energy-loss spectrometry* (EELS).

In Fig. 1.17, the two working modes of imaging (a) and diffraction (b) are schematized. In particular, if the imaging system (constituted by the lenses below the objective lens) is focused on the image plane of the objective lens an high magnification image of the sample is obtained; if the imaging system is focused on the back focal plane of the objective lens, a diffraction pattern is obtained.

In the following, the principles at the base of most common transmission electron microscopy techniques are briefly mentioned, while a more detailed discussion of the less common electron holographic techniques is presented with the aim to give to the readers the basic tools to comprehend the discussion of the experimental results reported in the next Chapters.

1.4.1 Conventional transmission electron microscopy

In conventional transmission electron microscopy, a *diffraction contrast* can be obtained by selecting only one diffracted beam with an aperture in the back focal plane of the objective lens. In this way, the contrast in the obtained image arises thanks to the local perturbations in the periodicity and orientations of atomic planes due to changes in crystalline phases, atomic ordering and defects. The image is therefore a high magnification map of the diffraction efficiency (or transmission efficiency, if the transmitted beam is selected) related to the selected diffraction spot.

An easy way to describe the image formation for this imaging technique is the "*two beams approximation*" that can be developed following the Howie-

Whelan formulation [85], not reported here. The most important aspects emerging from the formulation are that the transmitted and diffracted intensities vary periodically with the two independent variables t and s, where t is the sample thickness and s is a parameter related to the deviation from the ideal Bragg condition.

1.4.2 High-resolution transmission electron microscopy

A different imaging technique can be performed if more diffracted beams are selected and contribute to the image formation. In this case, the diffracted beams can interfere and the image is created as an interferogram. The technique is also called *phase contrast*, since the phases of the diffracted beams have a key role in the contrast formation, or, alternatively, high-resolution transmission electron microscopy (HRTEM).

A basic formulation (whose validity is restricted to the ideal case of very thin specimens) of the image contrast formation is possible by using the basic concepts of information theory [86]. In the case of very thin specimens, a detailed description can be carried out by applying the "*phase object approximation*" and assuming that the sample is a "*weak phase object*". For the detailed theoretical formulation, the reader is addressed to specific textbooks [87, 88].

It is worth to note that for real specimens, far from the ideal case of thicknesses of few atomic cells, the HRTEM images show a complex dependence from both the thickness and the defocus. The obtained interferogram contains the periodicity of the reticular potential, giving useful crystallographic information; however, to correctly describe and interpret the HRTEM images, the employment of image simulations is strictly required.

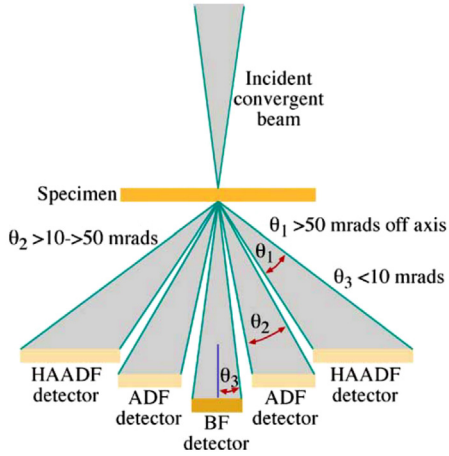

Fig. 1.18 Schematic representation of a typical configuration of detectors in STEM mode. (From [84])

1.4.3 Scanning transmission electron microscopy imaging

Differently to the techniques briefly introduced up to now, based on the parallel illumination of the entire area of the sample that is under investigation, in the scanning transmission electron microscopy (STEM) technique the beam is concentrated in a very small probe and a raster scan of the portion of interest of the sample is performed. In this working mode, the electron beam generated by the gun is focalized by the lenses of the condenser system (above the specimen plane) and an image of the electron source is created in the specimen plane. Thanks to scanning coils, the focalized electron probe is moved along the specimen and the transmitted electrons are detected below the sample. The intensity revealed by the detectors is recorded as a function of the beam position during the scan and the final image is therefore obtained.

The great advantage of this technique is that the spatial resolution achieved is strictly related to the size of the probe. The only lens involved in this techniques are the lens above the specimen, which are the only one contributing in the formation of the focalized probe. The detectors used in

STEM imaging modes are positioned below the sample, in back focal plane of the objective lens and are constituted by concentric rings. These detectors are grouped in bright field and dark field detectors, depending if they integrate or not also the transmitted beam (Fig. 1.18). Particularly interesting is the employment of a high-angle annular detector (*high-angle annular dark field*, HAADF), which permits to obtain an image by collecting the electrons that undergo to incoherent elastic scattering processes. The cross section for the scattering process of such electron, which are scattered at high-angles, is the Rutherford one and is proportional to Z^{α} ($\alpha \approx 1.7$), where Z is the atomic number. In this way, if the specimen is sufficiently thin, the contrast in the image can be directly related to the atomic number Z and for this reason the technique is commonly called *Z- contrast*.

The employment of a focalized probe permits to simultaneously acquire other signals apart from the transmitted electrons. The interactions between the beam and the specimen can generate inelastic processes in which the beam loses a part of its energy, which is transferred to the sample. The principal techniques making use of secondary signals, exploited in a TEM to achieve analytical information, are the already mentioned electron energy-loss spectrometry and energy dispersive X-ray spectroscopy.

For a detailed description of the STEM working mode the reader is addressed to the references: [89].

1.4.4 Electron Holography

The recent availability of high brightness, stable and coherent field emission guns permits to apply electron holography to a wide variety of materials, which range from the semiconductors [90, 91] to magnetic materials [92, 93]. At the same time, the great advances in the design and fabrication of advanced magnetic materials focus the attention of the scientific community on the need for characterization techniques able to investigate the magnetic properties of the materials below the micrometric scale.

Electron holography is a very powerful tool that consents to retrieve the phase shift of the electron wavefuntion, which is due to the magnetic and electric fields. From the magnetic phase shift, the flux lines of magnetic induction projected along the direction of the incident electron beam can be directly visualized at the nanometre scale, permitting the study of the domains structure and the magnetization processes in many nanostructured magnetic materials. In a similar way, if the electrostatic phase shift is taken into account, electron holography can be also successfully employed to investigate the electric potential distribution.

There are different approaches in electron holography, the most common being *off-axis holography* and *in-line electron holography*. The off-axis electron holography makes use of an electron biprism to create an interference fringes pattern. This technique can be divided in two main subgroups:

(i) *high-resolution* electron holography, in which the final aim is to improve the resolution of HRTEM images using the phase plates to correct the lens aberrations [94];

(ii) *medium-resolution* electron holography, which is a technique finalized to the characterization of magnetic and electrostatic fields with nanometre spatial resolution [95].

The in-line electron microscopy technique, commonly called Lorentz microscopy, permits to retrieve the phase of the electron wavefunction measuring only an intensity distribution along the direction parallel to the optical axis of the microscope. This technique does not require an electron biprism and it is very powerful to easily obtain qualitative information about magnetic fields over a large area of the sample [93, 96].

In the following, the basic concepts regarding medium resolution off-axis electron holography and Lorentz microscopy are introduced, focusing the attention to the most relevant aspects for the characterization of magnetic materials. These techniques have been widely employed in the characterization of the magnetic materials described in the next Chapters.

1.4.4.1 Off-axis electron holography

Basic concepts

The main requirements to perform off-axis electron holography are a transmission electron microscope equipped with an electron biprism and a highly coherent field emission gun. In a conventional transmission electron microscope, the specimen is inserted in the gap among the pole pieces of the objective lens. When the lens is excited, the specimen is therefore subjected to a strong magnetic field of approximately 2T. In such a high field, most of the magnetic specimens are immediately magnetized upon being inserted into the electron microscope column, thus compromising the investigation of the original magnetic domains structure of the sample. To perform electron holography, instead, a proper hardware configuration that permits to perform the experiment without applying any magnetic field on the specimen is necessary [98]. In the modern instruments this is achieved by employing a Lorentz lens, which is a non-immersion lens whose pole pieces are below the specimen position in the TEM column (Fig. 1.19a).

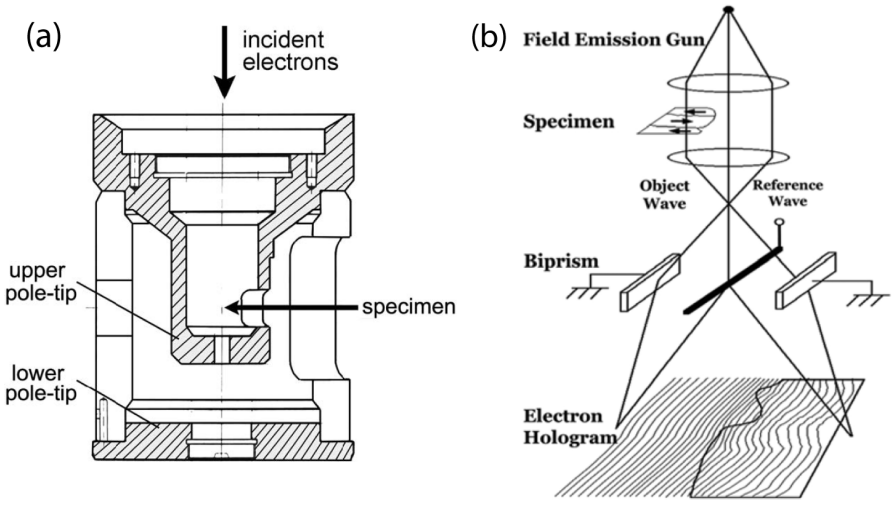

Fig. 1.19 (a) Schematic diagram (cross-section) of a Lorentz lens. (b) Scheme of the experimental setup for electron holography. (From [97, 98])

The typical electron-optical configuration for an electron holography experiment is schematized in Fig. 1.19b. The region of interest of the sample is positioned in a way so that it covers approximately half of the field of view. The electron biprism, which is a thin conducting wire placed close to the first image plane, is excited with a small positive voltage in order to promote the overlap of the reference electron wave, that has travelled in the vacuum, with the electron wave that has passed through the specimen. Increasing the voltage applied to the biprism, the width of the overlap region increases making possible the observation of larger portion of the specimen but putting strong constraints on the spatial coherence of the source necessary to maintain a sufficient contrast in the interference fringes.

In coherent image formation, the electron wavefunction in the image plane can be written in the form:

$$\psi_i(\bar{r}) = A_i(\bar{r})\exp\left[i\phi_i(\bar{r})\right] \tag{1.13}$$

where $\bar{r}$ is a two-dimensional vector in the plane of the sample, being the thickness of the specimen negligible compared to its lateral extension, A and ϕ are the wavefunction amplitude and phase, respectively. In conventional imaging techniques, we record a spatial distribution of wavefunction intensity given by:

$$I(\bar{r}) = \left|A_i(\bar{r})\right|^2 \tag{1.14}$$

which is only related to the amplitude of the wavefunction and all the information concerning the phase is lost. On contrary, in the intensity distribution related to an off-axis electron hologram an additional term due to the tilted plane reference wave must be added to the wavefunction of the perturbed wave, thus obtaining [98]:

$$I_{holo}(\bar{r}) = \left|\psi_i(\bar{r}) + \exp\left(2\pi i\bar{q}_c\cdot\bar{r}\right)\right|^2 \tag{1.15}$$

where the tilt of the reference wave is given by the two dimensional reciprocal space vector $\bar{q} = \bar{q}_c$.

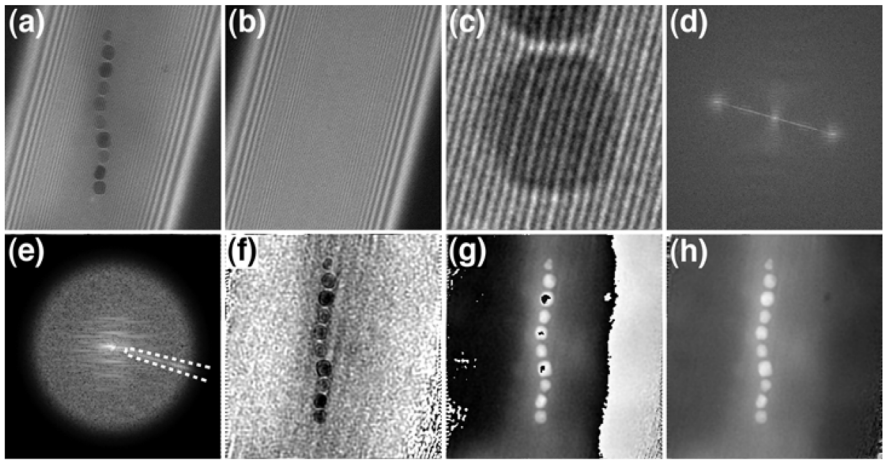

Fig. 1.20 Sequence of steps performed to extract amplitude and phase from an electron hologram. (a) Experimental hologram of a chain of magnetite crystals. Fresnel fringes due to diffraction effects at the edge of the biprism are visible at both the sides. The field of view of the image is 725 nm. (b) Reference hologram acquired in the vacuum, immediately after acquiring the hologram on the specimen. (c) Magnified region of the specimen hologram. (d) FFT of the electron hologram shown in (a), containing the centerband, two sidebands and the diagonal streak resulting from the Fresnel fringes. (e) One of the two sidebands is extracted from the FFT applying a circular mask with smoothed edges; also the streak due to Fresnel fringes (marked by dashed lines) can be masked. The selected sideband is centred and an IFFT is performed to obtain a complex image, whose amplitude and phase are represented in (f) and (g), respectively. Finally phase-unwrapping algorithms are used to remove the 2π-discontinuities from the phase (g) to obtain the final unwrapped phase (h). (From [99])

By combining this expression with Eq. 1.13, the hologram intensity can be rewritten in the form:

$$I_{holo}(\overline{r}) = 1 + A_i^2(\overline{r}) + 2A_i(\overline{r})\cos\left[2\pi i\overline{q}_c \cdot \overline{r} + \phi(\overline{r})\right] \qquad (1.16)$$

in which three different contributions can be identified: the reference image intensity, the specimen image intensity and a set of cosinusoidal fringes whose local phase shift and amplitudes are related to the phase and amplitude of the electron wavefunction in the image plane (Eq. 1.13). In Fig. 1.20a an experimental electron hologram of a sample of magnetic nanoparticles is shown [99]. A reference hologram (Fig. 1.20b) in the vacuum is taken immediately after taking the hologram of the specimen for a reason that will be explicated later. In Fig. 1.20c, a magnified region of the hologram shown in

Fig. 1.20a is reported: as can be seen, local changes in the position of fringes are observed in proximity of the particles.

By performing the Fourier transform of the hologram, we obtain [99]:

$$\begin{aligned} FFT\left[I_{holo}(\overline{r})\right] &= \delta(\overline{q}) + FT\left[A_i^2(\overline{r})\right] + \\ &+ \delta(\overline{q}+\overline{q}_c) \otimes FT\left[A_i(\overline{r})\exp\left[i\phi_i(\overline{r})\right]\right] + \\ &+ \delta(\overline{q}-\overline{q}_c) \otimes FT\left[A_i(\overline{r})\exp\left[-i\phi_i(\overline{r})\right]\right] \end{aligned} \quad (1.17)$$

The Eq. 1.17 contains a peak at the origin of the reciprocal space corresponding to the Fourier transform of the reference image ("*centerband*"), a second peak centred at the origin corresponding to the Fourier Transform of the conventional bright field TEM image and two "*sidebands*". The two sidebands are constituted by a peak centred at $\overline{q} = -\overline{q}_c$, corresponding to the Fourier transform of the image wavefunction, and a peak centred at $\overline{q} = \overline{q}_c$, corresponding to the complex conjugate of the image wavefunction. These two terms are the last ones in Eq. 1.17 and they contain the information about both amplitude and phase of the electron wavefuction.

The Fourier transform of the hologram shown in Fig. 1.20a is reported in Fig. 1.20d. The centerband and the two sidebands are recognizable. The diagonal streak is caused by the Fresnel fringes due to diffraction effects at the edges of the biprism.

In order to recover the complex electron wavefunction, one of the two sidebands is selected and a circular mask with smoothed edges is applied to reduce its intensity radially to zero, as shown in Fig. 1.20e. Also the streak due to Fresnel fringes can be masked. The selected sideband is finally shifted to the centre of the image and then an inverse Fourier transform is performed. The complex image obtained is given by the expression [98]:

$$FT^{-1}\left\{\delta(\overline{q}) \otimes FT\left[A_i(\overline{r})\exp\left[i\phi_i(\overline{r})\right]\right]\right\} = A_i(\overline{r})\exp\left[i\phi_i(\overline{r})\right] \quad (1.18)$$

The amplitude and phase of the complex image wavefunction are finally calculated using the expressions:

$$A = \sqrt{\mathrm{Re}^2(\psi) + \mathrm{Im}^2(\psi)} \qquad \phi = \tan^{-1}\frac{\mathrm{Im}(\psi)}{\mathrm{Re}(\psi)} \tag{1.19}$$

where *Re(ψ)* and *Im(ψ)* are the real and imaginary parts respectively of the complex wavefunction. The amplitude and phase extracted from the hologram in Fig. 1.20a are shown in Fig. 1.20f and 1.20g, respectively. The resulting amplitude image is similar to an energy-filtered bright-field TEM image, since the contribution of inelastic scattering to the holographic interference fringe formation is negligible [99]. The phase image contains discontinuities in position where the phase shift exceeds the 2π amounts. The phase image can be unwrapped to remove the discontinuities by using "unwrapping" algorithms (Fig. 1.20h).

The phase information is stored in the local lateral displacements of holographic interference fringes. Small inhomogeneities of the thickness and the charge of the biprism wire, lens distortions, as well as charging effect at apertures, can introduce artefacts into the reconstructed wavefunction and, hence, into the extracted phase [99]. In order to take into account these effects and correct the artefacts in the phase, a reference hologram (Fig. 1.20b) is usually obtained from the vacuum by removing the specimen from the field of view without changing the electron-optical setting of the microscope. The correction of said undesired effects is hence possible by subtracting the phase image obtained from the vacuum wavefunction from the phase image obtained from the specimen wavefunction and the distortion-free phase of the image wavefunction is therefore extracted.

Electrostatic and magnetic contributions to the phase shift

The phase shift obtained by electron holography is sensitive to both the electrostatic potential and the magnetic vector potential of the specimen. If we assume that the specimen is thin and weakly diffracting, dynamical diffraction can be neglected and the phase shift of the electron wavefunction can be expressed by the *Aharonov-Bohm phase shift* [100]:

$$\begin{aligned}\phi(x,y) &= \phi_e(x,y)+\phi_m(x,y) = \\ &= \sigma\int_{-\infty}^{+\infty}V(x,y,z)\,dz - \frac{e}{\hbar}\int_{-\infty}^{+\infty}A_z(x,y,z)dz\end{aligned} \tag{1.20}$$

where V is the electrostatic potential, A_z is the component of the magnetic vector potential parallel to the electron beam propagation direction and σ is the interaction constant given by:

$$\sigma = \frac{2\pi}{\lambda}\ \frac{E+E_0}{E(E+2E_0)} \tag{1.21}$$

and depends on the acceleration voltage of the microscope $U = E/e$. In the above reported expressions, e and $\hbar$ are the charge of the electron and reduced Plank constant, respectively. In Eq. 1.21, λ is the relativistic electron wavelength and E_0 is the rest mass of the electron.

When no charge distributions or applied electric fields are present within or around the specimen, the electrostatic contribution to the phase shift originates from the *mean inner potential* (MIP) V_0 of the material coupled with the thickness variations of the specimen, not negligible at the sample edges. In this case the *electrostatic phase shift* is given by:

$$\phi_e(x,y)=\sigma V_0\, t(x,y) \tag{1.22}$$

where $t(x,y)$ is the specimen thickness. If the specimen has a uniform composition, then the electrostatic contribution to the phase shift is proportional to the local specimen thickness.

The magnetic contribution to the phase shift (*magnetic phase shift*) contains information about the magnetic flux. The difference between the magnetic phase shift calculated at two arbitrary positions with coordinates (x_1, y_1) and (x_2, y_2) in a phase image is given by:

$$\begin{aligned}\Delta\phi_m &= \phi_m(x_1,y_1)-\phi_m(x_2,y_2) = \\ &= -\frac{e}{\hbar}\int_{-\infty}^{+\infty}A_z(x_1,y_1,z)\,dz + \frac{e}{\hbar}\int_{-\infty}^{+\infty}A_z(x_2,y_2,z)\,dz\end{aligned} \tag{1.23}$$

that can be expressed by the loop integral:

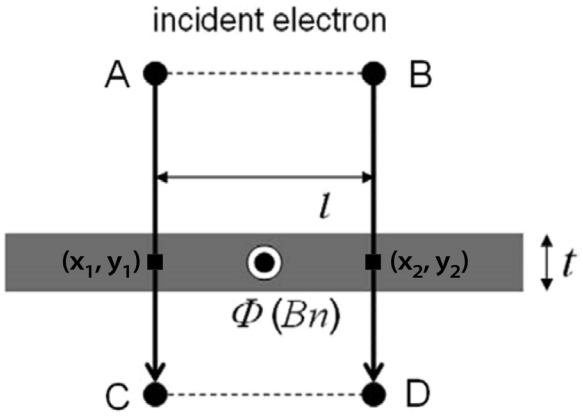

Fig. 1.21 Scheme of a thin magnetic specimen with constant thickness t. Φ is the magnetic flux through the plane ABCD, assuming that A, C and B, D are respectively on the perpendiculars to the sample in (x_1,y_1) and (x_2,y_2) at an infinite distance from the specimen. (From [98])

$$\Delta\phi_m = -\frac{e}{\hbar}\oint A \bullet dl \tag{1.24}$$

on a rectangular loop formed by two parallel electron trajectories at the points (x_1, y_1) and (x_2, y_2) and by the closure segments perpendicular to the electron trajectories taken at an infinite distance. A scheme of the described loop is given in Fig. 1.21.

Thanks to the Stockes's theorem, the quantity $\Delta\phi_m$ can be related to the flux of magnetic induction concatenated the area *S* delimited by the rectangular loop:

$$\Delta\phi_m = \frac{\pi}{\phi_0}\Phi_S \tag{1.25}$$

where $\phi_0 = h/2e$ is a flux quantum. The phase difference $\Delta\phi_m$ between any two points in a phase image is therefore a measure of the magnetic flux concatenated to the region of the space bounded by the two electron trajectories crossing the sample in the two points.

The relationship between the magnetic phase shift and the components of the magnetic induction in the plane of the film can be established by calculating the gradient of ϕ_m, which is given by [99]:

$$\nabla\phi_m = \frac{e}{\hbar}\left[B_y^p(x,y),\ -B_x^p(x,y)\right] \tag{1.26}$$

where:

$$B_i^p(x,y) = \int_{-\infty}^{+\infty} B_i(x,y,z)dz \tag{1.27}$$

represents the component of the magnetic induction perpendicular to the direction of the incident electron beam projected along the beam direction.

If the sample has constant thickness and the magnetic induction does not vary significantly with z within the specimen, Eq 1.26 can be used to quantify the magnetic field strength and its direction at a local scale. If the thickness is not constant, it is necessary to separate the magnetic and electrostatic contributions to obtain correct information on the magnetic properties of the material.

Separation of magnetic phase shift and mean inner potential

As pointed out in the previous description, the total phase shift of the electron wavefunction contains two terms, due to the electrostatic and magnetic contributions respectively. The mean inner potential contribution is negligible when the specimen thickness is uniform or when the thickness changes very gradually in the investigated portion of the sample.

Actually, although measurements of the local values of the mean inner potential can be useful to study the morphology or the chemical composition of the specimen, its contribution to the phase shift is detrimental for the investigation of magnetic materials by electron holography.

In particular, for small magnetic entities (in the range of few to tens nanometres) the mean inner potential contribution can be larger than the magnetic contribution, thus completely compromising the study of the magnetic properties of the materials [101].

Several methods have been proposed in order to separate the magnetic from the electrostatic contribution, in order to isolate the magnetic information.

Tonomura et al. [102] proposed a method that utilizes the "*time-reversal operation of an electron beam*". This method permits to achieve the separation by acquiring a second hologram in the same area of the sample, after turning upside-down the specimen with respect to the first acquired hologram. The sign (positive or negative) of the magnetic phase shift depends on the direction of the incident electron beam, while the sign of the electrostatic contribution does not change. Calculating the sum or difference of the phases extracted by the two holograms it is therefore possible to obtain twice the mean inner potential and twice the magnetic phase shift, respectively. Once the mean inner potential contribution has been isolated, it can be subtracted from all the subsequent phase images of the same portion of the sample to isolate the magnetic phase shift. A smoothing of the final phase image is often used to remove statistical noise and artefacts deriving from small residual misalignment of the two phase images [99].

Dunin-Borkowski et al. [103] proposed an alternative and more practical method consisting in performing an in-situ magnetization reversal inside the microscope column: applying a sufficiently large magnetic fields, the magnetization of the sample can be saturated in two opposite directions and two holograms that differ only in the sample magnetization direction can be acquired. The sum of the two phase images, in which the sample magnetization is along opposite directions, directly gives twice the mean inner potential contribution. This type of magnetization reversal process can be performed by using either a magnetizing TEM specimen holder or by tilting the sample and using the vertical magnetic field of the TEM objective lens. In the latter case, the objective lens can be turned off and the specimen brought back to the zero tilt condition before acquiring each hologram.

It is worth noting that this second approach is only applicable if the magnetization in the specimen can be perfectly reversed.

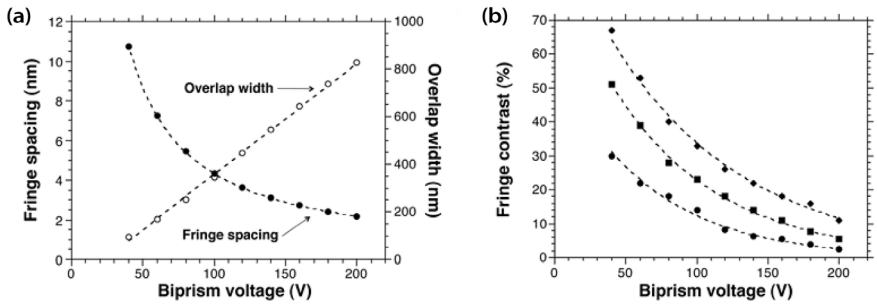

Fig. 1.22 a) Dependence of interference fringes spacing and overlap width (in nm) on biprism voltage. (b) Dependence of interference fringes visibility on the biprism voltage, at different magnifications (circles: 1450x, squares: 2250x, diamonds: 3700x). All the datas refers to a FEI Titan 800-300 TEM operated at 300kV [105, 106].

Practical aspects

As already said, a field emission gun is essential to achieve a highly coherent electron beam. In the reality, a perfectly spatially and temporally coherent electron source does not exist.

In an electron holography experiment the coherence degree has to be high enough to permit the acquisition of an interference fringes pattern with a sufficient contrast in a sufficiently low acquisition time. Typical acquisition times range from 5 to 20 seconds, but longer exposures can be performed providing that high stabilities of the holder and the microscope column prevent specimen and beams drifts to occur.

In order to characterize the magnetic structure of the materials, the microscope objective lens is usually turned off since it creates a high field (about 2T) in the region in which the specimen is inserted. As previously described, to overcome this problem a non-immersion Lorentz lens is used as the main imaging lens: this lens permits to create an image at a relatively high magnification (up to 70k for a FEI Titan 80-300 microscope), leaving the sample in a field-free environment. The C_s aberration for the Lorentz lens (for a FEI Titan microscope, C_s = 8400 mm [104]) is significantly high if compared with typical values of common objective lens and a spatial resolution of about 2 nm is achieved. It must be noted, however, that the spatial resolution for

magnetic characterization is primarily limited by the interference fringes spacing and by the signal to noise ratio.

In electron holography, a small portion of the sample can be analysed. By changing the voltage of the biprism, it is possible to increase the overlap width (Fig. 1.22a). However, an increase of the biprism voltage produces at the same time a reduction in the fringe spacing and in the fringes contrast (Fig. 1.22a and b). The proper voltage has therefore to be chosen carefully in order to have a sufficient overlap width without sacrificing fringe contrast and spacing, which finally affect the phase and spatial resolution respectively.

1.4.4.2 Lorentz microscopy

Basic concepts

Electrons are charged particles and when they travel through a region in which a magnetic induction B is present, they experiment a force. Provided that no electric field is present, this force is the classical Lorentz force:

$$\overline{F} = -\left|e\right| \overline{v} \times \overline{B} \tag{1.28}$$

where v is the velocity of the electrons. If an electron travels for a distance t through a region in which a magnetic induction B perpendicular to v is present, it will be deflected by an angle θ_L given by [107]:

$$\theta_L = \frac{eBt}{mv} \tag{1.29}$$

where m is the mass of the electron, and B and v are equal to $|\boldsymbol{B}|$ and $|\boldsymbol{v}|$, respectively. The Eq. 1.29 can be alternatively expressed as:

$$\theta_L = \frac{eB\lambda t}{\hbar} \tag{1.30}$$

where λ is the electron wavelength and $\hbar$ the Plank constant. This form is convenient since relativistic effect can be easily taken into account by using the proper value for λ. Typical values of the Lorentz angle are very small, $\theta_L \approx 10^{-5}$ rad, that is about 100 times less than typical Bragg diffraction angles in TEM ($\theta_B \approx 10^{-3}$ rad).

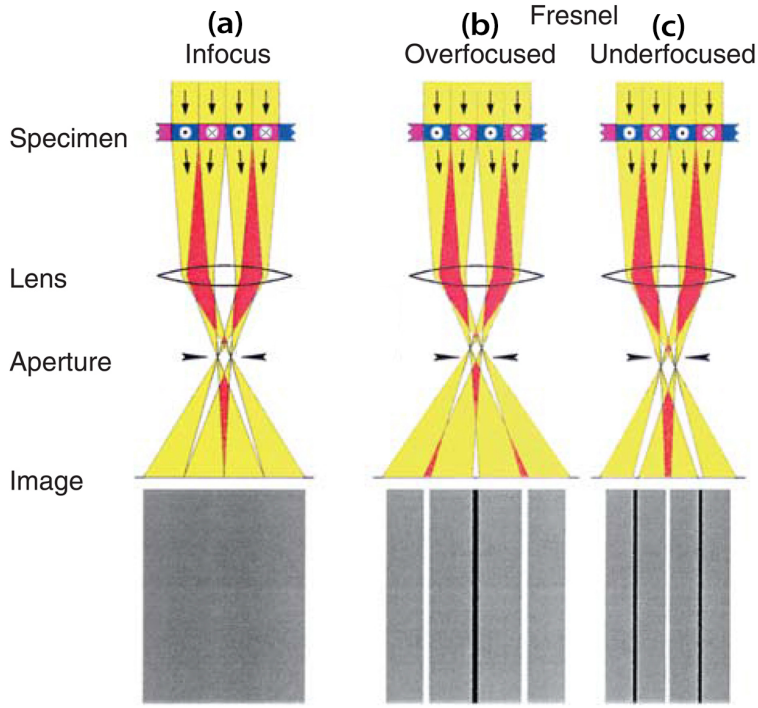

Fig. 1.23 A schematic diagram of the Fresnel mode for Lorentz microscopy. In top part, the electro-optical system is schematized (in a real microscope, two or more additional lenses are present below the objective lens). In the bottom part, the resulting images are given: (a) in-focus, (b) over-focused and (c) under-focused images. (From [107]).

Since the effect of magnetic induction is to deflect the electrons, the intensity of an electron beam travelling across a magnetic specimen is not affected by magnetic domains in the material: the effect of the magnetic induction, as described, is to solely change the direction in which electrons emerge from the specimen but not the number of electrons or their speed. An in focus image of the specimen, therefore, does not contain any information about the magnetic domain structure [107].

The basic principles regarding the magnetic contrast formation in Lorentz imaging are schematized in Fig. 1.23. The top part of the figure shows the electron rays diagram, the cross-sectional view of the specimen, the objective lens and the objective aperture. The schematized specimen has magnetic

domain with their magnetization directions perpendicular to the beam propagation direction and pointing alternatively in and out of the plane of the paper (as schematized by the arrows heads and tails). In the bottom part, the contrast obtained in the corresponding images is shown.

The parallel incident beam illuminates uniformly the specimen but, after propagating through the sample, the electron rays are deflected either to the right or to the left depending on the domain magnetization direction. The deflected rays travel through the electro-optical system and then form an image into the screen. Although no magnetic contrast is detectable in the in-focus image (Fig. 1.23a), a magnetic contrast appears if out-of-focus images are acquired. In particular, in the over-focus and under-focus images a contrast is visible at the magnetic domain walls (Fig. 1.23b and c respectively). The ray diagram shows that the bright and dark lines are generated, respectively, by an increase or a decrease of the number of incident electrons detected in the image, due to the defocusing.

The local redistribution in the observed intensity, due to the local deflection of electron rays by magnetic domains, is also called "*magnetic refraction*". This method of displaying the domain structure is called *Fresnel method* (for the analogies to the optical case of the interference produced by the Fresnel biprism). The contrast appearing in the over-focused image is reversed when the objective lens is under-focused.

Moreover, the defocusing the objective lens alters the magnification of the image because of the change in the lens current; these changes in magnification are shown exaggerated in Fig. 1.23b and c.

Transport of Intensity Equation

Some decades ago, Teague [108] derived an equation for the wave propagation in terms of a phase and intensity distribution under the small angle approximation (*paraxial approximation*), the so-called *Transport of Intensity Equation* (TIE). The remarkable aspect in the Teague work is that it

highlights the possibility to determine the phase distribution by only measuring the intensity distribution.

In particular, starting from the time-independent Schrödinger equation:

$$\left[-\frac{\hbar^2}{2m}\nabla^2 - V\left(\bar{r}\right)\right]\psi\left(\bar{r}\right) = E\,\psi\left(\bar{r}\right) \tag{1.31}$$

if we assume that the electron travels in vacuum $V(\bar{r})$ and the electron wavefunction is a perturbed plain wave travelling along the beam propagation direction (z), written in the form:

$$\psi\left(\bar{r}\right) = \exp\left(ik_z z\right) f\left(\bar{r}\right) \tag{1.32}$$

under the paraxial approximation (that can also be expressed by $k_x, k_y \ll k_z$, where k_x, k_y and k_z are the components of the wave vector for the electrons), the Schrödinger equation becomes:

$$\left(i2k\frac{\partial}{\partial z} + \nabla_{xy}^2\right)\psi\left(\bar{r}\right) = 0 \tag{1.33}$$

where $k = 2\pi/\lambda$ is the wave vector, λ is the electron wavelength and ∇_{xy}^2 is a 2D Laplacian operator.

If we now express the complex electron wavefunction by using the real functions, I and ϕ, which represent the intensity and phase distribution respectively, in this form:

$$\psi(\bar{r}) = \sqrt{I(\bar{r})}\exp\left[i\phi(\bar{r})\right] \tag{1.34}$$

then also the Schrödinger equation can be split in two equations, one for the real and one for the imaginary part. The imaginary part gives the TIE equation:

$$\frac{2\pi}{\lambda}\frac{\partial}{\partial z}I(\bar{r}) = -\nabla_{xy}\bullet\left[I(\bar{r})\ \nabla_{xy}\phi(\bar{r})\right] \tag{1.35}$$

The TIE equation is a partial differential equation that correlates the intensity and phase distributions in a quite complicated way, since the intensity distribution derivative along the beam propagation direction is connected to the phase by a non-trivial differential relationship.

Following the method proposed by Paganin and Nugent [109], we can introduce an intermediate function Φ, whose gradient corresponds to the product of the wavefunction intensity and its phase gradient (see the term inside the square bracket in the left side of Eq. 1.35), so defined:

$$\nabla_{xy}\Phi(\bar{r}) \equiv I(\bar{r})\,\nabla_{xy}\phi(\bar{r}) \tag{1.36}$$

which, if inserted in the TIE equation (Eq. 1.35), gives:

$$\nabla^2_{xy}\Phi(\bar{r}) = -\frac{2\pi}{\lambda}\frac{\partial}{\partial z}I(\bar{r}) \tag{1.37}$$

In this way, the TIE equation turns to a standard inhomogeneous Poisson equation. In the first step, the Poisson equation is solved to obtain the auxiliary function Φ. Then, dividing the gradient of Φ by the intensity I and taking the 2D divergence, a second Poisson equation for the phase shift can be written:

$$\nabla^2_{xy}\phi(\bar{r}) = \nabla_{xy}\bullet\left(\frac{1}{I(\bar{r})}\nabla_{xy}\Phi(\bar{r})\right) \tag{1.38}$$

the solution is the phase function, given by:

$$\phi(\bar{r}) = -\frac{2\pi}{\lambda}\nabla^{-2}_{xy}\nabla_{xy}\bullet\left[\frac{1}{I(\bar{r})}\nabla_{xy}\nabla^{-2}_{xy}\frac{\partial}{\partial z}I(\bar{r})\right] \tag{1.39}$$

where ∇^{-2}_{xy} is a formal expression indicating the inverse Laplacian operator.

The two Poisson's problems can be solved by using Fourier transforms. However, in order to numerically solve the partial differential equation it is unavoidable to face tedious problems related to the boundary conditions. A lot of different methods have been proposed in the last years to reduce the artefacts due to boundary effects (e.g. [110, 111]), but an artefact-free algorithm to retrieve the phase by TIE equation is still lacking.

To experimentally evaluate the intensity derivative with respect to z, three images are usually acquired: beside the in-focus image, two defocused images are acquired at the defoci values $\pm\varepsilon$. This image series is usually called *Fresnel series*. The intensity derivative is then calculated by the central difference method:

$$\frac{I(z+\varepsilon)-I(z-\varepsilon)}{2\varepsilon} = \frac{\partial I}{\partial z}+O(\varepsilon^2) \quad (1.40)$$

In principle, in order to achieve an accurate estimation of the intensity derivative the two defocused images should be acquired at very small values of defocus; however, it is always preferable to acquire the images at a large defocus step in order to increase the signal to noise ratio in the intensity difference. At large defoci values commonly chosen to take the images, a strong effect related to the variation in the lens current has to be taken into account. In particular, the images must be properly aligned and the changes in magnification need to be carefully corrected in order to avoid artefacts in the reconstruction of the phase image.

1.4.4.3 Phase contours and magnetization maps

A very common way to visualize the reconstructed magnetic phase shifts (as obtain by both electron holography and Lorentz microscopy) is the plotting of the cosine of the phase:

$$I_{ph}(\vec{r}) = \cos\phi(\vec{r}) \quad (1.41)$$

eventually after an amplification of the phase obtained by multiplying the phase image by an integer n. The cosine map offers the great advantage of giving a direct visualization of the in-plan projected flux of magnetic induction, since the lines visualized in the map represent the lines of equal phase shift. The direction of the lines and their spacing give a direct visualization of the direction and intensity of the planar component of the magnetic induction in a map at nanometre resolution.

Another common way of visualizing the features contained in the reconstructed magnetic phase shift is by calculating the B_x and B_y planar components of the magnetic induction (as defined by Eq. 1.26) and generate a 2D colour-map in which the colour gives the direction of the magnetization while the saturation is related to the vector modulus.

The two maps can be plotted superimposed thus enabling a direct visualization of the magnetic properties of the specimen. In Fig. 1.24, reported from [112], the magnetic phase contours amplified 128x for two cobalt nanoparticles rings are shown. The magnetic colour map is superimposed to the contour plot. The arrows, in agreement with the colour wheel shown, indicate the direction of the measured magnetic induction.

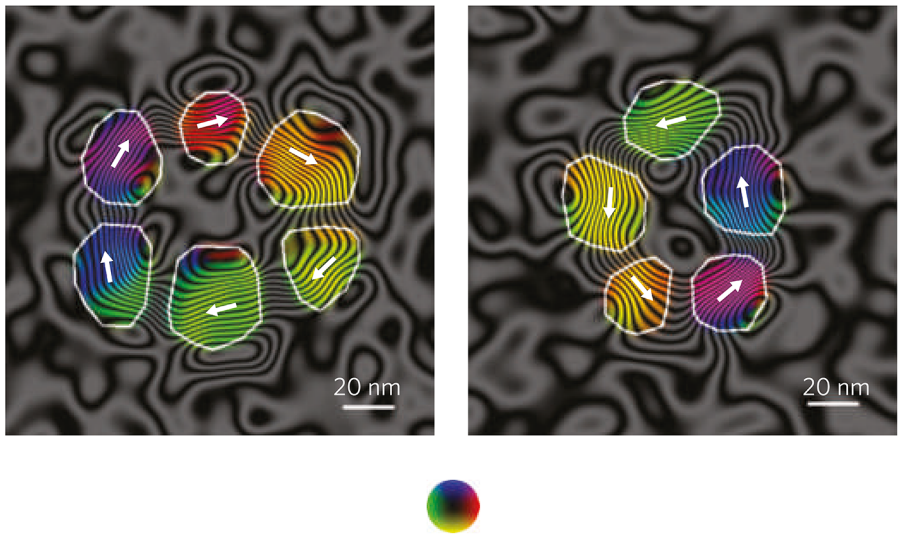

Fig. 1.24 Magnetic phase contour (x128 amplification) obtained from the magnetic contribution to the phase shift for two cobalt nanoparticles rings. The magnetic colour map is superimposed to the image; the arrows indicate the direction of the measured magnetic induction. (From [112]).

1.5 Other characterization techniques

In this Section, the other characterization techniques employed to investigate the morphology and the magnetic properties of the samples are described.

1.5.1 Scanning Probe Microscopies

The scanning probe microscopies are investigation techniques based on the scanning of the surface of the specimen by a fine tip. Depending on the interactions between the tip and the surface, maps of surface morphology, electric, magnetic or chemical properties can be obtained. In this doctoral work, the scanning probe microscopy was used in atomic force microscopy (AFM) and magnetic force microscopy (MFM) modes. The AFM exploits the Van der Waals forces to detect morphological contrast with a resolution down to few atomic layers. The MFM exploits the magnetic forces arising between the tip coated with a magnetic material and the sample, to detect the out-of-plane signal generated by the magnetic specimens. MFM technique was used to map the configuration of the out-of plane magnetic domains of the specimens, with a lateral resolution of tens of nm. For a detailed description of the techniques, the interested reader is addressed to the following reference: [113].

1.5.2 Magnetic measurements

The characterization of the superparamagnetic state of a colloidal suspension of nanoparticles can be carried out in different ways. One of the most common methods consists in performing both *zero field cooling* (ZFC) and *field cooling* (FC) measurements. In the following a brief description of the ZFC and FC is given.

1.5.2.1 Zero field cooling

In the ZFC measurement, the sample is firstly cooled at the minimum reachable temperature without any applied magnetic field and then it is heated up under a small external field.

In this way, the initial state with no net magnetization (in the superparamagnetic state moments are randomly oriented) is “frozen” when the sample is cooled down.

When an external magnetic field is applied at low temperature, the moments have not enough energy to rotate along the field direction. When the sample is heated, however, the thermal energy of the system increases and the moments start rotating. The moments can therefore align to the applied filed and an increase in the net magnetization along the direction of the applied field is thus observed. The magnetization increases up to a maximum value that is reached in correspondence of the average blocking temperature of the system. Above the blocking temperature, the kinetic energy becomes higher than the magnetic energy and the moments are misaligned, with a global lowering of the magnetization.

1.5.2.2 Field cooling

In the FC measurement, on the contrary, the nanoparticles moments are aligned along a common direction at the beginning of the experiment, by the application of an external magnetic field. Cooling down the sample under the applied field this configuration is "frozen".

During the subsequent heating of the sample, also under the applied magnetic field, the net magnetization decreases since for a growing number of nanoparticles the superparamagnetic state will establish.

Observing the trends of the ZFC and FC curves, two characteristic temperatures can be further defined. In particular, the irreversibility temperature (T_I) is defined as the temperature at which the ZFC-FC curves start to be separated and the saturation temperature (T_S) is defined as the temperature at which the FC stops to be constant. For a system of polydispersed NPs, T_B obtained as the maximum of ZFC can be considered as the average blocking temperature for the nanoparticles ensemble: under T_B nanoparticles are blocked while, over T_B they are in the superparamagnetic state. The T_I, instead, can be considered as the maximum blocking temperature corresponding to the blocking temperature of the biggest magnetic NPs. The T_S, on the contrary, is the minimum blocking temperature corresponding to the blocking temperature of the smallest nanoparticles.

1.6 Instrumental equipments

In this Section the instruments used to conduct the experiments reported in the next Chapters are briefly presented.

1.6.1 Transmission electron microscopes

The transmission electron microscopy characterizations were performed using three different instruments installed in different institutes. The instruments are here listed.

1. **JEOL JEM-2200FS** – Istituto dei Materiali per l'Elettronica ed il Magnetismo (IMEM-CNR), Parma, Italy
   Analytical transmission electron microscope (Fig. 1.25, top) working at 200 kV, equipped with Schottky FEG. The maximum achievable point-to-point resolution is 0.19 nm. The microscope is equipped with EDXS detector and an in-column omega filter.

2. **JEOL JEM-2200FS U-HRTEM** – Istituto Italiano di tecnologia (IIT), Genova, Italy
   Analytical transmission electron microscope like the JEM-2200FS described above, equipped with the C_s–objective aberration corrector (from CEOS Company). The maximum achievable resolution is 0.1 nm. The microscope is also equipped with the heating holder in order to perform temperature dependent measurements.

3. **FEI TITAN^3 80-300 U-HRTEM** – Laboratorio de Microscopias Avanzadas (LMA), Instituto de Nanociencia de Aragón (INA), Zaragoza, Spain
   This microscope (Fig. 1.25, bottom) is dedicated to ultra-high resolution TEM imaging. The microscope works at 80-300 kV acceleration voltages and is equipped with a SuperTwin objective lens

and a CETCOR C_s-objective aberration corrector from CEOS Company, allowing a point-to-point resolution of 0.08 nm. Moreover, this aberration-corrected microscope is equipped with a Lorentz lens and an electron biprism permitting to perform Lorentz microscopy and medium resolution electron holography experiments.

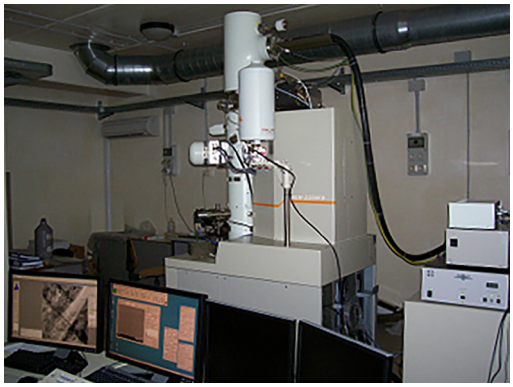

JEOL JEM-2200FS
installed at IMEM-CNR, Parma
Italy

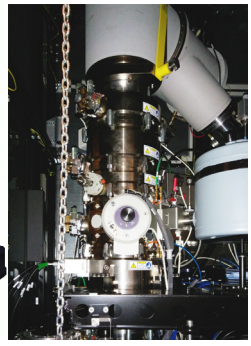

FEI TITAN^3 80-300
installed at LMA, Zaragoza
Spain

Fig. 1.25 Employed TEM microscopes, installed at IMEM-CNR (top) and LMA-INA (bottom), respectively.

1.6.2 Scanning probe microscope

The surface morphology and the out-of-plane magnetic domains were investigated by means of AFM and MFM measurement. The experiments were carried out using a Dimension 3100 equipped with Nanoscope IVa Controller (Veeco Instruments), installed at the IMEM-CNR Institute in Parma (Italy) (Fig. 1.26). High-resolution height profiles were obtained in tapping mode, while the magnetic measurements were performed in tapping mode with a double-pass technique.

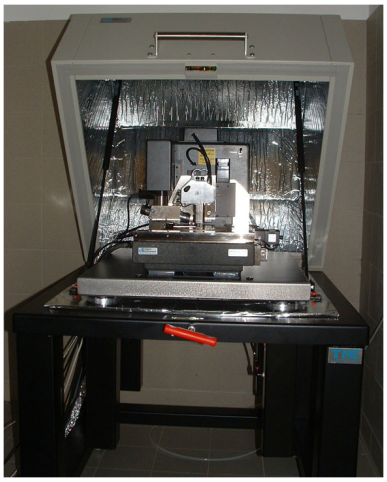

Dimension 3100 equipped with Nanoscope IVa, installed at the IMEM-CNR, Parma Italy

Fig. 1.26 Scanning probe microscope installed at IMEM-CNR.

1.6.3 Magnetometers

Magnetic measurements were performed by using customized instruments that are installed at the IMEM-CNR Institute in Parma (Italy): vibrating sample magnetometer (VSM), alternating gradient force magnetometer (AGFM) and superconducting quantum interference device (SQUID).

References

[1] V. I. Shubayev, T. R. Pisanic II and S. Jin, *Adv. Drug Deliver Rev.*, 2009, 61 (6), 467-477.

[2] R. Hao, R. Xing, Z. Xu, Y. Hou, S. Gao and S. Sun, *Adv. Mater.*, 2010, 22, 2729-2742.

[3] N. Tran and T. J. Webster, *J. Mat. Chem.*, 2010, 20, 8760-8767.

[4] J.B. Haun, T.J. Yoon, H. Lee and R. Weissleder, *WIREs Nanomed. Nanobiotechnol.* 2010, 2, 3, 291-304.

[5] J. H. Jung, J. H. Lee and S. Shinkai, *Chem. Soc. Rev.*, 2011, 40, 4464-4474.

[6] S. Jiang, K. Y. Win, S. Liu, C. P. Teng, Y. Zheng and M.Y. Han, *Nanoscale*, 2013, 5, 3127-3148.

[7] S. Sun, C.B. Murray, D. Weller, L. Folks, and A. Moser, *Science*, 2000, 287(5460), 1989-1992.

[8] H. Zeng and S. Sun, *Adv. Funct. Mater.*, 2008, 18, 391-400.

[9] F. Liu, Y. Hou and S. Gao, *Chem. Soc. Rev.*, 2014, 43, 8098-8113.

[10] N. Lee and T. Hyeon, *Chem. Soc. Rev.*, 2012,41, 2575-2589.

[11] Y. Jin, C. Jia, S.W. Huang, M. O'Donnel and X. Gao, *Nat. Commun.*, 2010, 1, 41.

[12] R. Weissleder, M. Nahrendorf and M. J. Pittet, *Nat. Mater.*, 2014, 13, 125-138.

[13] A. Schroeder, D. A. Heller, M. M. Winslow, J. E. Dahlman, G. W. Pratt, L. Langer, T. Jacks and D. G. Anderson, *Nat. Rev. Cancer*, 2012, 12, 1, 39-50.

[14] A. C. Anselmo, V. Gupta, B. J. Zern, D. Pan, M. Zakrewsky, V. Muzykantov and S. Mitragotri, *ACS Nano*, 2013, 7, 12, 11129–11137.

[15] T. Todd, Z. Zheng, W. Tang, H. Chen, G. Wang, Y.J. Chuang, K. Deaton, Z. Pan and J. Xie, *Nanoscale*, 2014,6, 2073-2076.

[16] Q A Pankhurst, N T K Thanh, S K Jones and J Dobson, *J. Phys. D: Appl. Phys.*, 2009, 42, 224001.

[17] L. Asín, M. R. Ibarra, A. Tres and F. Goya, *Pharmaceut. Res.*, 2012, 29, 5, 1319-1327.

[18] C. Blanco-Andujar, D. Ortega, P. Southern, Q. A. Pankhurst and N. T. K. Thanh, *Nanoscale*, 2015, 7, 1768-1775.

[19] A. Bhirde, J. Xie, M. Swierczewska and X. Chen, *Nanoscale*, 2011, 3, 142-153.

[20] A. Quarta, D. Bernareggi, F. Benigni, E. Luison, G. Nano, S. Nitti, M. C. Cesta, L. Di Ciccio, S. Canevari, T. Pellegrino and M. Figini, *Nanoscale*, 2015, DOI: 10.1039/C4NR04426F.

[21] J. Garcia, Y. Zhang, H. Taylor, O. Cespedes, M. E. Webba and D. Zhou, *Nanoscale*, 2011, 3, 3721-3730.

[22] A. McNally, *Nat. Nanotechnol.*, 2013, 8, 315–316.

[23] R. M. Cornell and U. Schwertmann, *The Iron Oxides: Structure, Properties, Reactions*, *Occurences and Uses*, Wiley-VCH, 2004.

[24] M. Okube, T. Yasue and S. Sasaki, *J. Synchrotron Rad.*, 2012, 19, 759-767.

[25] L. Neel, *Ann. Phys. Fr.*, 1948, 3-137.

[26] L. Neel, *C. R. Acad. Sci.*, 1949, 664-668.

[27] S. Bedanta and W. Kleemann, *J. Phys. D: Appl. Phys.*, 2009, 42, 013001.

[28] D. Sellmyer and R. Skomski, *Advanced Magnetic Nanostructures*, Springer, 2006.

[29] L. Neel, *Ann. Geophys.*, 1949, 5, 99.

[30] W. F. Jr. Brown, *Phys. Rev.*, 1963, 130, 1677.

[31] Q. A. Pankhurst, J. Connolly, S. K. Jones and J. Dobson, *J. Phys. D: Appl. Phys.*, 2003, 36, R167-R181.

[32] R.E. Rosensweig, *J. Magn. Magn. Mater.*, 2002, 252, 370–374.

[33] J. Carrey, B. Mehdaoui and M. J. Respaud, J. *Appl. Phys.*, 2011, 109, 083921.

[34] R. Ramprasad, P. Zurcher, M. Petras, M. Miller and P. Renaud, *J. Appl. Phys.*, 2004, 96, 519.

[35] A. Planes, E. Obradó, A. Gonzàlez-Comas and L. Mañosa, *Phys. Rev. Lett.*, 1997, 79, 3926.

[36] K. Ullakko, J. K. Huang, C. Kantner, R. C. O' Handley and V. V. Kokorin, *Appl. Phys. Lett.*, 1996, 69, 1966;

[37] A. Sozinov, N. Lanska, A. Soroka and W. Zou, *Appl. Phys. Lett.*, 2013, 102, 021902.

[38] A. Backen, S. R. Yeduru, A. Diestel, L. Schultz, M. Kohl and S. Fähler, *Adv. Eng. Mater.*, 2012, DOI: 10.1002/adem.201200069.

[39] I. Karaman, B. Basaran, H. E. Karaca, A. I. Karsilayan and Y. I. Chumlyakov, *Appl. Phys. Lett.*, 2007, 90, 172505.

[40] M. Gueltig, H. Ossmer, M. Ohtsuka, H. Miki, K. Tsuchiya, T. Takagi and M. Kohl, *Adv. Energy Mater.*, 2014, 4, 17.

[41] J. Ma and I. Karaman, *Science*, 2010, 327, 1468.

[42] A. Sozinov, A. A. Likhachev, N. Lanska and K. Ullakko, *Appl. Phys. Lett.*, 2002, 80, 1746.

[43] E. Pagounis, R. Chulist, M. J. Szczerba and M. Laufenberg, *Appl. Phys. Lett.*, 2014, 105, 052405.

[44] I. Aaltio, A. Soroka, Y. Ge, O. Söderberg and S. P. Hannula, *Smart Mater. Struct.*, 2010, 19, 075014.

[45] R. Kainuma, Y. Imano, W. Ito, Y. Sutou, H. Morito, S. Okamoto, O. Kitakami, K. Oikawa, A. Fujita, T. Kanomata and K. Ishida, *Nature*, 2006, 439, 957.

[46] M. Ohtsuka, M. Sanada, M. Matsumoto, K. Itagaki, *Mater. Sci. Eng. A*, 2004, 378, 377.

[47] A. J. Bradley, J. W. Rodgers, *Proc. R. Soc. A*, 1933, 144, 852, 340-359.

[48] International Center for Diffraction Data, PDF Number: 00-050-1518.

[49] P. J. Webster, K. R. A. Ziebeck, S. L. Town and M.S. Peak, *Philos. Mag. B*, 1984, 49, 295.

[50] V. A. Chernenko, *Sci. Mater.*, 1999, 40, 523.

[51] N. Lanska, O. Söderberg, A. Sozinov, Y. Ge, K. Ullakko and V. K. Lindroos, *J. Appl. Phys.*, 2004, 95, 8074.

[52] K. Bhattacharya, *Microstructure of Martensite*, Oxford Univ. Press, 2003.

[53] V. V. Martynov, *Journ. de Phys. IV*, 1995, C8, 91.

[54] J. Pons, V. A. Chernenko, R. Santamaria, E. Cesari, *Acta Mater.*, 2000, 48, 3027.

[55] J. Pons, R. Santamaria, V. A. Chernenko, E. Cesari, *Mater. Sci. Eng. A*, 2006, 438-440, 931.

[56] L. Righi, F. Albertini, L. Pareti, A. Paoluzi and G. Calestani, *Acta Mater.*, 2007, 55, 15, 5237-5245.

[57] L. Righi, F. Albertini, E. Villa, A. Paoluzi, G. Calestani, V. Chernenko, S. Besseghini, C. Ritter and F. Passaretti, *Acta Mater.*, 2008, 56, 16, 4529-4535.

[58] S. Singh, V. Petricek, P. Rajput, A. H. Hill, E. Suard, S. R. Barman and D. Pandey, *Phys. Rev. B*, 2014, 90, 014109.

[59] Z. Nishiyama, *Martensite Transformation*, Academic Press, New York, 1978.

[60] S. J. Murray, M. Marioni, S. M. Allen, R. C. O'Handley and T. A. Lograsso, *Appl. Phys. Lett.*, 2000, 77, 886.

[61] R. Tickle and R. D. James, *J. Magn. Magn. Mater.*, 1999, 195, 3, 627-638.

[62] V.A. Chernenko, V.A. Lvov, S. Besseghini, Y. Murakami, *Scripta Mater.*, 2006, 55, 4, 307-309.

[63] A.T. Onisan, A.N. Bogdanov, U.K. Rößler, *Acta Mater.*, 2010, 58, 13, 4378-4386.

[64] O. Heczko, *IEEE Trans. Magn.*, 2014, 50, 11, 2505807.

[65] L. Straka, O. Heczko, H. Seiner, N. Lanska, J. Drahokoupil, A. Soroka, S. Fähler, H. Hänninen and A. Sozinov, *Acta Mater.*, 2011, 59, 20, 7450-7463.

[66] J. W. Dong, J. Q. Xie, J. Lu, C. Adelmann, C. J. Palmstrøm, J. Cui, Q. Pan, T. W. Shield, R. D. James and S. McKernan, *J. Appl. Phys.*, 2004, 95, 2593.

[67] M. A. Herman, W. Richter and H. Sittner, *Epitaxy: Physical Principles and Technical Implementation*, Springer, Berlin, 2003.

[68] J. W. Dong, L. C. Chen, C. J. Palmstrøm, R. D. James and S. McKernan, *Appl. Phys. Lett.*, 1999, 75, 1443.

[69] J. W. Dong, J. Q. Xie, J. Lu, C. Adelmann, C. J. Palmstrøm, J. Cui, Q. Pan, T. W. Shield, R. D. James and S. McKernan, *J.Appl. Phys.*, 2004, 95, 2593.

[70] G. Jakob and H.J. Elmers, *J. Magn. Magn. Mater.*, 2007, 310, 2, 3, 2779-2781.

[71] P. Pörsch, M. Kallmayer, T. Eichhorn, G. Jakob, H. J. Elmers, C. A. Jenkins, C. Felser, R. Ramesh and M. Huth, *Appl. Phys. Lett.*, 2008, 93, 2, 022501.

[72] O. Heczko, M. Thomas, J. Buschbeck, L. Schultz and S. Fähler, *Appl. Phys. Lett.*,

2008, 92, 7, 072502.

[73] P. Ranzieri, S. Fabbrici, L. Nasi, L. Righi, F. Casoli, V. A. Chernenko, E. Villa and F. Albertini, *Acta Mater.*, 2013, 61, 263.

[74] M. Thomas, O. Heczko, J. Buschbeck, U. K. Rößler, J. McCord, N. Scheerbaum, L. Schultz and S. Fähler, *New J. Phys.*, 2008, 10, 023040.

[75] International Center for Diffraction Data, PDF Number: 00-004-0829.

[76] M. Thomas, O. Heczko, J. Buschbeck, L. Schultz, and S. Fähler, *Appl. Phys. Lett*., 2008, 92, 192515.

[77] M. Thomas, O. Heczko, J. Buschbeck, Y. W. Lai, J. McCord, S. Kaufmann, L. Schultz and S. Fähler, *Adv. Mat.,* 2009, 21, 3708.

[78] . Backen, S. R. Yeduru, M. Kohl, S. Baunack, A. Diestel, B. Holzapfel, L. Schultz and S. Fähler, *Acta Mater.*, 2010, 58, 9, 3415-3421.

[79] C. A. Jenkins, R. Ramesh, M. Huth, T. Eichhorn, P. Pörsch, H. J. Elmers, and G. Jakob, *Appl. Phys. Lett*., 2008, 93, 234101.

[80] S. Priya, *J. Electroceram*., 2007, 19, 167.

[81] Y. Chiu, C.-T. Kuo and Y.-S. Chu, *Microsyst. Technol*., 2007, 13, 1663.

[82] G. J. Snyder, J. R. Lim, C.-K. Huang and J. P. Fleurial, *Nat. Mater*., 2003, 2, 528.

[83] M. Gueltig, H. Ossmer, M. Ohtsuka, H. Miki, K. Tsuchiya, T. Takagi, and M. Kohl, *Adv. Energy Mater.*, 2014, 4, 1400751.

[84] D. B. Williams, C. B. Carter, *Transmission Electron Microscopy. A Textbook for Materials Science*, Springer, 2009.

[85] P. B. Hirsch, A. Howie, R. B. Nicholson, D. W. Pashley and M. J. Whelan, *Electron microscopy of thin crystals*. 1977, Krieger, New York.

[86] F. A. Lenz, *Electron Microscopy in Material Science*, Academic Press, 1971, 540.

[87] L. Reimer and H. Kohl, *Transmission Electron Microscopy: Physics of Image Formation*, Springer, 2008.

[88] R. Erni, *Aberration-corrected Imaging in Transmission Electron Microscopy*, Imperial College Press, 2010.

[89] S. J. Pennycook, P. D. Nellist, *Scanning Transmission Electron Microscopy: Imaging and Analysis*, Springer, 2011.

[90] A. C. Twitchett, R. E. Dunin-Borkowski and P. A. Midgley, *Phys. Rev. Lett*., 2002, 88, 238302.

[91] M. Hÿtch, F. Houdellier, F. Hüe and E. Snoeck, *Nature*, 2008, 453, 1086-1089.

[92] Y. Murakami, J. H. Yoo, D. Shindo, T. Atou and M. Kikuchi, *Nature*, 2003, 423, 965-968.

[93] S. Seki, X. Z. Yu, S. Ishiwata, Y. Tokura, *Science*, 336, 6078, 198-201.

[94] M. Lehmann, H. Lichte, D. Geiger, G. Lang, E. Schweda, *Mater. Charact*., 1999, 42, 4–5, 249-263.

[95] P. A. Midgley and R. E. Dunin-Borkowski, *Nat. Mater*., 2009, 8, 271-280.

[96] M. J. G. Cottet, M. Cantoni, B. Mansart, D. T. L. Alexander, C. Hébert, N. D. Zhigadlo, J. Karpinski and F. Carbone, *Phys. Rev. B*, 2013, 88, 014505.

[97] D. Shindo, Y. G. Park, Y. Murakami, Y. Gao, H. Kanekiyo and S. Hirosawa, *Scr. Mater*., 2003, 48, 851

[98] D. Shindo, Y. Murakami, J. *Phys. D: Appl. Phys*., 2008, 41, 183002;

[99] T. Kasama, R. E. Dunin-Borkowski and M. Beleggia, *Electron Holography of Magnetic Materials, Holography-Different Fields of Application*, 2011, Dr. Freddy Monroy Ed.

[100] Y. Aharonov and D. Bohm, Phys. Rev., 1959, 115, 485.

[101] K. Keimpema, H. De Raedt and J. Th. M. De Hosson, *J. Comput. Theor. Nanos*., 2006, 3, 3,362-374.

[102] A. Tonomura, T. Matsuda, J. Endo, T. Arii and K. Mihama, *Phys. Rev. B*, 1986, 34, 3397.

[103] R. E. Dunin-Borkowski, M. R. McCartney, B. Kardynal and D. J. Smith, *J. Appl. Phys*., 1998, 84, 374.

[104] C. Phatak, M. Beleggia and M. De Graef, *Ultramicroscopy*, 2008, 108, 6, 503-513.

[105] J. Sickmann, P. Formánek, M. Linck, U. Muehle and H. Lichte, *Ultramicroscopy*, 2011, 111, 4, 290-302.

[106] H. Lichte, *Ultramicroscopy,* 2008, 108, 3, 256-262.

[107] S. Amelinckx, D. van Dyck, J. van Landuyt and G. van Tendeloo, *Electron Microscopy: Principles and Fundamentals*, Wiley, 1997.

[108] M. R. Teague, *J. Opt. Soc. Am*., 1983, 73, 1434-1441.

[109] D. Paganin and K. A. Nugent, *Phys. Rev. Lett.,* 1998, 80, 2586-2589.

[110] T. E. Gureyev and K. A. Nugent, *JOSA A*, 1996, 13, 8, 1670-1682.

[111] V.V. Volkov, Y. Zhu, M. De Graef, *Micron*, 2002, 33, 5, 411-416.

[112] P. A. Midgley and R. E. Dunin-Borkowski, *Nat. Mater*., 2009, 8, 271–280.

[113] E. Meyer, H. H. R. Bennewitz, *Scanning Probe Microscopy: The Lab on a Tip*, Springer-Verlag, Berlin, 2003.

2 The role of dipolar interactions in magnetic hyperthermia unveiled by Lorentz microscopy

2.1 Introduction

In the recent past, a great effort has been devoted to the research of new nanostructured materials with functional properties that can be exploited in biomedical applications [1]. As already described in Section 1.2.3, magnetic NPs in the superparamagnetic state are suitable for both diagnostic and therapeutic approaches: in the field of diagnostics, they have been proposed as contrast agent to enhance the signal in the MRI techniques [2-5], while in the field of therapeutics they can be used as magnetic vectors for drug delivery [6-9] and/or heat mediators in hyperthermia treatment [10, 11].

The magnetic hyperthermia, performed applying radiofrequency magnetic

fields, can be effectively employed to locally induce cancer cells death, thanks to the generated heat [12] and the localized destructive effect over the cellular membrane [13]. The capability of a suspension of magnetic NPS to behaves as a good hyperthermic mediator is measured by the specific power absorption value (see Section 1.2.3.4) that represents the thermal power generated by the unit mass of the magnetic NPs under an applied AC field.

The transformation of the AC field energy into heat can occur by several mechanisms with a global efficiency that strongly depends on the amplitude and frequency of the applied magnetic field as well as on the structural and morphological properties of the NPs, in particular their size and shape, the inter-particles interactions [14]. The ability to tune these parameters in a controlled way gives the possibility to improve the efficiency of the hyperthermic process, allowing the reduction of the NPs amounts necessary to generate the requested heat or permitting the use of lower fields frequencies and amplitudes. Today, the work of the scientific community for the achievement of this aim is conducted following different ways, choosing different materials [15,16], optimizing the NPs size [17,18] and changing the NPs shape [19,20].

From the magnetic point of view, the choice of the material is usually driven by the requirement of high magneto-crystalline anisotropy, an intrinsic parameter that depends on the crystalline structure and composition. The magneto-crystalline anisotropy term, in fact, strongly influences the shape of the hysteresis loop and the critical size for the transition from the superparamagnetic to the blocked regime. In particular, higher is the anisotropy value smaller is the critical size. At the same time, this intrinsic property also influences the hyperthermic efficiency of the NPs, which has been demonstrated to have a maximum in proximity of the critical size for the transition between the two regimes [21]. Also the variation of the NPs shape can produce an increase of the magnetic anisotropy adding two non-negligible terms, the shape anisotropy, which is directly related to the shape of the magnetic NPs, and the surface anisotropy, which is influenced by the

faceting of the magnetic NPs [22, 23].

Among the different biocompatible magnetic materials, magnetite has been widely employed since it can be obtained in big amounts and by easy synthesis routes in nanostructured forms, with a good control of size and shape [24, 25]. The SPA of magnetite NPs under an applied AC field is mainly due to two kinds of power loss mechanisms, the hysteresis and relaxation losses [26], while the contribution from eddy currents is negligible owing to the low conductivity of magnetite [27]. Both the contributing mechanisms are strongly influenced by the NPs size [25].

In superparamagnetic NPs the absence of coercivity and remanence prevents the establishing of magnetic inter-particle interactions avoiding the formation of NPs aggregates. In real systems, however, magnetic NPs can interact and the NPs system can show a remarkable tendency toward a non-homogeneous state in which clusters of different size are observed. Beside this morphological fingerprint unveiling a deviation from the ideal system of superparamagnetic NPs, the dipolar interactions that arise among NPs can also strongly influence the heating ability of the colloidal suspension.

The effects of the dipolar interactions on the hyperthermia of an assembly of magnetic NPs, however, are still not completely understood. This open point gives rise to controversial hypothesis about the role that dipolar interactions play in magnetic hyperthermia processes. In the next Section, the most relevant hypothesis proposed by the scientific community will be reported and summarized.

In order to investigate the effects of the dipolar interactions on the magnetic hyperthermia, two systems consisting in magnetite NPs with the same size distribution but different degrees of interaction have been synthetized. The details on the synthesis routes will be reported in Section 2.3. In the Section 2.4 the structural and morphological characterizations will be reported. These results are complemented and supported by the magnetic characterizations. Finally, in Section 2.5 a novel way to correlate the magnetic hyperthermic behaviours to the dipolar interactions in the NPs suspensions

exploiting Lorentz microscopy will be presented. In particular, visualizing and mapping the inter-particles interactions it is possible to make reliable hypothesis on the power losses mechanisms for different NPs aggregates and understand the interactions effects on the performance of different NPs suspensions as hyperthermic mediators.

2.2 The effects of dipolar interactions on hyperthermia: controversial hypothesis

The role of magnetic dipolar interaction on hyperthermia has not been completely understood and controversial hypothesis are reported in the literature. Some authors have reported a decrease of the SPA value with increasing the aggregation state of the NPs, whereas other authors found a beneficial effect of the dipolar interaction on the SPA value. In the following, an overview over the different opinions is reported.

Urtizberea et al. [28] have reported a remarkable decrease of the SPA values with increasing the nanoparticle concentration in monodispersed maghemite NPs suspensions; this decrease has been related to two main effects: (i) a decrease of the static susceptibility with particles concentration, meaning that the increase of dipolar interactions makes the NPs more stable against field orientation; (ii) a decrease of relaxation times with the increase of the interactions, producing a faster NPs relaxation.

De la Presa et al. [29] have shown that an increase of maghemite nanoparticle concentration can induce the formation of nanoparticles clusters, which don't affect the observed SPA values.

Serantes et al. [30] have performed Monte Carlo simulations to demonstrate that an increase in the dipolar interaction intensity induces a change of the energy barrier, changing the global magnetic behaviour of the system; in particular, they observed a decrease in the magnetic susceptibility and the

hysteresis losses, which affects the hyperthermia process diminishing its efficiency.

Sadat et al. [31], taking into account different systems based on magnetite NPs, have asserted that the dipolar interactions are the crucial parameter that should be reduced in the design and synthesis of Fe_3O_4 NPs for magnetic hyperthermia, being an increase of the interactions counterproductive for the hyperthermic process.

On the contrary, Martinez-Boubeta et al. [32] have observed an increase of the SPA values with increasing the concentration of Fe-MgO single-domain NPs suspension up to the point in which the magnetic interactions between particles become comparable to the anisotropy field.

Burrows et al [33] have shown an enhanced energy loss for small FePt NPs, thanks to an enhancement of the energy barrier due to dipolar interactions.

Jeun et al. [34] reported a significant increase of the SPA value in soft ferromagnetic NPs of ferrites obtained by the control of inter-particle dipolar interactions; the remarkable enhancement of the SPA was mainly attributed to an increase in the magnetic hysteresis and relaxation losses, resulting from the increase in magnetic moment and susceptibility induced by the dipolar interactions.

From the theoretical point of view, Landi [35] has recently proposed a model which asserts that the SPA can increase or decrease depending on the σ value (representing the ratio between the height of the energy barrier (see Section 1.2.2) and the thermal energy, $\sigma = KV/k_BT$). For small fields amplitudes, assuming a linear response theory (see Eq. 1.11 and Eq. 1.12 in Section 1.2.3.4) it is possible to approximate the SPA value as:

$$SPA \approx \frac{\omega\tau}{1+(\omega\tau)^2} \tag{3.1}$$

where $\tau \approx e^{\sigma}$ is the relaxation time and $\omega = 2\pi f$. From the Eq. (3.1) derives that in order to optimize the SPA, the frequency should be set to a value, which satisfies the condition $\omega\tau \approx 1$. This condition defines a σ_{opt}, which maximizes the SPA. The σ for the considered systems can be lower or higher than the

optimal value σ_{opt} for a fixed alternating field frequency. For $\sigma < \sigma_{opt}$, the system is in the "*low-barrier regime*" where the magnetization jumps between different stable states are frequent but the energy released in each jump is small. Increasing the dipolar interactions, the anisotropy barrier increases thus taking the system closer to the optimal condition, which maximizes the SPA: in this regime dipolar interactions have a beneficial effect on the SPA value.

On the contrary, for $\sigma > \sigma_{opt}$ the system is in the "*high-barrier regime*" where the field is not very effective in promoting the jumps. In this regime the dipolar interactions have a counterproductive effect, increasing even more the barrier height. Even if this theoretical model includes both the two possible opposite behaviours, an in-depth analysis correlating the morphology of the interaction-induced nanoparticles aggregates to the hyperthermic behaviour of the NPS suspension is still lacking.

In this Chapter, a novel way to visualize and map the inter-particles interactions exploiting the Lorentz microscopy will be presented. The investigation was carried out on a system consisting in magnetite NPs with different degrees of interaction. In order to study a strongly interacting system, magnetite NPs were synthetized by co-precipitation method without adding any stabilizing surfactant. In comparison, a weakly interacting system was synthetized by the thermal decomposition synthesis route, which makes use of a surfactant permitting to obtain a stable and dispersed system.

Until now the Lorentz microscopy has never been exploited to investigate the effects of dipolar magnetic interactions on the performance of nanoparticles suspensions as hyperthermic mediators: in the proposed analysis the macroscopic hyperthermic behaviour will be correlated to the aggregation state at the sub-micrometric scale, paving the way to the comprehension of the power losses mechanisms for NPs aggregates with different degrees of dipolar interactions.

2.3 Synthesis of magnetite nanoparticles

2.3.1 Synthesis by co-precipitation

The synthesis of magnetite NPs by co-precipitation route was carried out following the procedure reported in [36] and schematically depicted in Fig. 2.1a.

In particular, 4 g of $FeCl_2 \cdot 4H_2O$ (20 mmol) were added to a solution of 11 g of $FeCl_3 \cdot 6H_2O$ (40 mmol) in 120 mL of deionized water. The solution was heated at 360 K under argon atmosphere. The pH value of the solution was then adjusted to 10 by the addition of concentrated aqueous ammonia. The magnetite formation started immediately. After stirring for 4 h under argon atmosphere the reaction was cooled to room temperature. At RT, the NPs were washed several times with deionized water to remove the excess of ammonia. The black precipitate was collected by magnetic decantation, dried under high vacuum and characterized. The product is easily redispersible in aqueous solution by sonicating for 10 min.

2.3.2 Synthesis by thermal decomposition

The synthesis by thermal decomposition was performed employing a slightly modified version of the procedure reported in [37] and summarized in Fig. 2.1b. $Fe(acac)_3$ (2 mmol), 1,2-hexadecanediol (10 mmol), oleic acid (6 mmol) and oleylamine (6 mmol) were mixed in 20 mL of benzyl ether under N_2 flow.

The mixture was heated at 473 K for 2 h and then heated to reflux (~573 K) for 1 h under an N_s blanket. When the black-brown mixture reached RT, ethanol (40 mL) was added. A black material was precipitated and separated by centrifugation (5000 rpm, 15 min). The product is easily redispersible in hexane.

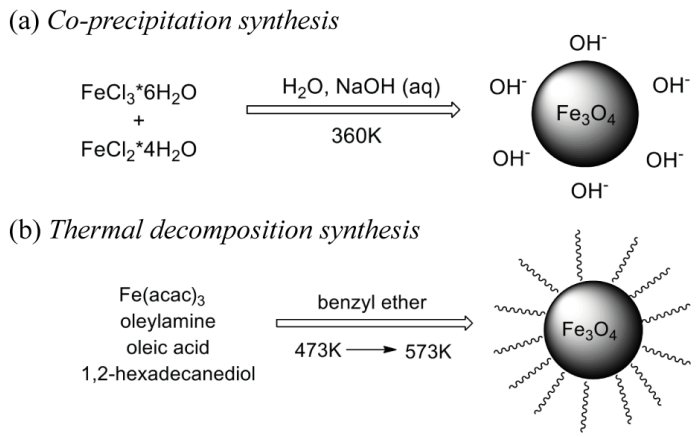

Fig. 2.1 Schematic representation of the two synthesis routes: (a) co-precipitation, (b) thermal decomposition.

2.4 A comparative system: the tuning of the interaction degree by controlling the surface stabilization

In this Section, the comparative system is studied in detail in order to achieve a deeper comprehension of the role of dipolar interactions on hyperthermia; in particular, the results concerning the structural and morphological characterizations, performed mainly by transmission electron microscopy, will be discussed.

2.4.1 Morphological and structural characterizations of the specimens

The morphological and structural characterizations have been performed mainly by transmission electron microscopy, employing the techniques of conventional bright field imaging, HRTEM and selected area electron diffraction; a complementary characterization finalized to investigate the properties of the NPs in the colloidal suspension has been carried out by means of dynamic light scattering (DLS).

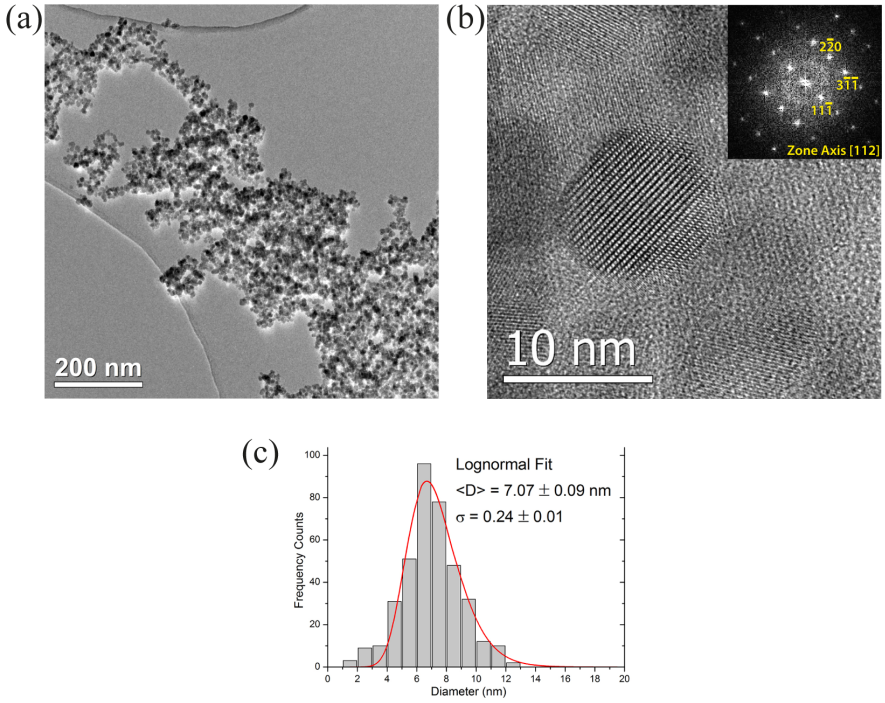

Fig. 2.2 TEM characterization of magnetite NPs synthetized by co-precipitation. (a) Low magnification bright field image. (b) HRTEM image; the inset shows the FFT of a square area containing the nanoparticle in the centre of the image. (c) NPs size distribution.

The morphology of the sample synthetized by co-precipitation method clearly points out a strong tendency of the NPs to create aggregates on a scale of several hundreds of nanometres. In the bright field TEM image taken at 25k magnification and reported in Fig. 2.2a, in fact, it is possible to observe a strong agglomeration of the nanoparticles. As can be observed from the HRTEM image shown in Fig. 2.2b, the obtained sample consists of NPs of nearly spherical shape with homogeneous size distribution centred around 7 nm. Each particle is a single crystal of magnetite, as clearly pointed out by the FFT of the particle in the centre of the HRTEM image, shown in the inset of Fig. 2.2b. The NPs size histogram (Fig. 2.2c) obtained from a relevant statistical sampling has been fitted with lognormal distribution, which correctly describes the asymmetric shape of the experimental size distribution [38].

The transmission electron microscopy analysis performed on NPs synthetized by thermal decomposition method points out that the obtained sample consist of well-stabilized particles of spherical shape, as can be seen in the TEM image reported in Fig. 2.3a. Each particle is a single crystal of magnetite, as clearly indicated by atomic lattice fringes in HRTEM image (shown in Fig. 2.3b) and by the spots in the Fourier transform of the particle in the centre of the image (inset of Fig. 2.3b). The nanoparticles have a homogeneous and narrow size distribution centred around 6.5 nm (Fig. 2.3c).

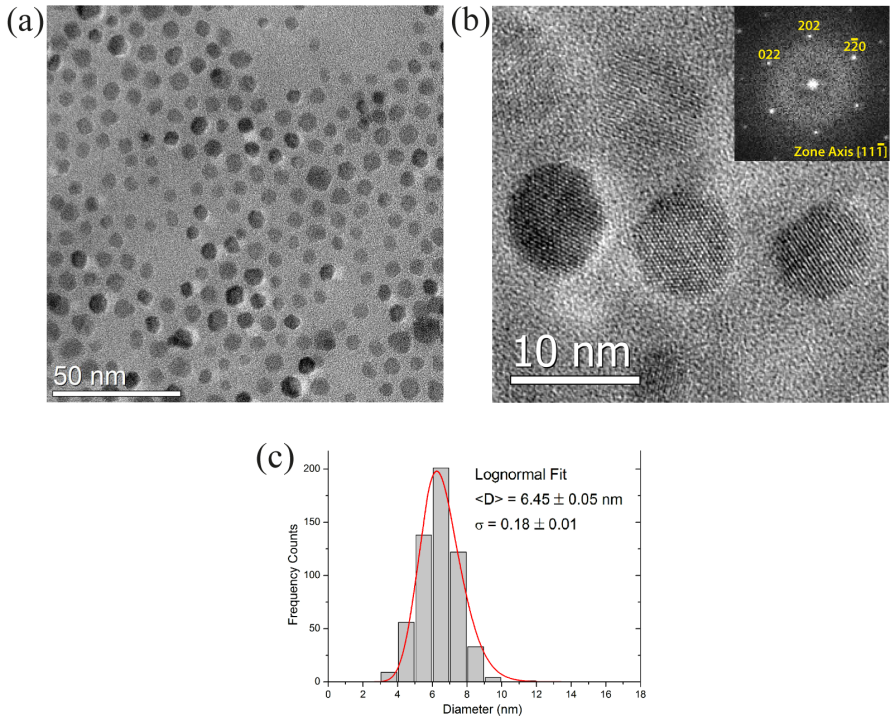

Fig. 2.3 TEM characterization of magnetite NPs synthetized by thermal decomposition. (a) Low magnification bright field image. (b) HRTEM image; the inset shows the FFT of a square area containing the nanoparticle in the centre of the image. (c) NPs size distribution.

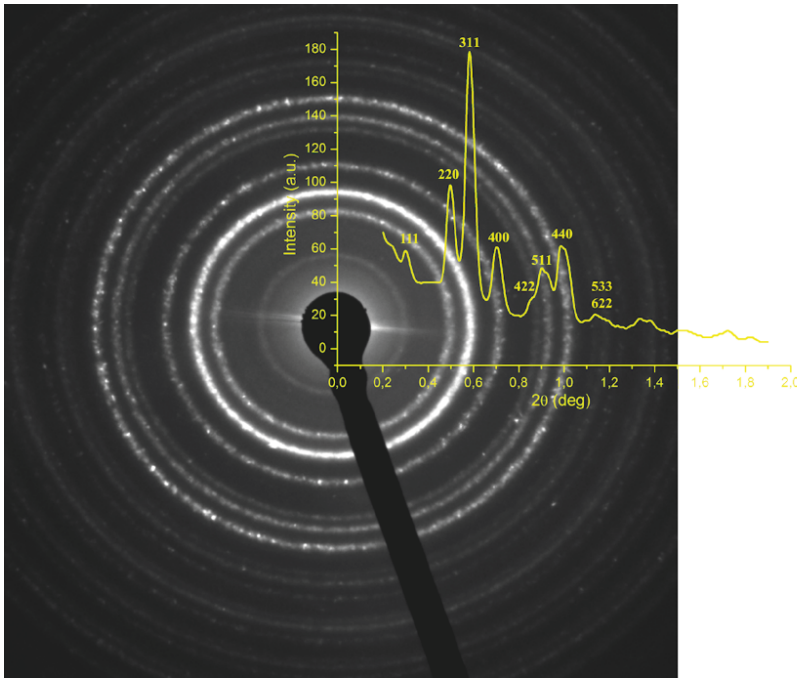

Fig. 2.4 Electron diffraction pattern obtained for the co-precipitated NPs. The spectrum obtained by an angular integration of the diffraction rings, in which the main reflections are indexed, is superimposed to the image.

Peaks	d_{exp} (nm)	d (nm) [ICSD]
111	0.49	0.4858
220	0.30	0.2975
311	0.25	0.2537
400	0.21	0.2103
422	0.17	0.1717
511	0.16	0.1619
440	0.15	0.1487

Table 2.1 The measured d-spacings are reported in comparison to literature reference values (ICSD#: 082451) for magnetite.

Electron diffraction from a large area of the sample was employed to achieve structural information about the NPs. In particular, the positions of the peaks and their relative intensities in the obtained diffraction pattern match very well the typical ones of magnetite powder (ICSD#: 082451), for both the investigated samples. In Fig. 2.4 the diffraction pattern obtained for the co-precipitated sample is reported; in Table 2.1, the measured d-spacings are

reported and compared to the reference values from the crystallographic database.

The results of the characterizations performed by dynamic light scattering are reported in Table 2.2. From the comparison of the values obtained by the two different characterizations it is possible to conclude that the particles synthetized by co-precipitation show a stronger tendency to agglomerate and create aggregates, whose mean hydrodynamic radius (R_H) is around 100 nm with a broad size distribution. The particles synthetized by thermal decomposition are very stable and well dispersed with a narrow size distribution thanks to the organic shell provided by the surfactant, which acts as steric stabilizer preventing the agglomeration.

Sample	$<R_H>$(nm)	σ
Co-precipitation	97	0.49
Thermal decomposition	10	0.24

Table 2.2 Mean values and distribution widths for the hydrodynamic radii in both the investigated samples, as obtain from DLS.

2.4.2 Magnetic characterization of the specimens

A complete magnetic characterization of the specimens has been carried out to investigate the magnetic properties of the NPs suspensions under an applied static magnetic field.

The magnetization loops were obtained either by alternating-gradient force magnetometer or by vibrating sample magnetometer; in both cases the maximum applied field was 2 T. The hysteresis loops measured at room temperature with an applied static field are reported in Fig. 2.5a, for both the described samples. The measurement clearly shows that the particles synthetized either by thermal decomposition or by co-precipitation have zero coercivity and remanence, even if they display very different aggregation states. These peculiar features of the magnetization curves clearly demonstrate that their behaviour at room temperature is superparamagnetic.

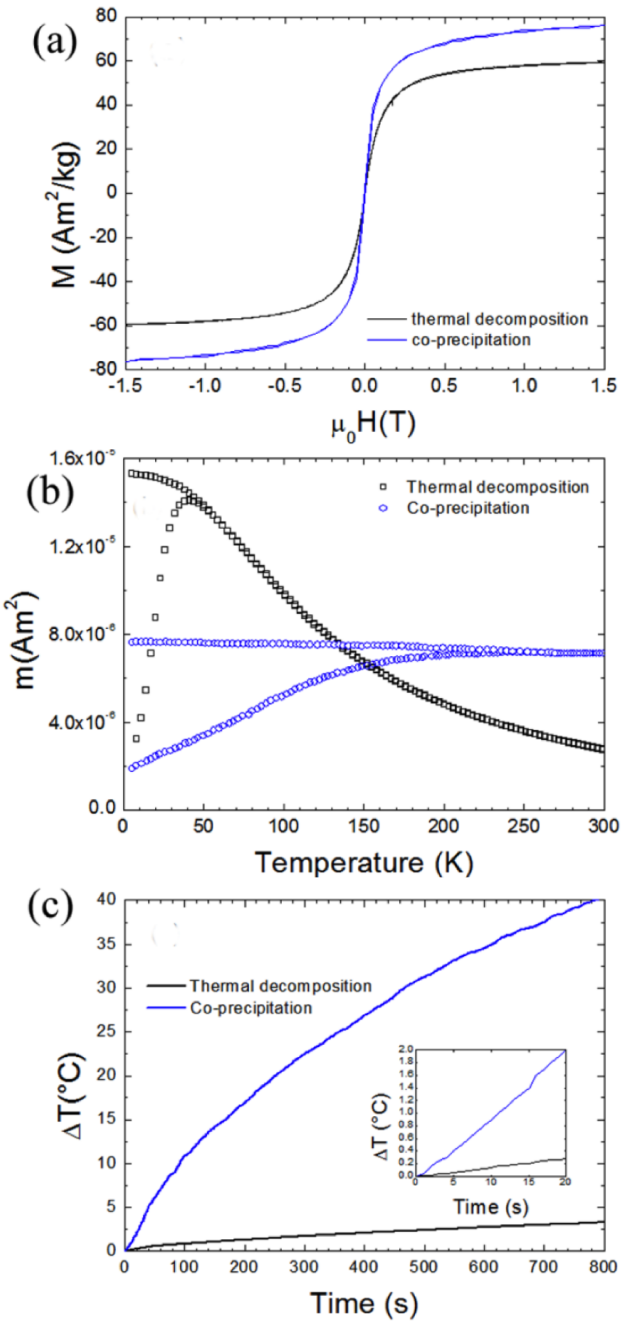

Fig. 2.5 (a) Magnetization loops for the two investigated samples at RT. (b) ZFC-FC curves for magnetic NPs obtained by thermal decomposition and co-precipitation. (c) Hyperthermia measurement: variation of the temperature as a function of time for both the samples. The inset shows the initial slope of the curves.

The NPs obtained by co-precipitation show a very high saturation magnetization (M_s) of 77 Am^2/kg. This value is very close to the bulk one [39]. The NPs synthesized by thermal decomposition have an M_s value of 60 Am^2/kg, after the subtraction of the organic shell weight that has been estimated by thermo gravimetric analysis (TGA). The relatively small difference between the observed M_s values can be attributed to a higher degree of crystallinity of the co-precipitated magnetic NPs, as commonly reported in literature [40].

In order to have a deeper insight into magnetic properties at room temperature, the ZFC and FC measurements have been performed with an applied field of 8 kA/m. Fig. 2.5b shows two very different dependences of the magnetization on temperature. In fact, even if the size distributions of the two samples are very similar (Fig. 2.2c and 2.3c), the magnetic NPs synthesized by thermal decomposition, thanks to the organic shell, are less interacting than the NPs obtained through co-precipitation in which no steric stabilization is present. In the latter case, as can be observed by TEM analysis (Fig. 2.2a) the magnetic NPs are in contact, thus meaning that dipolar interactions are more effective giving rise to a broad distribution of blocking temperatures and to a flat FC curve (Fig. 2.5b).

The observed magnetic behaviour demonstrates that the particles obtained by co-precipitation are so aggregated that, even if they are in the superparamagnetic state at room temperature, when ZFC-FC measurements are performed they do not behave as isolated NPs but as clusters of different sizes. This result is in good agreement with dynamic light scattering measurements in which a broad distribution ($\sigma = 0.49$) of hydrodynamic radii has been observed, peaked around 97 nm. On the contrary, the NPs obtained by thermal decomposition show a narrow size distribution ($\sigma = 0.24$) centred around 10 nm in the dynamic light scattering measurement. In agreement with the different observed value of the hydrodynamic radius, the ZFC-FC measurements on the NPs obtained by thermal decomposition show a very different behaviour: the FC curve is not as flat as in the case of the co-precipitated sample and the values for the characteristic temperatures (as

defined in Section 1.5.2) are: $T_S \approx 25$ K, $T_B \approx 40$ K, $T_I \approx 50$ K. The very narrow size distribution of the particles and the shape of ZFC-FC measurement highlight that the dipolar interactions in this system are less effective thanks to the organic shell, which allows the NPs to be well separated with mean inter-particle distances of 2-3 nm (Fig. 2.3a).

Despite the very different behaviours observed in ZFC-FC measurements, as already observed the magnetization curves of both samples exhibit a very similar trend characterized by zero coercivity and remanence, thus demonstrating their superparamagnetic properties at RT. The magnetization curves have been fitted using a Langevin function (see Section 1.2.2, Eq. 1.3). From the fitting of the curves, reported in Fig. 2.6, it is possible to estimate a mean value for the magnetic volume of the particles, for the two different systems. The diameters values corresponding to these mean volumes are reported in Table 2.3 for the co-precipitated sample and for the sample synthetized by thermal decomposition. The obtained values, related to the mean magnetic volumes, are in agreement with the size distributions obtained by TEM analysis and represent a further demonstration that the NPs constituting the clusters in the co-precipitated sample behave as single superparamagnetic NPs, even if strong inter-particles interactions are observed in ZFC-FC measurements.

The hyperthermia measurements (Fig. 2.5c) have been done on both samples with a maximum applied field of 12.7 kA/m at frequency of 235 kHz. The SPA for magnetic NPs synthesized by thermal decomposition is 3.4 W/g while the one of the sample obtained by co-precipitation is around 50 W/g. The huge difference in the SPA values is quite surprising considering that the particle size distributions and M_s values for the two systems are comparable. It is therefore evident that this difference originates from the establishing of dipolar interactions among the NPs obtained by the co-precipitation method, as suggested by the ZFC-FC measurements. In the following an analysis by Lorentz microscopy will be presented in order to achieve a deeper comprehension of the role of dipolar interactions in magnetic hyperthermia.

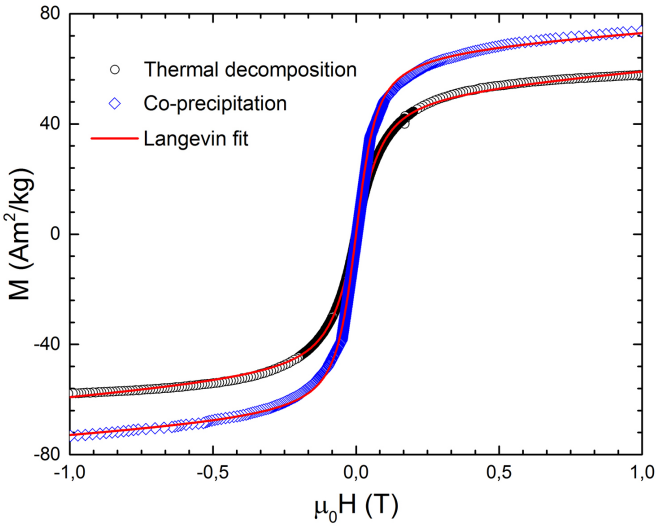

Fig. 2.6 Fitting of the magnetization curves M(H) with the Langevin function (red curve) for both the investigated samples.

Sample	TEM: <d> (nm)	Langevin: <d> (nm)
Co-precipitation	7.1 ± 0.1	9.3 ± 0.2
Thermal decomposition	6.5 ± 0.1	9.1 ± 0.1

Table 2.3 Mean diameters values obtained by TEM analysis and by the fitting of the magnetization curves with the Langevin function, for both samples synthetized by co-precipitation and thermal decomposition.

2.5 Mapping of the dipolar interactions by Lorentz microscopy

In order to visualize and map the interactions at the basis of this huge difference in the SPA values we exploited Lorentz microscopy, which represents a very powerful tool that allows retrieving the magnetic phase shift of the electron wavefunction and thus to reconstruct the in-plane magnetic induction among different magnetic NPs and clusters. Lorentz microscopy was performed on the JEOL JEM-2200FS microscope turning off the objective lens and using the objective mini-lens as a Lorentz lens. In this way, the specimens are inserted in the TEM column in a field-free environment.

Applying the TIE equation (Eq. 1.35) to a Fresnel focal series (each frame was acquired with an exposure of 1 sec), the phase can be retrieved (see Section 1.4.4.2 for details). The reconstruction has been directly computed within STEMCELL software exploiting the tool for Lorentz microscopy [41]. In order to isolate the electrostatic and magnetic contributions of the phase shift, a second focal series has been acquired after turning upside-down the sample. The separation method permits to isolate the magnetic phase shift in Lorentz microscopy [42] in a similar way to the commonly one employed in off-line electron holography (see Section 1.4.4.1). The phase images have been corrected in order to remove linear phase ramps.

Afterwards, a map of the in-plane projected magnetic induction can be directly obtained differentiating the magnetic phase shift and the magnetic induction flux lines can be visualized as the contour lines of equal phase shift, by computing a cosine map of the magnetic phase shift (see Section 1.4.4.3).

2.5.1 Visualization of the dipolar interactions

A Fresnel focal series acquired on the sample synthetized by co-precipitation method is shown in Fig. 2.7, where (a), (b) and (c) are the in-focus, over-focused and (c) the under-focused images respectively. As can be seen, the images cover a significant area of the sample; the field of view of the images is about 1.93 x 1.93 μm^2. The analysed portion of the sample noticeably evidences the presence of magnetic nanoparticles clusters and irregular chains. After acquiring a second Fresnel series after turning upside-down the specimen and applying the separation method, the mean inner potential and the magnetic phase shift can be obtained as half of the sum and half of difference, respectively, of the phase images obtained by the two focal series. The MIP and the magnetic phase shift are shown in Fig. 2.8a and b, respectively. The magnetic induction colour map, plotted superimposed to the contour lines of equal phase shift (obtained amplifying 10x the phase), is shown in Fig. 2.9a.

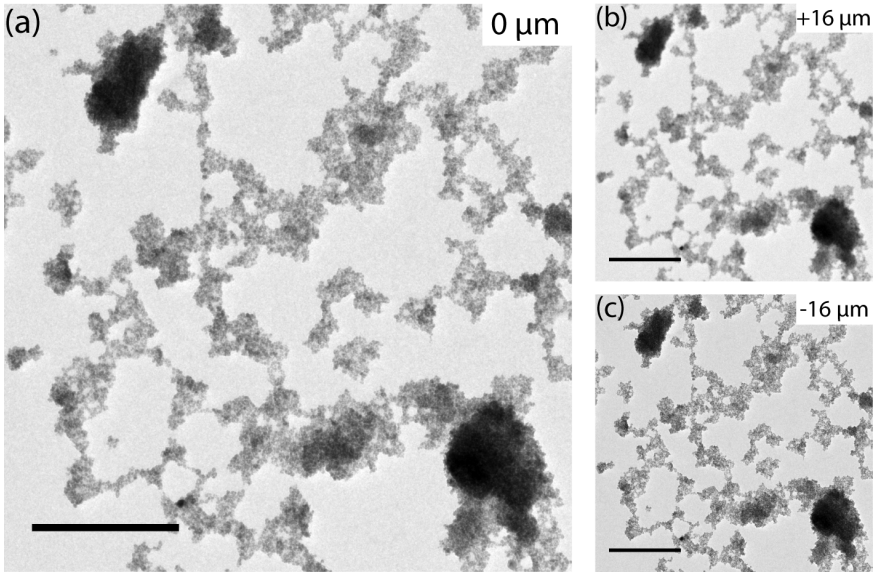

Fig. 2.7 Fresnel focal series on a significant portion of the sample synthetized by co-precipitation. (a) In-focus, (b) over-focused, (c) under-focused images. The bar in each image is 0.5 µm. The defocus step for the series is 16 µm.

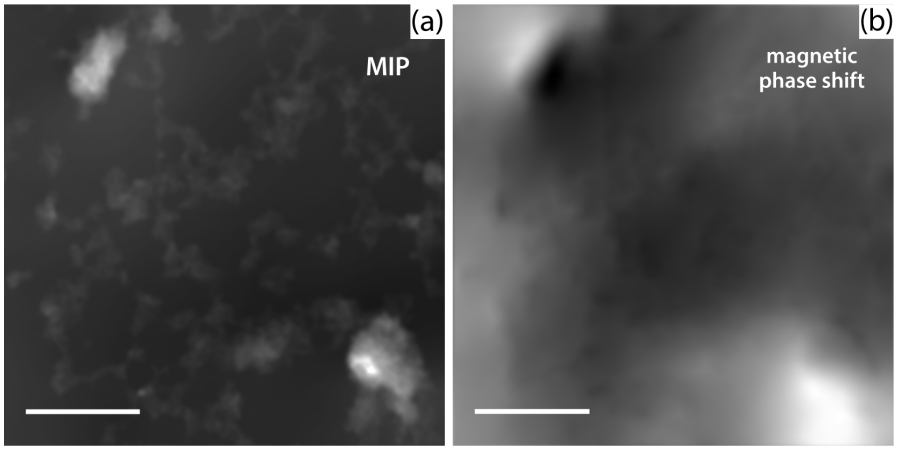

Fig. 2.8 (a) Mean inner potential and (b) magnetic phase shift obtained for the same area shown in Fig. 2.7 obtained as half of the sum and half of difference, respectively, of the phase images obtained by two focal series (the second one acquired after turning upside down the sample). The bar in each image is 0.5 µm.

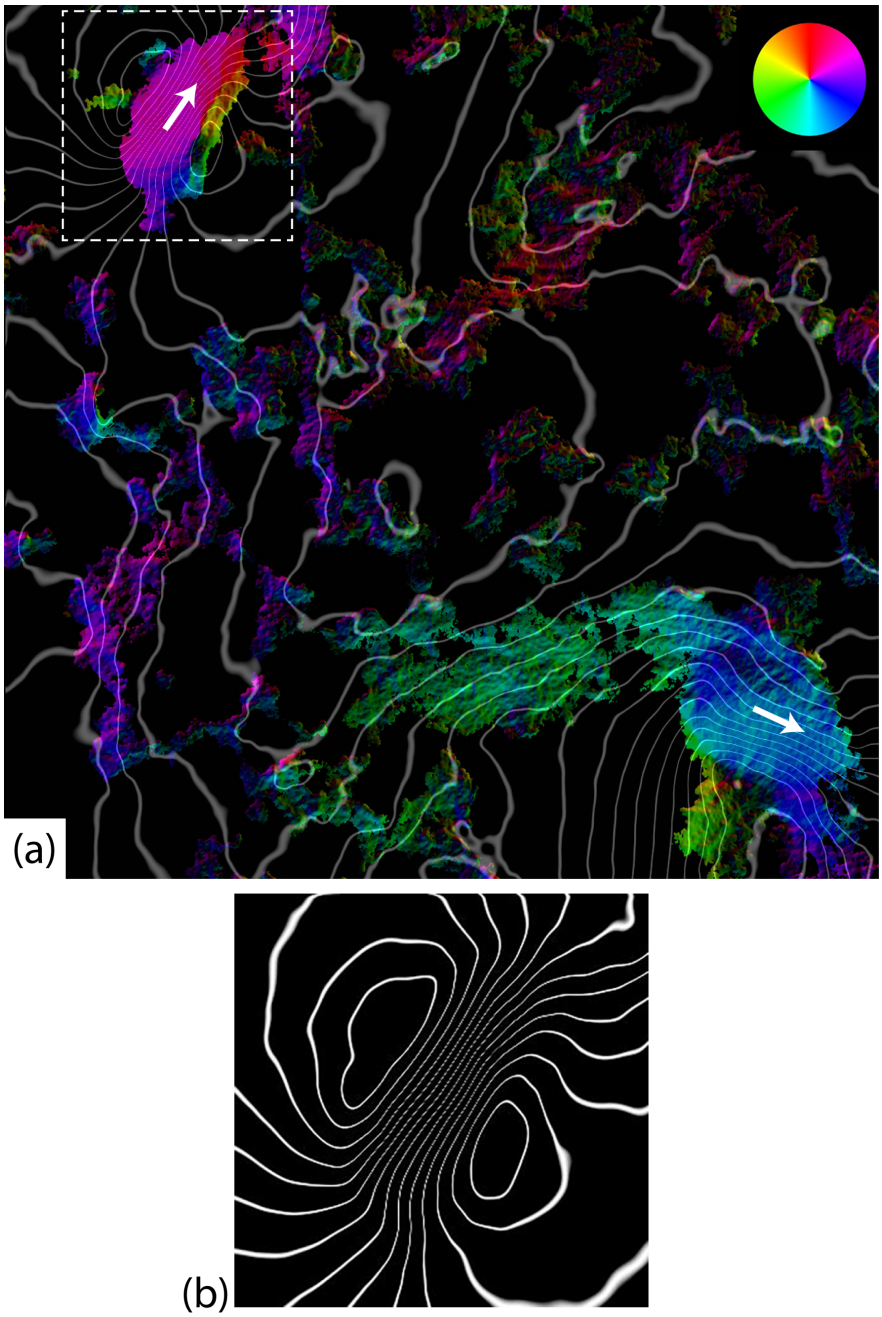

Fig. 2.9 (a) Magnetic induction colour map superimposed to the contour lines of equal phase shift, obtained amplifying 10x the phase. A white arrow indicates the direction of the magnetization in the two bigger clusters. In the top right corner the colour wheel is given. (b) Zoom of the phase contours in the region marked by the dashed line in (a).

The map clearly indicates that the clusters show a uniform magnetization, in the directions depicted by the white arrows. In the image, the magnetic induction flux lines are approximated by the phase contour lines. These lines highlight a dipolar-like behaviour of the clusters, as shown in Fig. 2.9b. Among the clusters, smaller and irregular NPs chains arise probably induced by drying the suspension in the dipolar field of the bigger clusters. The irregular chains do not show any peculiar features in the contour lines. In fact, these smaller magnetic chains do not perturb significantly the magnetic flux lines of uniformly magnetized bigger clusters; on the contrary the flux lines generated by the big clusters show a remarkable tendency to concentrate following the distribution of magnetic NPs chains among them. It is therefore possible to conclude that in the bigger clusters, which behave as magnetic dipoles, the magnetic interactions induce the moment of each nanoparticle to assume a preferential direction even if the NPs that constitute the cluster are not in the blocked momentum regime. Inside the irregular chains, instead, the interactions among NPs are less effective and do not perturb their superparamagnetic regime.

Lorentz microscopy has also been performed on the specimen of nanoparticles synthetized by thermal decomposition. As can be seen in the in-focus low magnification image reported in Fig. 2.10a, the NPs synthetized by thermal decomposition don't show any tendency to aggregate even on a large scale. The field of view of the image is 1.27 x 1.27 μm^2. A focal series with the same defocus step has been acquired (Fig. 2.10b and c). The mean inner potential and magnetic phase shift (shown in Fig. 2.11 a and b, respectively) have been retrieved using again the separation method by acquiring two focal series, one after flipping the sample. The analysis clearly points out that the highly stabilized nanoparticles are in the superparamagnetic regime and the weak dipolar interactions among NPs don't affect the magnetic behaviour of this system, since no significant features in the cosine map of the 60x amplified magnetic phase shift (Fig. 2.11c) can be related to the NPs. In fact, the magnetic flux lines visible in the map do not spatially correspond to regions of

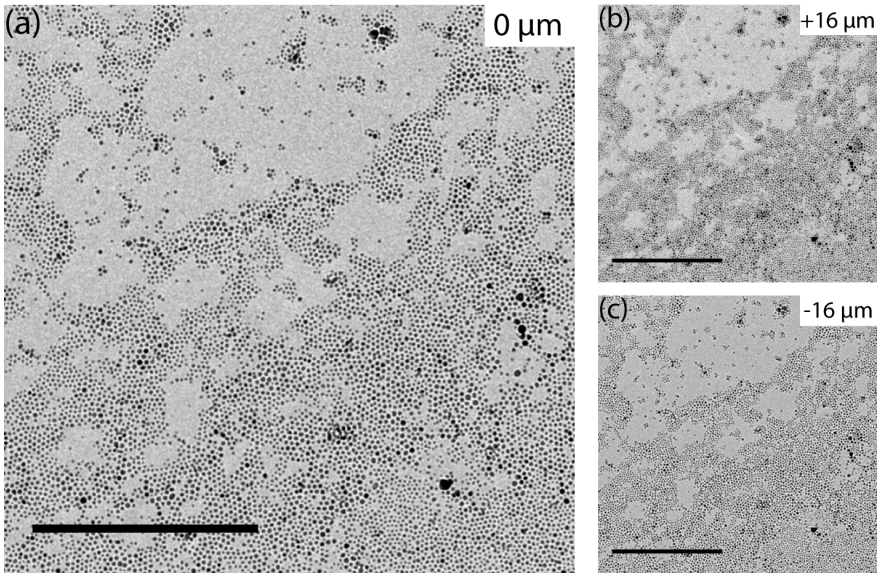

Fig. 2.10 Fresnel focal series on a portion of the sample synthetized by thermal decomposition. (a) In-focus, (b) over-focused, (c) under-focused images. The bar in each image is 0.5 µm. The defocus step for the series is 16 µm.

the sample in which NPs are present. Since a high amplification factor has been applied to the magnetic phase shift, the features shown in the image can be solely attributed to the weak and unavoidable stray fields in the microscope column. The magnetic induction colour map is not here reported since no significant features are present, as expected for a system of slightly interacting NPs in the superparamagnetic regime.

2.5.2 Correlation of magnetic hyperthermia to the NPs aggregation state

From the results described above, it is possible to assert that for the NPs obtained by thermal decomposition the organic shell hinders the establishing of inter-particle interactions, in this way allowing the magnetic moments to be free to rotate inside the crystals. It is therefore possible to conclude that the hyperthermic behaviour and the SPA value observed for this sample are mainly due to the Néel relaxation mechanism, which is the dominant one in small NPs in the superparamagnetic state.

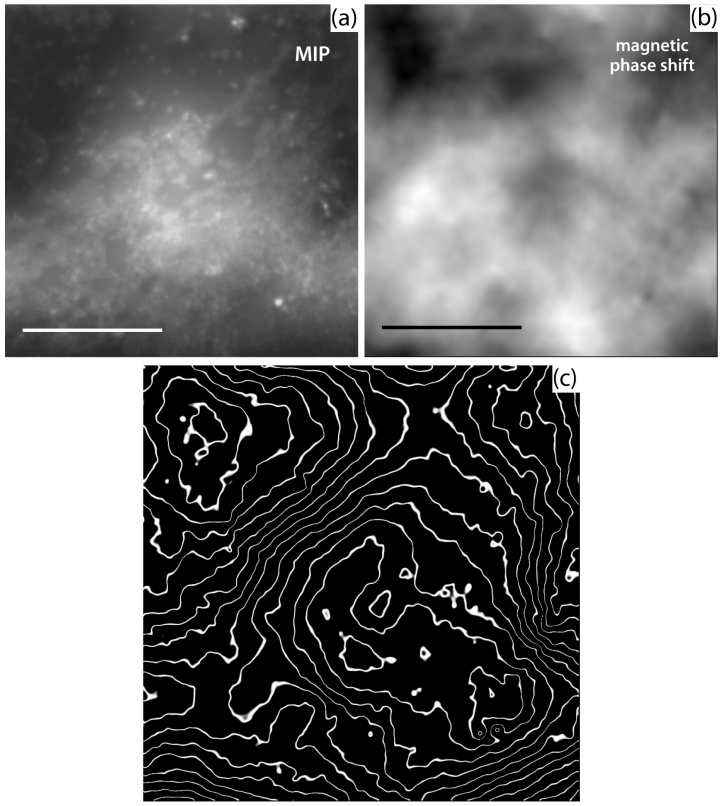

Fig. 2.11 (a) Mean inner potential and (b) magnetic phase shift obtained for the same area shown in Fig. 2.10 obtained as half of the sum and half of difference, respectively, of the phase images obtained by two focal series (being the second series acquired after turning upside down the sample). The bar in each image is 0.5 μm. (c) Magnetic induction flux lines, approximated by contour maps 60x amplified, obtained by Lorentz microscopy; the image has the same lateral size of (a) and (b).

On the contrary, the NPs obtained through co-precipitation are characterized by strong inter-particle interactions giving rise to a system constituted by big clusters, interconnected by irregular nanoparticle chains. The results obtained by Lorentz microscopy on the co-precipitated sample demonstrate that:

(i) Due to strong dipolar interactions, the big clusters show a dipole-like behaviour even if under an applied static magnetic field they don't show any hysteresis. It agreement with the results reported by F. Burrows et al. [33] is reasonably to think that the application of an AC

field (235 kHz in frequency for the measurements reported here) blocks the moments giving rise to a contribution to the SPA mainly due to hysteresis losses. The magnetic moments, that in the superparamagnetic state show a preferential orientation (as observed by Lorentz microscopy) due to the effect of strong dipolar interactions, under an external AC field are probably blocked to their common specific direction, thanks to a cooperatively alignment the NPS moments led by the interactions.

(ii) The NPs external to the clusters don't show peculiar features attributable to a dipolar-like behaviour. They show superparamagnetic properties and, thanks to the dipolar field generated by the big clusters, they organize in irregular chains. Their moments are free to rotate under an applied magnetic field, giving rise to a contribution to the SPA mainly due to Néel and Brown relaxation losses.

On the basis of the described interpretation, the SPA value for the sample synthetized by co-precipitation is consequently due to different contributions: a dominant one due to the big clusters which contribute to the SPA through the hysteresis loss mechanism and a smaller one attributed to Néel and Brownian relaxation losses, which arise as a consequence of the formation of irregular NPs chains.

The presented results demonstrate that NPs aggregates, in which different degrees of dipolar interaction are visualized by Lorentz microscopy, can behave differently and give very different contribution to the heating generation in the hyperthermia process. These effects are strongly dependent on the aggregates size and the packing of the NPs inside the clusters and can lead to erroneous interpretations about the role of magnetic dipolar interactions on magnetic hyperthermia. Lorentz microscopy represents an easy and reliable tool to investigate and understand the magnetic properties of different NPs assemblies, permitting to correlate the magnetic properties at the nanoscale to the macroscopic magnetic behaviour.

References

[1] A. Hervault and N. T. K. Thanh, *Nanoscale*, 2014, 6, 11553.

[2] H. B. Na, I. C. Song and T. Hyeon, *Adv. Mater.,* 2009, 21, 2133.

[3] F. Hu, K. W. MacRenaris, E. A. Waters, T. Liang, E. A. Schultz-Sikma, A. L. Eckermann and T. J. Meade, *J. Phys. Chem. C*, 2009, 113, 20855.

[4] O. T. Bruns, H. Ittrich, K. Peldschus, M. G. Kaul, U. I. Tromsdorf, J. Lauterwasser, M. S. Nikolic, B. Mollwitz, M. Merkel and N. C. Bigall, *Nat. Nanotechnol.*, 2009, 4, 193.

[5] N. Lee, Y. Choi, Y. Lee, M. Park, W. K. Moon, S. H. Choi and T. Hyeon, *Nano Lett.*, 2012, 12, 3127.

[6] Q. A. Pankhurst, N. K. T. Thanh, S. K. Jones and J. Dobson, J. Phys. D: Appl. Phys., 2009, 42, 224001.

[7] M. Arruebo, R. Fernández-Pacheco, M. R. Ibarra and J. Santamaría, *Nanotoday*, 2007, 2, 22.

[8] M. Liong, J. Lu, M. Kovochich, T. Xia, S. G. Ruehm, A. E. Nel, F. Tamanoi and J. I. Zink, *ACS Nano*, 2008, 2, 889.

[9] T. Todd, Z. Zhen, W. Tang, H. Chen, G. Wang, Y. J. Chuang, K. Deaton, Z. Pan, and J. Xie, *Nanoscale*, 2014, 6, 2073.

[10] R. Hergt, S. Dutz, R. Müller and M. Zeisberger, *J. Phys.: Condens. Matter.*, 2006, 18, S2919.

[11] L. Asín, M. R. Ibarra, A. Tres and G. F. Goya, *Pharmaceut. Res.*, 2012, 29, 1319.

[12] M. Suto, Y. Hirota, H. Mamiya, A. Fujita, R. Kasuya, K. Tohji and B. Jeyadevan, *J. Magn. Magn. Mater.*, 2009, 321, 1493–1496.

[13] N. K. Prasad, K. Rathinasamy, D. Panda and D. Bahadur, *J. Mater. Chem.*, 2007, 17, 5042.

[14] E. Lima Jr, E. De Biasi, M. Vasquez Mansilla, M. E. Saleta, M. Granada, H. E. Troiani, F. B. Effenberger, L. M. Rossi, H. R. Rechenberg and R. D. Zysler, *J. Phys. D.: Appl. Phys.*, 2013, 46, 045002.

[15] L.-M. Lacroix, R. Bel Malaki, J. Carrey, S. Lachaize, M. Respaud, G. F. Goya and B. Chaudret, *J. Appl. Phys.*, 2009, 105, 023911.

[16] S. Vasseur, E. Duguet, J. Portier, G. Goglio, S. Mornet, E. Hadova, K. Knızek, M. Marysko, P. Veverka and E. Pollert, *J. Magn. Magn. Mater.*, 2006, 302, 315–320.

[17] B. Mehdaoui, A. Meffre, J. Carrey, S. Lachaize, L.-M. Lacroix, M. Gougeon, B. Chaudret and M. Respaud, *Adv. Funct. Mater.*, 2011, 21, 4573–4581.

[18] J.-P. Fortin, C. Wilhelm, J. Servais, C. Ménager, J.-C. Bacri and F. Gazeau, *J. Am. Chem. Soc.*, 2007, 129 (9), 2628–2635.

[19] Y. Jing, H. Sohn, T. Kline, R. H. Victora, and J.-P. Wang, *J. Appl. Phys.*, 2009, 105, 07B305.

[20] P. Hugounenq, M. Levy, D. Alloyeau, L. Lartigue, E. Dubois, V. Cabuil, C. Ricolleau, S. Roux, C. Wilhelm, F. Gazeau and R. Bazzi, *J. Phys. Chem. C*, 2012, 116, 15702–15712.

[21] G. F. Goya, E. Lima, A. D. Arelaro, T. Torres, H. R. Rechenberg, L. Rossi, C. Marquina and M. R. Ibarra, *IEEE Trans. Magn.*, 2008, 44, 4444.

[22] P. Guardia, A. Riedinger, S. Nitti, G. Pugliese, S. Marras, A. Genovese, M. E. Materia, C. Lefevre, L. Manna and T. Pellegrino, *J. Mater. Chem. B*, 2014, 2, 4426.

[23] P. Guardia, R. Di Corato, L. Lartigue, C. Wilhelm, A. Espinosa, M. Garcia-Hernandez, F. Gazeau, L. Manna and T. Pellegrino, *ACS Nano*, 2012, 6, 3080.

[24] M. Min Y. Wu, J. Zhou, Y. Sun, Y. Zhang, and G. Ning, *J. Magn. Magn. Mater.*, 2004, 268, 33.

[25] G. F. Goya, T. S. Berquó, F.C. Fonseca and M. P. Morales, *J. Appl. Phys.*, 2003, 94, 3520.

[26] R. E. Rosensweig, *J. Magn. Magn. Mater.,* 2002, 252, 370.

[27] S. Dutz and R. Hergt, *Int. J. Hyperthermia*, 2013, 1-11.

[28] A. Urtizberea, E. Natividad, A. Arizaga, M. Castro and A. Mediano, *J. Phys. Chem. C*, 2010, 114, 4916.

[29] P. de la Presa, Y. Luengo, M. Multigner, R. Costo, M. P. Morales, G. Rivero and A. Hernando, *J. Phys. Chem. C*, 2012, 116, 25602.

[30] D. Serantes, D. Baldomir, C. Martinez-Boubeta, K. Simeonidis, M. Angelakeris, E. Natividad, M. Castro, A. Mediano, D.-X. Chen, A. Sanchez, LI. Balcells and B. Martínez, *J. Appl. Phys.*, 2010, 108, 073918.

[31] M. E. Sadat, R. Patel, S. L. Bud'ko, R. C. Ewing, J. Zhang, H. Xu, D. B. Mast and D. Shi, *Mater. Lett.*, 2014, 129, 57.

[32] C. Martinez-Boubeta, K. Simeonidis, D. Serantes, I. Conde-Leborán, I. Kazakis, G. Stefanou, L. Peña, R. Galceran, L. Balcells, C. Monty, D. Baldomir, M. Mitrakas and M. Angelakeris, *Adv. Funct. Mater.*, 2012, 22, 3737.

[33] F. Burrows, C. Parker, R. F. L. Evans, Y. Hancock, O. Hovorka and R. W. Chantrell, *J. Phys. D: Appl. Phys.*, 2010, 43, 474010.

[34] M. Jeun, S. Bae, A. Tomitaka, Y. Takemura, K. H. Park, S. H. Paek and K.-W. Chung, *Appl. Phys. Lett.*, 2009, 95, 082501.

[35] G. T. Landi, *Phys. Rev. B*, 2014, 89, 014403.

[36] R. Massart, *IEEE Trans. Magn.*, 1981, 17, 1247.

[37] S. Sun, H. Zeng, D. B. Robinson, S. Raoux, P. M. Rice, S. X. Wang and L. Guanxiong, *J. Am. Chem. Soc.*, 2004, 126, 273.

[38] C. G. Granqvist and R. A. Buhrman, *J. Appl. Phys.*, 1976, 47, 2200.

[39] C. J. Goss, *Phys. Chem. Miner.*, 1988, 16, 2, 164-171.

[40] C. Ravikumar and R. Bandyopadhyaya, *Journal Phys. Chem. C*, 2011, 115, 1380.

[41] V. Grillo, E. Rotunno, M. Campanini, M. C. Spadaro and S. D'addato, *Micros. Microanal.*, 2014, 20, 3, 2134-2135.

[42] E. Humphrey, C. Phatak, A.K. Petford-Long and M. De Graef, *Ultramicroscopy*, 2014, 139, 5.

3 The effects of epitaxial strain and film thickness on the twin variants formation in NiMnGa thin films

3.1 Introduction

Magnetic shape memory (MSM) alloys represent an interesting class of materials, very promising in novel applications regarding the transduction and actuation. In fact, their structural ability to tolerate very high strain values up to 12% and the possibility to change their shape by applying magnetic fields or by changing the temperature [1-5] make them great candidates for micro/nano-actuators [6-10], cantilevers and sensors [11-13]. Moreover, martensitic thin films are very feasible starting entities for devices fabrication and integrated-circuit design, by means of lithographic and patterning processes [14, 15].

The near-stoichiometric NiMnGa is the most investigated and promising material among the magnetic shape memory alloys. As described in Section 1.3.3, in NiMnGa thin films the martensitic phase transformation gives rise to a poly-twinned system characterized by a complex microstructure. Among all the possible twinning configurations arising from {110} twinning planes of the cubic austenitic parent phase, the epitaxial constrains due to the substrate induce the survival of only two families of twin variants, the first with 45° lamellae, the second with 90° lamellae [16-19].

The employment of a buffer-layer between the substrate and the martensitic thin film is necessary to permit the realization of free-standing structures and test-devices. In addition, some strict requirements have to be satisfied in order to obtain free-standing martensitic films that can be effectively exploited as actuators and/or cantilevers. In fact a suitable buffer layer has to provide a good matching between lattice parameters of the NiMnGa thin film and the substrate, in order to assure an epitaxial growth, and, at the same time, a selective etching process for the buffer layer should exist with the severe condition that it has not to affect the film. At this purpose, the growth of a Cr under-layer on MgO substrates is a common choice widely reported in literature [20, 21], since it provides a good matching between its lattice parameter to both the MgO and NiMnGa ones. Moreover, thanks to the existence of a selective wet etching for Cr layer [22], it can be removed obtaining free-standing martensitic thin films that can be effectively employed as actuators and/or cantilevers.

It is known from the theory of epitaxial growths that the presence of a substrate represents a strong constraint for the film growth and it is able to strongly affect the properties of the obtained film. [23, 24]. In literature many authors have reported different martensitic microstructures in differently prepared NiMnGa thin films, i.e. obtained under different growing conditions and by changing the compositions [25-28]. Since both these aspects can affect the lattice parameters of the NiMnGa films, it is therefore evident that the film/substrate mismatch is an important parameter able to play a key role in

the microstructure formation in epitaxially constrained thin films.

Another important tuneable parameter, that can significantly modify the martensitic microstructure, is the film thickness: many authors have in fact reported different martensitic microstructures at different thicknesses [18, 29-32]. To continue the analogy with the case of conventional epitaxial growths, a thickness related behaviour, ascribed to a certain strain relief mechanism, probably exists and is activated as soon as a critical thickness value is reached.

Martensitic thin films are however considerably different from conventional thin films, thanks to the complexity of their microstructure. In particular to correctly describe the martensitic system and the stable twin variants configuration generated depending on the growth parameters and thickness, both the interfacial energy at the twinning interfaces and the elastic energy for the twin variants have to be taken into account.

In the literature, a univocal model describing the effect of the strain on the martensitic microstructure has not yet been proposed. Nevertheless, an exhaustive explanation of the role of under-layer on the martensitic microstructure is still lacking. Most of the papers written on NiMnGa films grown on MgO with a Cr under-layer, in fact, assume that a thin layer of Cr does not influence the martensitic microstructure of the film at RT.

In this Chapter it will be demonstrated that for thin films the Cr under-layer has a strong influence on the martensitic microstructure generated from the parent austenitic phase, due to the different stress state of the NiMnGa cell on Cr in comparison to the case of NiMnGa cell on MgO. The effects induced by the film thickness will be also described.

In the following Section, the details about the film growth are reported (Section 3.2). In the Section 3.3, the structure and morphology of the films with thicknesses in the range 50-100 nm grown on MgO substrate will be described in order to make possible a subsequent comparison to the films with same thicknesses grown on Cr under-layer.

In Section 3.4 the experimental results obtained in the characterization of the films grown on Cr under-layer will be discussed, focusing the attention on

the correlation between structural and magnetic properties, as obtained by TEM analysis. On the basis of the presented results, a different behaviour compared to the film on MgO will be highlighted for the thin films at lower thicknesses, while a similar trend in function of thickness exists

A model for the twin variants selective formation, based on the theory of elastic domains, is described in Section 3.5. In particular, applying this model it will be shown that the different stress states for the considered films is the leading factor able to stabilize one twin variant family out of two, as well as explain the thickness dependent behaviour observed for the films grown on Cr under-layer.

It is here worth noting that, following the convention and nomenclature introduced in Section 1.3.3, the diffraction spots of the martensitic phase, as well as its crystallographic planes and directions, will be indexed within the pseudo-orthorhombic setting, which permits an easier comparison with the existing literature on thin films. Nevertheless, when necessary the corresponding indexes within the monoclinic setting will be reported, with the intent to give a detailed and clear description of the system without oversimplify its complexity.

3.2 NiMnGa films growth

All the characterized films were grown by radiofrequency sputtering apparatus with a base pressure of $3 \cdot 10^{-8}$ mbar using a single target with composition Ni(49.3)Mn(27.8)Ga(22.9) (at. %), as determined by energy dispersive X-ray spectroscopy (EDX) with an uncertainty of 0.2 at. % for each element.

NiMnGa films on the MgO(100) substrate were grown at a temperature of 693 K with an argon pressure of 1.4×10^{-2} mbar and a sputtering voltage of 1200 V; temperature was measured on the substrate surface before the growth. The resulting film composition obtained by EDXS analysis is

Ni(52.5±0.9)Mn(19.5±0.7)Ga(28.0±0.5) (at. %).

The NiMnGa films on Cr under-layer of 50 nm (layers sequence is: MgO(100)/Cr/NiMnGa) were grown at a temperature fixed at 623 K, in order to limit the intermixing between Cr and NiMnGa [21]. The resulting film composition analysed by EDXS is Ni(53.9 ± 0.8)Mn(20.2 ± 0.9)Ga(26.0 ± 0.8) (at.%).

3.3 NiMnGa films on MgO substrate

In this Section, previous results achieved in the characterization of NiMnGa films grown on MgO will be reported. In particular, the martensitic microstructures of NiMnGa films with thicknesses of 75 and 100 nm on MgO(100) substrate will be discussed in order to permit a comparison with the results obtained for the films grown on Cr under-layer, described in the following Sections.

The NiMnGa films are grown on heated substrates at a temperature where the austenitic phase is thermodynamically stable (T = 693 K). The epitaxial relation corresponding to the lowest lattice mismatch is achieved when the cubic axis of the NiMnGa austenitic cell is accommodated along the diagonal of the basal plane of the MgO cell, being the lattice mismatch between [100] NiMnGa and [110] MgO about 2.4%.

The first evidence of the strong constrains induced by the presence of a substrate can be found in NiMnGa films with low thickness. As reported by P. Ranzieri et al. [18], in fact, NiMnGa thin films with thicknesses in the range 10-40 nm display at RT an austenitic phase due to the hindering of the martensitic phase transition, whereas for the thicker films martensitic twin variants appear in the typical martensitic configuration of 45° lamellae, as shown in the cross-sectional STEM-HAADF image reported in Fig. 3.1a, and an out-of-plane component of magnetization was always observed in MFM measurements.

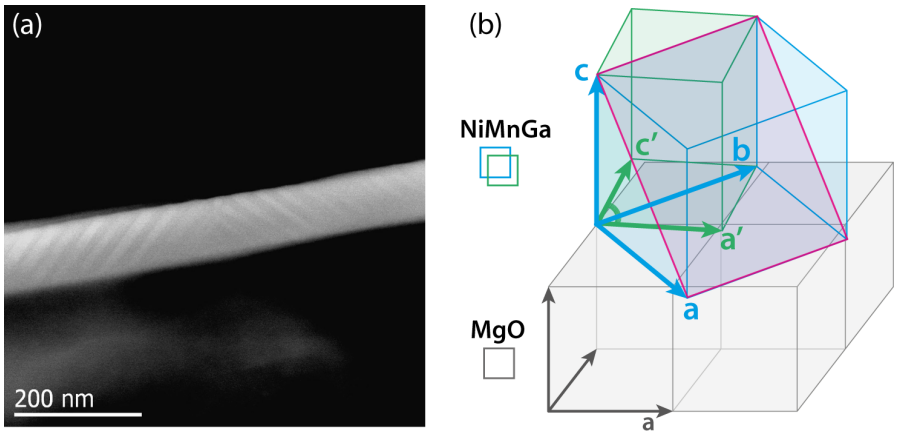

Fig. 3.1 (a) Cross-sectional STEM-HAADF image showing the morphology of the 100 nm thick film. (b) Schematic representation of the unit cell orientation for the observed twin variants: the pseudo-orthorhombic cell is sketched in blue and one of the twinning plane of the {101} family is drawn in purple. The monoclinic cell is sketched in green (in which the monoclinic angle $\beta = 93°$ is marked by the arc).

On the basis of the TEM characterization, it was possible to conclude that the visible 45° twinning planes correspond to {101} planes (indexed as {12-1} in the monoclinic setting) and induce a flipping of the c and a axes from an in-plane to an out-of-plane direction. The cell orientation related to the observed twin variants configuration is schematized in Fig. 3.1b. Among the possible {101} planes, one is drawn in purple as an example.

The temperature dependence of the austenitic lattice parameters can be inferred from the temperature evolution of the XRD pattern. In the following, in the description of temperature dependent measurements, we will refer to the austenitic diffraction spots using the letter 'A', whereas the spots relative to the martensitic phase will be marked by letter 'M'. The measurement carried out on the 75 nm thick film is reported in Fig. 3.2. The out-of-plane lattice parameters ($a_{\perp}$) of NiMnGa austenitic cell can be directly calculated from the peak positions. In particular, at 423 K the lattice parameter perpendicular to the film plane is $a_{\perp}(423\ K) = 5.783(7)$ Å. If we assume that the stress due to the epitaxial constrain produces the same distortion in the two planar edges of the

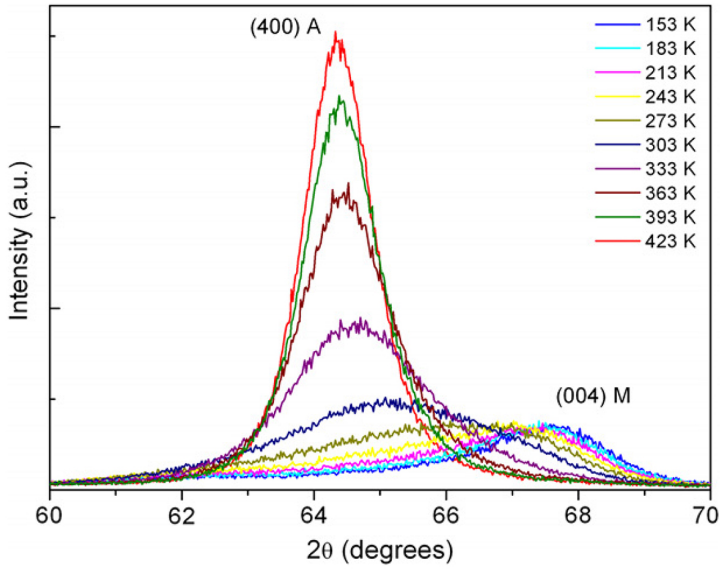

Fig 3.2 XRD patterns of the 75 nm thick film at different temperatures. The shift and the variation in the peaks intensity can be attributed to the martensitic transformation. The $(400)_A$ peak of austenite visible at high temperatures evolves into the $(004)_M$ peak of martensite at lower temperatures. (From [18]).

NiMnGa cell, the in-plane lattice parameter ($a_{//}$) can indirectly be estimated under the hypothesis that the total volume of the NiMnGa cell is not affected by the epitaxial constrain. Taking into account the linear thermal expansion of the NiMnGa austenitic phase, $\alpha_{NiMnGa} = 15x10^{-6}$ K^{-1} [33], the calculation gives: $a_{//}$ = 5.844(9) Å. It is therefore possible to conclude that the austenitic phase is subjected to a tensile strain $\varepsilon_{//}$= 0.4%. This experimental value is lower than the calculated misfit, this observation being in agreement to what reported in literature for films with higher thicknesses [34], probably thanks to the partial release of the misfit strain by the formation of misfit dislocations at the interface between film and substrate. Cooling down the temperature from 423 K to 333 K the out-of-plane lattice parameter shows a reduction in its value, with the appearance of a weak peak related to the martensitic phase and corresponding to a lattice parameter of 5.52(1) Å. This value corresponds to the martensitic c axis.

Since only this broad and low intensity peak related to the martensitic phase appear in the θ-2θ measurements, ω-scans have been performed in order to find possible martensitic orientations with scattering vectors slightly deviated with respect to the normal to the film plane. In particular, performing tilt scans along the [110] MgO and fixing the 2θ to the nominal angular values for $(400)_M$ and $(004)_M$ d-spacings of the martensitic phase (corresponding to ω = 30.7 ± 0.1 and ω = 33.9 ± 0.1), two doublets are visible (Fig. 3.3), thus demonstrating that in the thin film the unit cell can assume two different orientations, the first having the a axis and the second with the c axis perpendicular to the film plane, as found by TEM analysis. The splitting of each peak in the ω-scans, moreover, demonstrates that both the two axis are slightly tilted with respect to the normal direction of about 2.9° (for a axis) and 2.5° (c axis).

The presence of lamellae with the short pseudo-orthorhombic axis (c) normal to the film plain is in good agreement with the MFM and magnetic hysteresis loops measurements, displaying an out-of-plane component of magnetization.

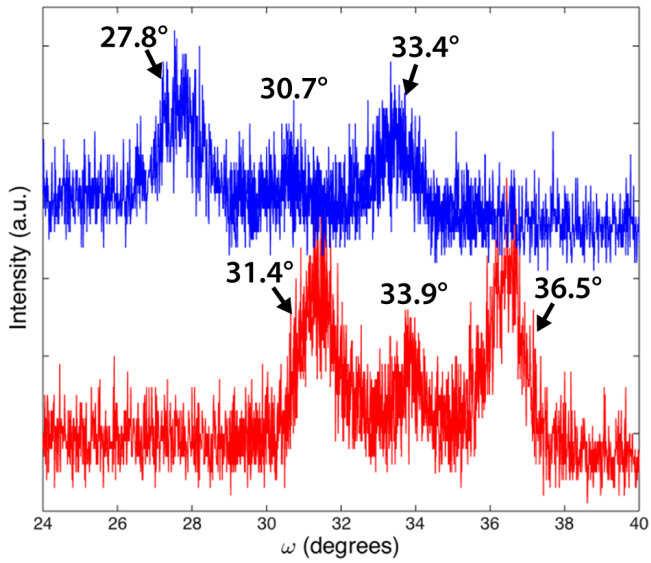

Fig 3.3 Tilt scan along the [110] MgO direction around the nominal 2θ position of $(400)_M$ and $(004)_M$ peaks (in blue and red respectively) of the martensitic cell.

3.4 The effect of Cr under-layer on twin variants formation

As already introduced in Section 3.1, the Cr is a good candidate as under-layer material for the low mismatch with both MgO and NiMnGa. In this Section the morphology and structural properties of NiMnGa films grown on Cr under-layer are discussed, highlighting the peculiar differences with the previously reported films grown directly on MgO substrate. In particular two NiMnGa films with thicknesses of 75 and 100 nm, grown onto a 50 nm thick Cr under layer, are described in details. The magnetic properties of the films are also investigated by the employment of both electron holography and magnetic characterizations.

3.4.1 NiMnGa 75 nm / Cr 50 nm/ MgO

3.4.1.1 Morphological and structural characterizations

Both HRTEM and SAED have been employed to investigate the structural properties of the Cr under-layer. The cross-sectional HRTEM image in Fig. 3.4a shows the good quality of the MgO/Cr interface, locally flat at the atomic scale. The orientation of the Cr cell respect to the MgO cell is described by the growth relationship MgO (001)[100] || Cr (001)[110], as demonstrated by the spots in the FFT of the image. In particular, the Cr grows on MgO substrate with its unit cell rotated in the plane of the film by 45° respect to the MgO one.

However, investigating the Cr/MgO interface by electron diffraction and taking into account the higher order diffraction spots, it turns out that the epitaxial Cr buffer layer is in a relaxed state. In fact, while the $(200)_{MgO}$ and $(110)_{Cr}$ spots appear superimposed (probably they are not distinguishable for the strong intensity of the MgO spot) a small but not negligible gap opens between $(400)_{MgO}$ and $(220)_{Cr}$ spots (Fig. 3.4b).

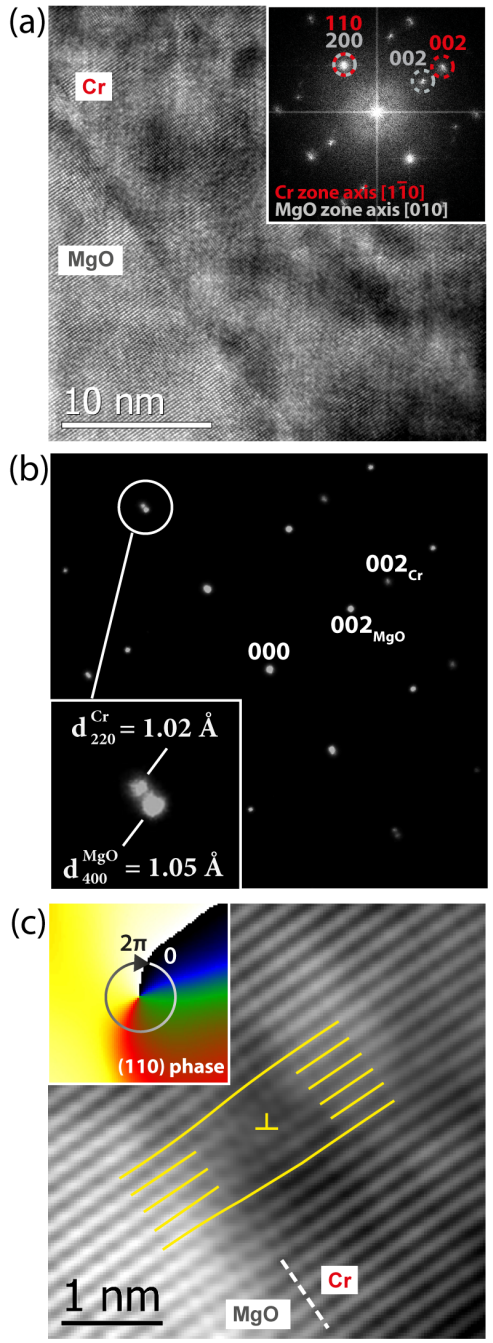

Fig 3.4 (a) HRTEM image and relative FFT (inset) of MgO/Cr interface. (b) SAED on a area across the interface. The inset shows a zoom of the second order spots. (c) Edge dislocation at the MgO/Cr interface; the extra-plane produces a discontinuity in the phase of $(110)_{Cr}$ reflection.

From the reciprocal lattice vectors lengths, the estimated values for lattice parameters of two materials are: a_{MgO} = 4.22 ± 0.08 Å and a_{Cr} = 2.88 ± 0.07 Å; these values are in perfect agreement with typical bulk parameters, thus demonstrating that the Cr under-layer is not adapted to MgO substrate.

The relief of the strain in the Cr under-layer is achieved with the formation of misfit dislocations at the MgO/Cr interface. In Fig. 3.4c, an enlargement of the MgO/Cr interface is reported: an edge dislocation is directly visible in the image and clearly highlighted by the discontinuity in the phase of the (110)Cr reflection (shown in the inset), calculated using the Geometric Phase Analysis (GPA) algorithm [35]. This result has to be taken in account in order to correctly describe the effect of under-layer on NiMnGa martensitic microstructure formation. In particular, the bulk lattice parameter of Cr will be used in the misfit strain calculations reported in the next Section.

The bright field cross-sectional TEM image of the 75 nm film reported in Fig. 3.5a demonstrates a selective twin variants formation, being the 90° twin variants the only observed in the sample in according to the configuration schematized in the figure. An HRTEM image of the interface between under-layer and NiMnGa film is shown in Fig. 3.5b. For the considered thickness, the presence of the Cr under-layer induces the martensitic pseudo-orthorhombic cell to assume an orientation with the b axis always normal to the plane of the film and the short c axis in the plane of the film along the [100] direction of the Cr, demonstrated by the (010) and (101) spots in the directions normal and parallel to the film plane respectively, as shown in the FFT of the image (inset in Fig. 3.5b). The orientation of NiMnGa cell is sketched in Fig. 3.5c, in which both the two settings are schematized: in blue the pseudo-orthorhombic setting, in green the monoclinic setting. The 90° lamellae observed in the morphological characterization are thus generated by {101} twinning planes and induce a twinning of the c and a axes in the plane of the films. The structural parameters obtained by TEM experiments are reported in Table 3.1.

Comparing this result to the one reported for the film grown on MgO, it is

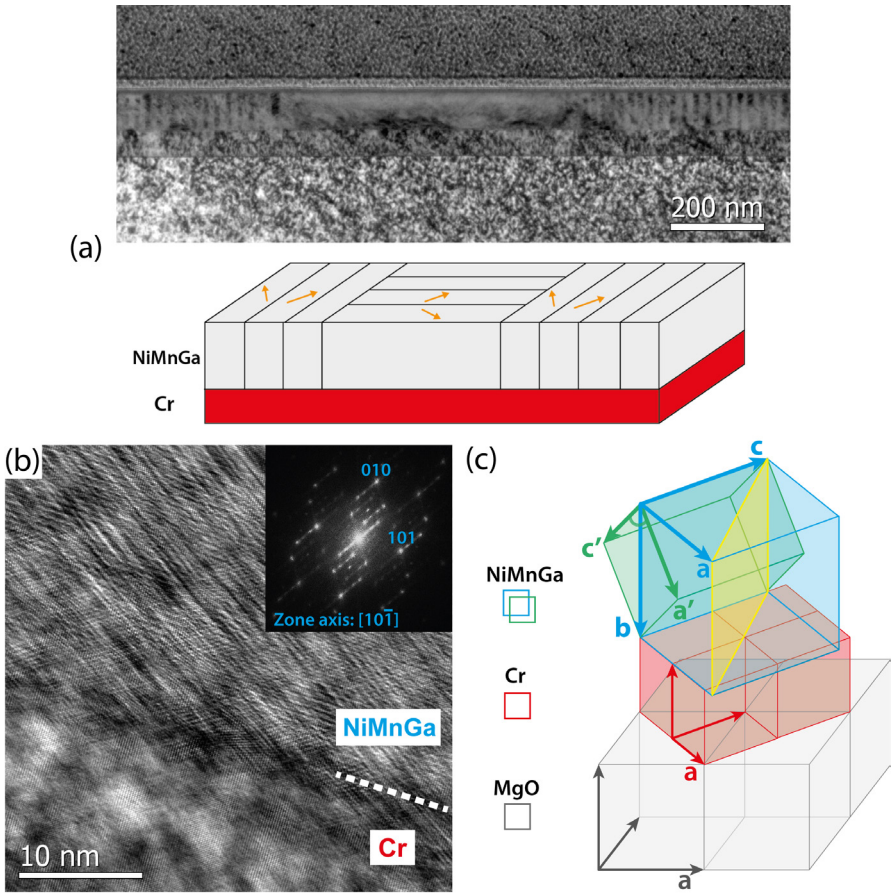

Fig 3.5 (a) Cross-sectional view of the NiMnGa film 75 nm thick and scheme of the observed microstructure. (b) HREM image showing the interface between under-layer and film; the inset shows the FFT of the image. (c) Scheme of the epitaxial relationships for the considered structure: the NiMnGa pseudo-orthorhombic cell is drawn in blue and a twinning plane of the {101} family is drawn in yellow, as example. The monoclinic cell is sketched in green (in the scheme the monoclinic angle β is marked with an arc).

System	Lattice parameters
Monoclinic (I2/m)	a′ = 4.32 Å, b′= 5.52 Å, c′ = 4.23 Å β = 92.7°
Pseudo-orthorhombic	a = 6.20 Å, b = 5.88 Å, c = 5.52 Å

Table 3.1 Lattice parameters for the 75 nm thick NiMnGa film grown on Cr under-layer, in both monoclinic and pseudo-orthorhombic settings.

worth to note that both the twinning systems observed in the martensitic thin films, displaying respectively 45° and 90° lamellae, are generated by the same twinning planes {101} in the pseudo-orthorhombic setting simply starting from a different orientation of the unit cell.

In particular, the morphological and structural characterization demonstrates that the presence of the under-layer, in the relaxed state, strongly affects the martensitic phase of the NiMnGa film of 75 nm thickness.

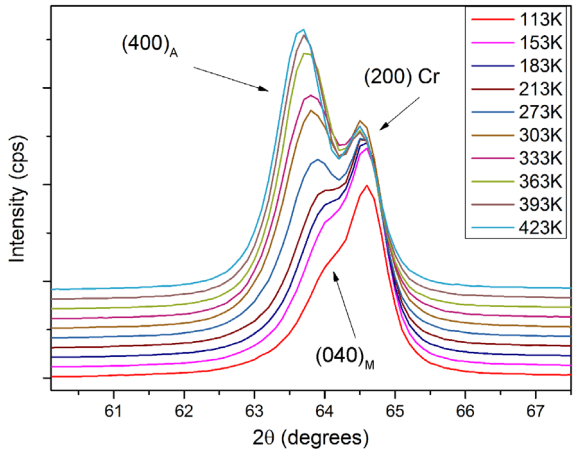

Fig 3.6 XRD patterns of the 75 nm thick film on Cr under-layer, at different temperatures. The variations of the $(400)_A$ peak position and intensity can be attributed to the martensitic transformation.

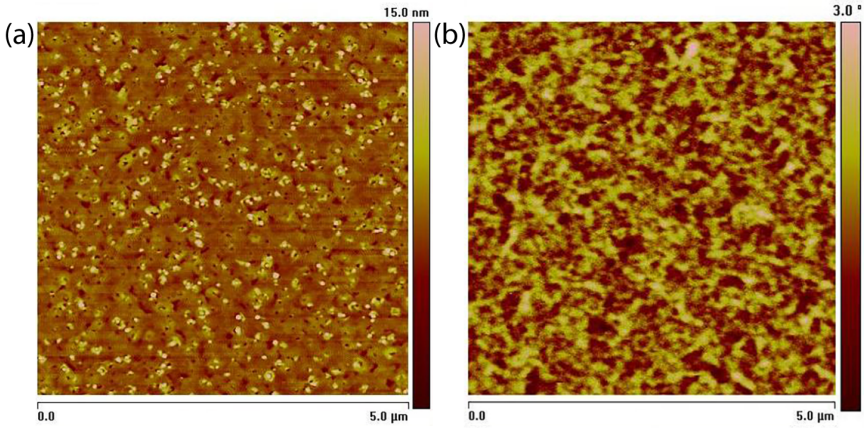

Fig 3.7 (a) AFM image of 75 nm thick film on Cr under-layer. The surface of the martensitic film is free of corrugations, indicating the absence of twin plates with 45° twinned lamellae. (b) Corresponding MFM image, demonstrating the absence of magnetic signal in the out-of-plane direction.

The temperature dependent XRD measurements reported in Fig. 3.6, carried out in the same temperature range across the transformation also investigated for the films grown on MgO (reported and discussed in Section 3.3), show that for the 75 nm thick film the $(010)_A$ peak of the austenitic phase evolves to the $(010)_M$ peak of the martensitic phase. This peak is indicative of a martensitic phase whose pseudo-orthorhombic unit cell is oriented with its b axis normal to the film plane, therefore having the short c axis in the plane of the film.

The different martensitic orientation found by TEM and XRD experiments reflects also on the surface morphology. Contrary to case of 75 nm NiMnGa films grown on MgO(100), showing the characteristic AFM surface modulation corresponding to twin variants with 45° lamellae [18], in the NiMnGa film with the same thickness grown on Cr/MgO(100) the surface modulations are totally absent, as shown in Fig. 3.7a, which is typical of 90° lamellae.

3.4.1.2 Magnetic characterizations

Beside these structural and morphological differences, it is undeniably evident that the under-layer of Cr also induces a deep change in the magnetic properties of the film, revealed by different and complementary techniques.

In Fig. 3.7b, a MFM measurement is reported, clearly indicating the absence of an out-of-plane magnetic signal. The observed behaviour, significantly different to corresponding one for the film with the same thickness but grown on MgO substrate, strongly suggests that an in-plane preferential orientation of the magnetization should exist.

In Fig. 3.8a an electron hologram acquired on the cross-sectional sample of the film is shown. Thanks to the separation method (see Section 1.4.4.1), the mean inner potential and the magnetic phase shift can be retrieved (Fig. 3.8b and c). The magnetic induction flux lines, approximated by contour lines of equal phase shift, are parallel to the film plane (Fig. 3.8d).

Also, magnetic hysteresis loops at room temperature show that the easy-magnetization direction is in the film plane (Fig. 3.9a). The saturation

magnetization is 400 kA/m, the coercivity is 10.7 kA/m when the field is applied in the film plane, 8.1 kA/m when the field is apply in the normal direction.

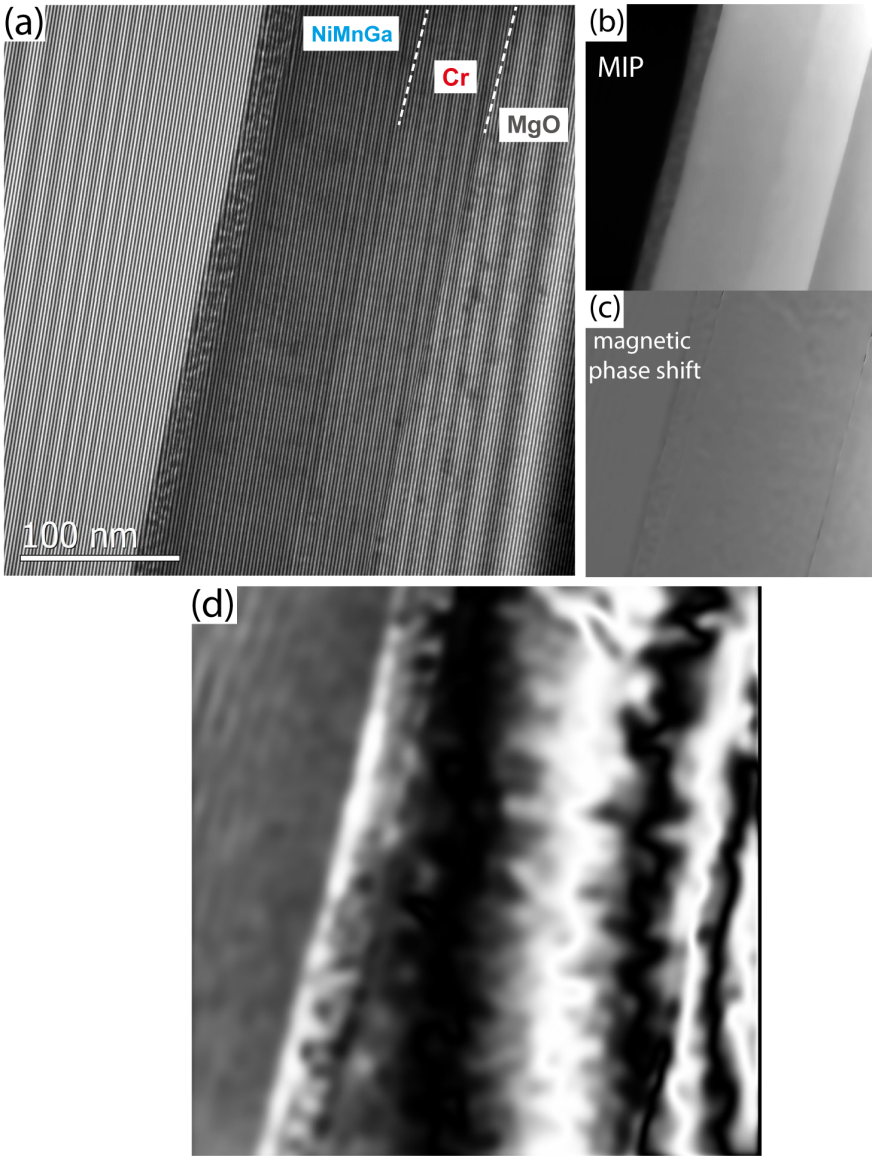

Fig 3.8 (a) Hologram of the NiMnGa 75 nm thin film on Cr/MgO in cross-sectional view. (b), (c): MIP and magnetic phase shift. (d) Cosine map of amplified (6x) phase showing magnetic induction flux lines, which are parallel to the film plane. (c)

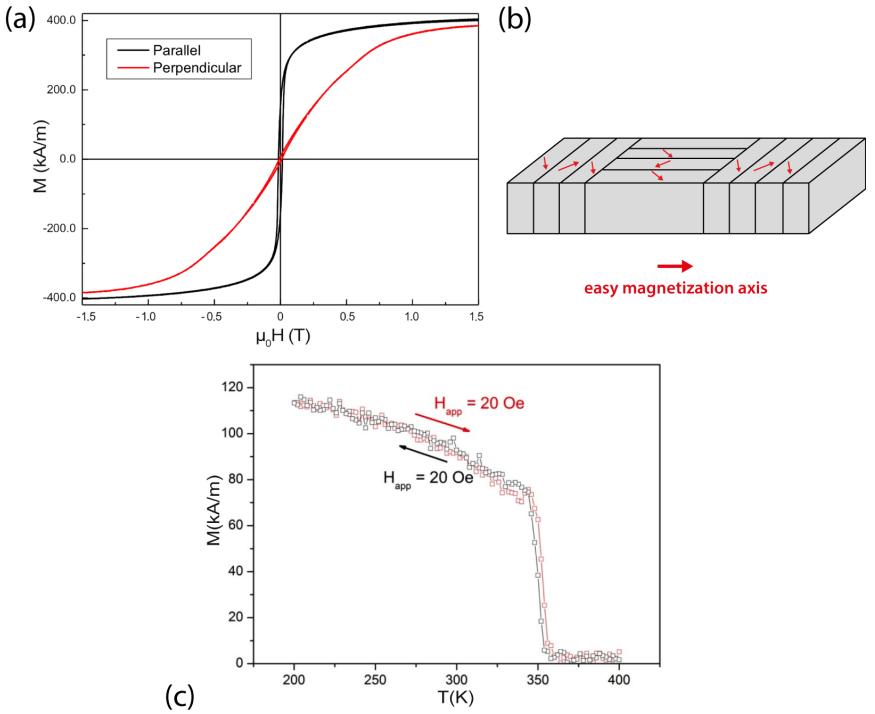

Fig 3.9 (a) RT magnetization loops measured in parallel and perpendicular configuration for the 75 nm thick NiMnGa film grown on Cr under-layer. (b) Scheme of the head-to-tail domains configuration model for the film. (c) Temperature behaviour of magnetization under an applied magnetic field (1.6 kA/m) along the (100) direction of MgO.

A model head-to-tail for the magnetic domain structures, as schematized in Fig. 3.9b, is compatible with the observed behaviour.

The effects of the temperature-induced martensitic phase transformation on the magnetization of the film were studied by applying a small magnetic field (1.6 kA/m) in the film plane. After demagnetizing the sample, the field was applied along the (100) direction of the MgO substrate and the magnetization was recorded as a function of temperature in the range 200-400 K. The magnetization trends are shown in Fig. 3.9c. In particular, decreasing the temperature from 400K, at which the austenitic phase is stable, the magnetization does not change until the value of 360 K, where a steep

increase occurs, marking the onset towards the martensitic phase. The estimated transition temperature is $T_M(\downarrow) = (352 \pm 2)$ K, obtained by calculating the maximum in the derivative curve. The transformation of the austenitic phase into the martensite is complete at 330 K and, by further decreasing temperature, magnetization slightly increases.

The reverse measurement from 200K up to 400K shows the same behaviour, with a transition temperature of $T_M(\uparrow) = (355 \pm 2)$ K. The phase transformation is therefore slightly above RT and a small hysteresis is observed.

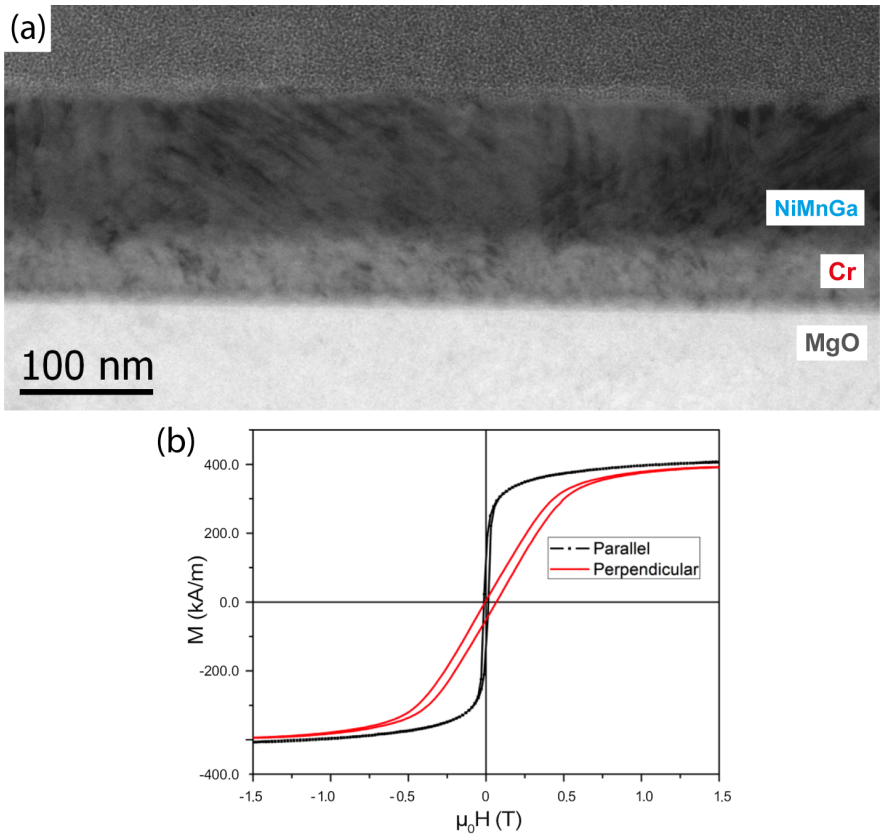

Fig 3.10 (a) Bright field cross-sectional TEM image of the 100 nm NiMnGa film on Cr under-layer: both the two family of twin variants with 45° and 90° lamellae are observed. (b) Hysteresis loops for the film in the parallel and perpendicular configurations.

3.4.2 NiMnGa 100 nm / Cr 50 nm/ MgO

The microstructure of the NiMnGa film 100 nm thick, grown on Cr under-layer, is strongly different to the one observed for the film with thickness of 75 nm previously described. In Fig. 3.10a a cross-sectional bright field TEM image of the film is shown, which displays both the two families of twin variants with 90° and 45° lamellae. The magnetic loops, reported in Fig. 3.10b for both the parallel and perpendicular configurations, is consistent with the appearance of 45° lamellae, since hysteresis is clearly visible in the direction normal to the film plane. The same morphology of the film 100 nm thick, showing the co-presence of the two twin families, is also observed for films with higher thicknesses, demonstrating that it may exist a critical thickness between 75 and 100 nm for which the second family of twin variants appears.

The results obtained for films with higher thicknesses, however, are not examined at this point; the 200 nm thick NiMnGa films on Cr under-layer will be deeply discussed in the next Chapter.

3.5 Strain-induced twin variant formation in NiMnGa thin films

In the following a model for the twin variants selective formation at low thicknesses, as well as the existence of a critical thickness for the appearance of the second family of twin variants, will be discussed starting from the theoretical model for elastic domains in solids.

3.5.1 Theoretical model

The equilibrium configuration of twin variants in a martensitic epitaxial layer is the one that minimizes the total energy of the system, given by the sum of the elastic energy and the surface energy [24]. In particular, the elastic energy contribution is due to the stress induced by the epitaxial constrains on the martensitic phase, while the surface energy is the energy term due to the

stress at the twinning planes, which are interfaces between different twin variants.

From the theoretical model of elastic domains, using a functional expression for the effective interface energy (valid if the lateral size of the twinning domains is significantly smaller than the film thickness), a thickness dependent trend of the system energy can be obtained (Fig. 3.11): for small thicknesses, a partial relief of elastic energy is obtained by the formation of one family of twin variants, whereas for higher thicknesses the system can achieve the total relief of the epitaxial strain by the formation of a poli-twinned structure in which both the twin variant families (45° and 90° lamellae) are present [24]. It follows that for very thin films with thicknesses few times larger than the lateral size of the twinned domains, true for the described cases, the elastic energy contribution is the one that governs the microstructure formation in the martensitic state, being not favourable for the system introducing new twinning interfaces at the domains boundaries between different families of twin variants. The elastic energy increases linearly with thickness and for thicknesses higher than the critical value h_C it overcomes the interface energy, which has a square root dependence on thickness [24]: new twin-boundaries are therefore created and two families of twin-variants are observed.

Experimental evidence shows that in the presence or in the absence of under-layer the NiMnGa martensitic films with thickness of 75 nm show only a twin variants family, demonstrating that up to this thickness the elastic energy contribution is the one governing the microstructure formation. Nevertheless, the peculiar configuration of twin variants observed for the specimens with Cr under-layer is totally different from the one observed for NiMnGa films of the same thicknesses on MgO. The strain analysis that is presented in the following suggests an easy guideline to comprehend why in the presence of an under-layer the free energy minimum of the martensitic phase is achieved by a different martensitic microstructure.

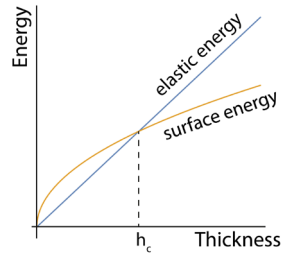

Fig 3.11 Thickness dependent trends of the elastic and surface energies. The different behaviours intersect at a critical thickness values h_C, above which the second family of twin variants appears.

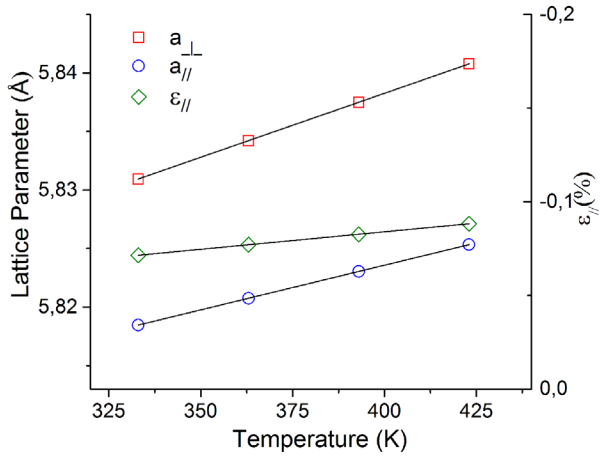

Fig 3.12 Temperature dependent behaviour of the out-of-plane (red squares) and in-plane (blue circles) lattices parameters for the austenitic phase, determined by XRD. The calculated in-plain strain is also given (green symbols).

3.5.2 Effect of strain and film thickness

In order to correctly describe the twin variant formation in the martensitic phase it is necessary to consider what happens by decreasing the temperature from the deposition temperature T_D to the martensitic phase transformation temperature T_M. Hence, in the followings we will describe the system in the austenitic phase and consider how it evolves in martensitic phase, which will be described in the pseudo-orthorhombic setting that is the closest one to the austenite.

As reported above, the NiMnGa films grown on MgO substrate show at T_D a misfit strain due to the mismatch between its lattice parameter and the MgO

one. Our experiments show that the austenitic cell is under an in-plane tensile stress, which is however smaller ($\varepsilon_{//}$ = 0.4%, as reported in Section 3.3 for the film 75 nm thick) than the calculated misfit (f = 2.4%) probably due to a partial release of the strain by the formation of misfit dislocations, as reported by Thomas et al. [34] for higher thicknesses. In the system NiMnGa/MgO the residual strain induced by the substrate leads to a selective formation of twin variants with 45° lamellae. Analysing the behaviour of the films grown on Cr under-layer, we will extend the description developing a model valid for both the cases MgO and Cr/MgO.

For the NiMnGa films grown on Cr under-layer, the experimental strain values of the austenitic cell can be calculated starting from the $(004)_A$ spot of the XRD pattern by the following method: since we need to compare the in plane austenitic parameter with the Cr one, we assume the conservation of the crystal volume and estimate the in-plane axis of austenite as the square root of the ratio between volume (taken from the bulk alloy of corresponding composition) and the out-of-plane lattice parameter obtained by X-ray measurements; a thermal expansion affecting the volume has been taken into account, assuming a coefficient of linear thermal expansion for Cr of α = 8.7×10^{-6} K^{-1} [36].

The temperature dependences of the out-of-plane and in-plane lattices parameters, as well as the in-plane strains, are reported in Fig. 3.12. The NiMnGa cell is subjected to a compressive strain $\varepsilon_{//}$ = -0.09%, which decreases linearly with the temperature. The calculated misfit of the austenitic cell on the Cr buffer layer at T_D is f = -1.2 %, meaning that the unit cell is subjected to a compressive in-plane stress. In analogy with the case previously described, also in the film grown on under-layer the observed strain value is smaller than the calculated misfit.

The different behaviour of the two described systems are schematized in Fig. 3.13a. The NiMnGa austenitic cell is under a compressive in-plane strain in films grown on Cr under-layer, whereas it is subjected to a tensile strain in films grown directly on MgO.

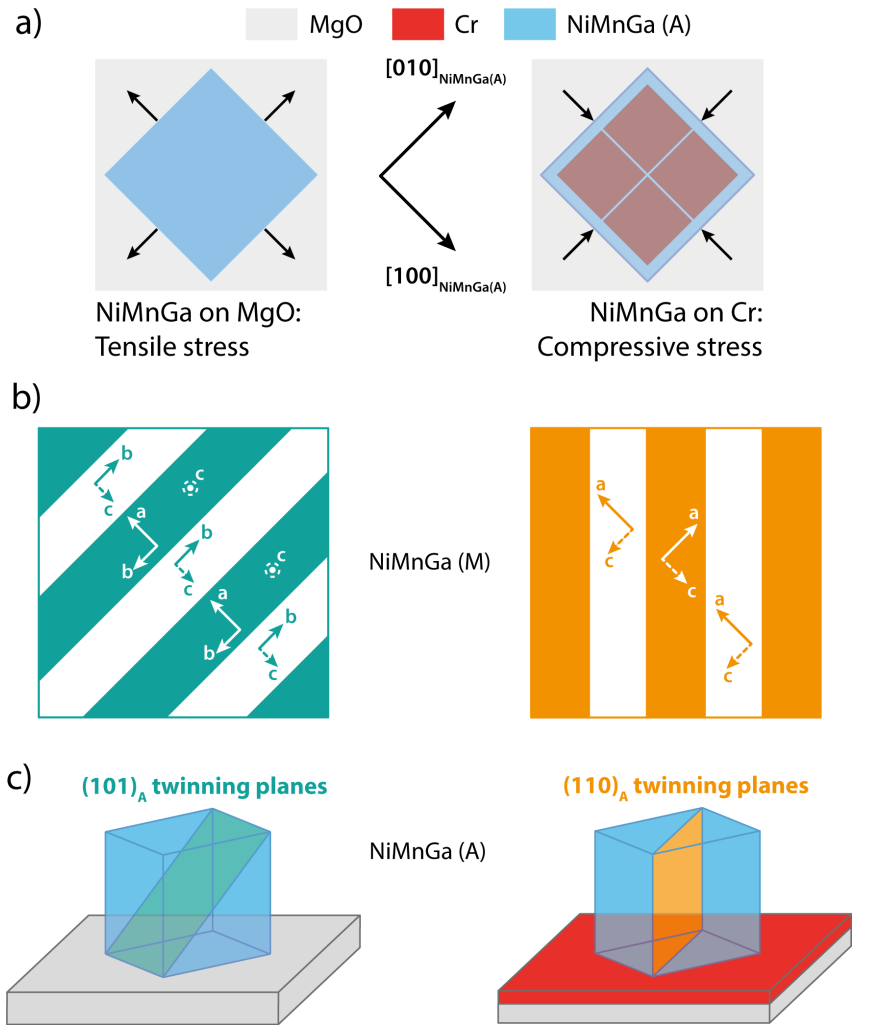

Fig. 3.13 (a) Schematic representation of the stress states of the NiMnGa austenitic cell on MgO substrate (left) and Cr under-layer (right). (b) Scheme of the two possible poli-twinned systems in the martensitic phase, generated by $(101)_A$ and $(110)_A$ twinning planes of the austenitic cell. (c) Observed twinning planes for the two different systems in the austenitic reference system.

Substrate / Configuration	MgO	Cr/MgO
$\{101\}_A$ twins (45° lamellae)	ε = +2.2%	ε = -1.1%
$\{101\}_A$ twins (90° lamellae)	ε= +2.4%	ε = -1.0%

Table 3.2 Calculated misfit strain for the possible microstructures in the NiMnGa martensitic films grown directly on MgO and with a Cr under-layer.

Starting from the RT lattice parameters of the NiMnGa martensitic cell obtained for bulk samples with similar composition [37]) it is possible to estimate the misfit strains in the martensitic films. The use of the lattice parameters of the strain-free bulk phase, apparently misleading, is necessary in order to accurately calculate the misfit strain induced by the substrate on the martensitic phase. The misfit are calculated along the in plane $[100]_A$ and $[010]_A$ directions, for the two kinds of microstructures generated by $\{110\}_A$ (producing the 45°lamellae) and $\{101\}_A$ (90°lamellae) twinning planes (schematized in Fig. 3.13b), which occur in presence or absence of Cr under-layer respectively. The calculated values are reported in Table 3.2.

On the basis of the calculated strain values, it is possible to notice how both the systems NiMnGa/MgO and NiMnGa/Cr show, for the 75 nm film thick, the twin variants system which minimize the in-plane strain. In fact, the experimentally observed microstructures (schematized in Fig. 3.13c) are 45° lamellae for the NiMnGa/MgO and 90° lamellae for NiMnGa/Cr.

Besides the agreement of the strain calculations with the observed microstructures, it is evident that for both substrates the energy difference between the two twin variants configurations is small. The small energy difference between the two possible twin variants configuration is in good agreement with the small thickness critical values at which the second family of twin variants appears (between 75 and 100 nm for the case of the NiMnGa films on Cr under-layer). However, this difference is not negligible representing about the 10% of the total strain and hence is effective in governing the microstructures of the films at thickness lower than h_C.

Although this estimation is based on the bulk lattice parameters, it points out how the system is able to switch to a different martensitic microstructure depending on the misfit strain state of the austenitic phase, choosing the microstructure that assures compatibility between the strain state of the austenitic and the martensitic phases and, at the same time, minimize the strain of the martensitic phase. The strain-induced mechanism leads, for the martensitic NiMnGa thin films in the range of thicknesses 50-75 nm, to the

formation of a martensitic microstructure with 45° lamellae for films grown on MgO and to the formation of a martensitic microstructure with 90° degrees lamellae for the films grown on Cr under-layer.

It has to be remarked that the proposed model is efficient in the description of martensitic thin films with thicknesses lower than the critical value hc. For thickness higher than h_C, the energy contribution due to the twinning interfaces has to be considered: in particular, the surface energy contribution can have a strong effect on the equilibrium twin variants configuration in the martensitic film, leading to the appearance of two families of twin variants, as observed for films with thicknesses higher than 100 nm. Furthermore, the observed results point out that for the system NiMnGa/Cr, for a thickness of the under-layer which assures that it is in the relaxed state (higher than 18 nm for Cr on MgO, from the theoretical calculation), the critical thickness for the appearance of the second family of twin variants is in the range 75-100 nm.

In conclusion, the under-layer, necessary for the purpose of devices realization, is able to strongly affect the martensitic microstructure and, providing that the effects it induces on the film are modelled, it can represent a powerful tool to selectively control the twin variants formation in martensitic thin films and so tailor the magnetic properties of the films.

References

[1] A. Sozinov, A. A. Likhachev, N. Lanska and K. Ullakko, *Appl. Phys. Lett*., 2002, 80, 1746.

[2] M. Chmielus, X. X. Zhang, C. Witherspoon, D. C. Dunand and P. Müllner, *Nat. Mater.*, 2009, 8, 863 – 866.

[3] A. Sozinov, N. Lanska, A. Soroka and W. Zou, *Appl. Phys. Lett*., 2013, 102, 021902.

[4] L. Straka, O. Heczkob and H. Hänninena, *Acta Mater.*, 2008, 56, 19, 5492–5499.

[5] H.E. Karaca, I. Karaman, B. Basaran, Y.I. Chumlyakov and H.J. Maier, *Acta Mater.*, 2006, 54, 1, 233–245.

[6] M. Kohl, A. Agarwal, V. A. Chernenko, M. Ohtsuka and K. Seemann, *Mat. Sci. Eng. A*, 2006, 438–440, 940-943.

[7] A. R. Smith, Aaron R. J. Tellinen and K. Ullakko, *Acta Mater*., 2014, 80, 373–379

[8] E. Pagounis, E., R. Chulist, M. J. Szczerba and M. Laufenberg, *Scripta Mater.*, 2014, 83, 29-32.

[9] M. Kohl, M. Schmitt, A. Backen, L. Schultz, B. Krevet and S. Fähler, *Appl. Phys. Lett*., 2014, 104, 043111.

[10] M. Schmitt, A. Backen, S. Fähler and M. Kohl, *Microelectron. Eng.*, 2012, 96, 536–539.

[11] N. Sarawate and M. Dapino, *Appl. Phys. Lett.*, 2006, 88, 121923.

[12] D Auernhammer, M Kohl, B Krevet and M Ohtsuka, *Smart Mater. Struct*., 2009, 18 104016.

[13] J. M. Stephan, E. Pagounis, M. Laufenberg, O. Paul and P. Ruther, *IEEE Sensors J*., 2011, 11, 11, 2683–2689.

[14] M. Schmitt, A. Backen, S. Fähler and M. Kohl, *Microelectron. Eng.,* 2012, 98, 0, 536-539.

[15] C. A. Jenkins, R. Ramesh, M. Huth, T. Eichhorn, P. Pörsch, H. J. Elmers and G. Jakob, *Appl. Phys. Lett*., 2008, 93, 234101.

[16] A. L. Roytburd, T. S. Kim, Q. Su, J. Slutsker and M. Wuttig, *Acta Mater*., 1998, 46, 14, 5095-5107.

[17] G. J. Mahnke, M. Seibt and S. G. Mayr, *Phys. Rev. B*, 2008, 78, 012101.

[18] P. Ranzieri, S. Fabbrici, L. Nasi, L. Righi, F. Casoli, V. A. Chernenko,E. Villa and F. Albertini, *Acta Mater.*, 2013, 61, 263–272.

[19] S. Kaufmann, R. Niemann, T. Thersleff, U. K Rößler, O. Heczko, J. Buschbeck, B. Holzapfel, L. Schultz and S. Fähler, *New J. Phys.*, 2011, 13, 053029.

[20] A. Backen, S. R. Yeduru, A. Diestel, L. Schultz, M. Kohl and S. Fähler, *Adv. Eng. Mater.*, 2012, 14, 8, 696-709.

[21] A. Backen, S. R. Yeduru, M. Kohl, S. Baunack, A. Diestel, B. Holzapfel and S. Fähler, *Acta Mater.*, 2010, 58, 9, 3415-3421.

[22] T. Eichhorn, R. Hausmanns and G. Jakob, *Acta Mater.*, 2011, 59, 5067.

[23] J. H. van der Merwe, *J. Appl. Phys.*, 1970, 41, 4725.

[24] A. L. Roitburd, *Phys. Status Solidi A*, 1976, 37, 1, 329-339.

[25] N. Lanska, O. Söderberg, A. Sozinov, Y. Ge, K. Ullakko and V. K. Lindroos, *J. Appl. Phys*., 2004, 95, 8074.

[26] C. Jiang, Y. Muhammad, L. Deng, W. Wu, and H. Xu, *Acta Mater.*, 2004, 52, 9, 2779-2785.

[27] G. H. Wu, C. H. Yu, L. Q. Meng, J. L. Chen, F. M. Yang, S. R. Qi, W. S. Zhan, Z. Wang, Y. F. Zheng and L. C. Zhao, *Appl. Phys. Lett.,* 1999, 75, 2990-2992.

[28] U. Gaitzsch, S. Roth, B. Rellinghaus and L. Schultz, *J. Magn. Magn. Mater.*, 2006, 305, 1, 275-277.

[29] A. Diestel, A. Backen, U.K. Rößler, L. Schultz and S. Fähler, *Appl. Phys. Lett.*, 2011, 99, 092512.

[30] G.J. Mahnke, M. Seibt and S. G. Mayr, *Phys. Rev. B*, 2008, 78, 012101.

[31] P. Leicht, A. Laptev, M. Fonin, Y. Luo and K. Samwer, *New. J. Phys.*, 2011, 13, 033021.

[32] Y. Luo, P. Leicht, A. Laptev, M. Fonin, U. Rüdiger, M. Laufenberg and K. Samwer, *New. J. Phys*., 2011, 13, 013042.

[33] V. A. Chernenko, M. Kohl, M. Ohtsuka, T. Takagi, V. A. L'vov and V. M. Kniazkyi, *Mater. Sci. Eng. A*, 2006, 438, 944.

[34] M. Thomas, O. Heczko, J. Buschbeck, L. Schultz, and S. Fähler, *Appl. Phys. Lett*., 2008, 92, 192515.

[35] M. J. Hÿtch, E. Snoeck and R. Kilaas, *Ultramicroscopy*, 1998, 74, 3, 131-146.

[36] N. A. Dubrovinskaia, L. S. Dubrovinsky, S. K. Saxena and B. Sundman, *Calphad*, 1997, 21, 4, 497-508.

[37] L. Righi, F. Albertini, E. Villa, A. Paoluzi, G. Calestani, V. Chernenko, S. Besseghini, C. Ritter and F. Passaretti, *Acta Mater.*, 2008, 56, 4529–4535.

4 Tuneable MIR effect in NiMnGa 200 nm thin films: a multi-scale characterization

4.1 Introduction

As already discussed, MSM alloys such NiMnGa are multifunctional materials potentially exploitable for the realization of micro-devices [1-4] thanks to their ability to reach giant strains up to 12%, one order of magnitude higher than the typical values achieved by piezoelectric or magnetostrictive materials currently employed in actuators.

The peculiar properties of magnetic shape memory alloys rely on the combination of both ferromagnetic and martensitic properties, with a strong interplay between magnetic and structural degrees of freedom. As already introduced in Section 1.3, a direct consequence of this strong correlation between structure and magnetism is that different actuation mechanisms are

possible for NiMnGa alloy.

Briefly recalling the basic concepts introduced in Section 1.3, the first kind of actuation mechanism, controlled by the temperature, is the conventional shape memory effect related to the diffusionless transformation from a high-temperature cubic austenitic phase to a low temperature martensitic phase characterized by a lower symmetry [5] and associated to the formation of martensitic variants. It is remarkable that heating the martensitic phase above the martensitic transition the cubic austenitic state is restored as well as the original shape.

In magnetic shape memory alloys a giant deformation can also be induced applying an external magnetic field by two different routes, which correspond to two additional actuation modes for martensitic materials. The first type of magnetic actuation takes advantage of the coupling between the crystal structure and the spontaneous magnetization of the material, stabilizing the phase showing the higher magnetic moment [6, 7]. The onset of a magnetically induced martensite (MIM) can be employed for actuation in a temperature range close to the temperature of the phase transition [8]. The second magnetic actuation mode observed in single crystals is based on magnetically induced reorientation of twin variants (MIR), previously discussed in Section 1.3.2.

The availability of magnetic shape memory alloys (MSM) thin films, able to reach huge strain values comparable to the ones observed in bulk crystals, would be of outstanding benefit for the effective employment of these materials as micro-actuators or, if the inverse effect is exploited, in energy harvesting and sensing. Nevertheless, the possibility of processing the thin films by lithographic procedures would open new prospects for the realization of smart and tiny machines [9], nowadays very appealing for the potential integration in actual micrometric devices [10].

However, the realization of martensitic thin films exhibiting such high strains has not been achieved up to now. Very limited MIR effects were found in thin films and a full comprehension of the mechanisms governing the MIR

effect in constrained martensitic thin films is still lacking.

In this Chapter it will be demonstrated how it is possible to control the magnetic properties of the film by controlling the microstructure, thanks to the strong correlation between the structure and magnetism exhibited by these materials. In particular, a multi-scale approach in the characterization of NiMnGa thin films will be presented in order to correlate structure, microstructure and magnetism from the macroscopic scale down to the scale length of the small twinning domains of the martensitic phase. In this approach, different TEM techniques including HRTEM, simulations and electron holography can be considered essential for the comprehension of the mechanisms involved in the twin boundaries motion in martensitic thin films.

In Section 4.2 a preliminary description of the few results reported up to now in literature concerning the realization of NiMnGa thin films displaying the MIR effect is reported.

In Section 4.3, the effects induced by the martensitic microstructure on the MIR effect are described. Thanks to a full characterization by means of SEM, AFM/MFM and magnetization measurements carried out on films showing different microstructures, it will be demonstrated that the MIR effect can be controlled and enhanced by properly tuning the film microstructure. In particular, a giant anisotropic MIR in a thin film of NiMnGa is for the first time reported. As a case study, the detailed analysis of the film showing these striking properties is given in the subsequent Sections.

An in-depth TEM characterization carried out combining different techniques, described in Section 4.4, makes possible to correlate the crystal structure to the twin variants configurations and the magnetism inside each domain of the poli-twinned martensitic phase. The employment of high-resolution imaging, as well as the comparison of the experimental images to the simulated ones, is successful in clarifying the doubts relative to the correctness of phase identification in 90° lamellae. A model based on TEM results is finally suggested to explain the anisotropic microstructure formation for the sample displaying the huge anisotropic MIR. In the last part, Section 4.5,

the realization procedure and the preliminary characterizations of a free-standing film are reported, pointing out the peculiar aspects of the martensitic structure and microstructure and investigating the martensitic phase transition in the free-standing structure.

4.2 State of the art: MIR effect in NiMnGa thin films

In the last years a great effort was devoted to the investigation of constrained epitaxial thin films grown on different substrates (i.e. MgO, STO, YSZ) [11-13] and free-standing films [13-15]. Up to now, few authors have reported about the MIR effect in constrained epitaxial thin films [16, 17].

M. Thomas et al. [11] reported a magnetic-induced twin variant reorientation in a NiMnGa film 470 nm thick grown on MgO(100) substrate. For the described film, showing a pseudo-orthorhombic structure with a strong monoclinic distortion, a reversible MIR effect was observed in the hysteresis loop measured applying an external field along the MgO (100) direction (Fig. 4.1a).

The shape of the curve, in fact, appears similar to the typical one observed for bulk martensites in which the MIR effect is displayed [11]. In particular, a step-like increase in the magnetization (Fig. 4.1b) occurs at a critical field value attributed to the twin variants reorientation process; the effect is as expected reversible, since a reduction of magnetic field is able to restore the original twin variants configuration. The fraction of the reoriented twin variants was estimated by the authors by calculating the ratio $\Delta J/J_S = 0.26$, where ΔJ represents the jump in the magnetization (obtained by the extrapolation of the magnetization curve at high fields to zero) and J_S the saturation magnetization.

The authors asserted that the reported MIR effect did not produce a radical structural change on the base of structural measurements. In Fig. 4.1c is reported the $(022)_M$ pole figure, in which a symmetric distribution of twin

variants was observed with no applied field. The structural measurements they performed demonstrate that no significant changes occur upon the application of an external field parallel to the [110]MgO (drawn as an arrow in Fig. 4.1c), as can be seen in the integrated intensity profiles reported in Fig. 4.1d. The main peaks are not affected by the applied magnetic field and the only relevant variation they observed in the measurement was a change in the background.

On the basis of these measurements, the authors proposed a model asserting that the magnetic induced reorientation of twin variants should happen only on the top of the film, being the reorientation of the twin variants near the substrate hindered by the strong epitaxial constrains. The model, in addition, states that the twin variants reorientation can occur in epitaxially constrained thin films providing that a compensation for the changes of the lateral size occurs: since the reorientation must take place without changing the film dimension, it should involve large areas of the sample to conserve the film size, by compensating the distortions on a macroscopic scale.

Beside this pioneer work about the MIR effect in constrained thin films, an exhaustive description of the reasons behind the appearance or the lack of the MIR effect in martensitic thin films is still lacking. Moreover, the new concepts recently proposed, concerning the existence of type-I and type-II twin boundaries, have to be taken into account to understand the behaviour of both constrained and free-standing thin films [17].

In the next Section the result obtained in the deposition and characterization of 200 nm thick NiMnGa films on Cr under-layer (50 nm thick) are reported. The results can be ascribed as a step forward in the understanding of the mechanisms involved in MIR effect in thin films: Moreover, the experimental results unequivocally demonstrate that the magnetic induced twin variants reorientation can be controlled, making it anisotropic or isotropic, and can be tuned, hampering or enhancing the effect, depending on the microstructure of the thin films.

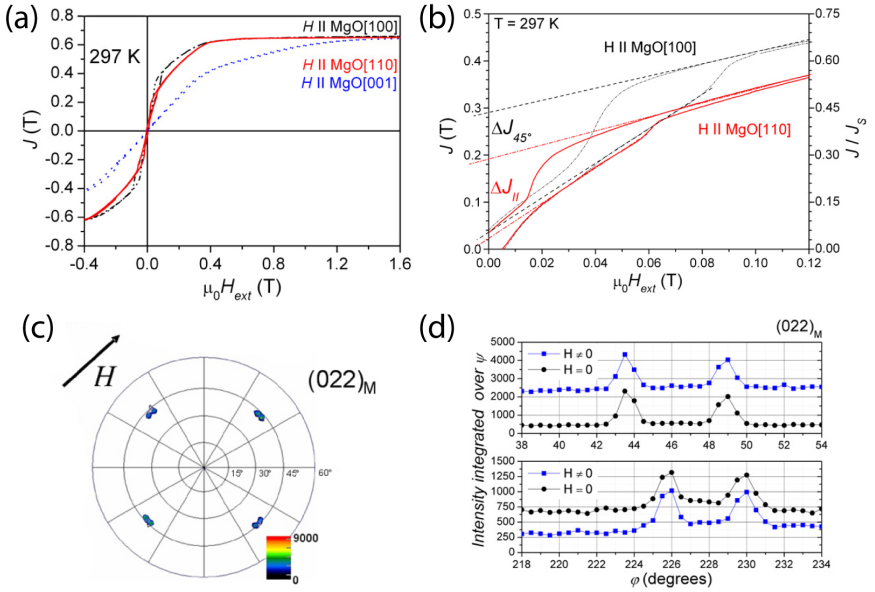

Fig. 4.1 (a) Hysteresis curves for the martensitic NiMnGa film at RT with the applied field along two in-plane directions, $[100]_{MgO}$ and $[110]_{MgO}$, and in the perpendicular direction. (b) 1st quadrant of the magnetization curve for the two in-plane directions. (c) Pole figure of the $(022)_M$ diffraction spot of the film at 300 K. (d) Integrated intensity of the $(022)_M$ pole along the applied magnetic field, in both parallel (top) and antiparallel (bottom) directions. The profiles obtained in the absence of the external field are also given. (From [11])

4.3 MIR effect: correlation between morphology, microstructure and magnetism

The described samples consist in 200 nm thick NiMnGa films with the composition Ni(53.7±0.7)Mn(21.8±0.8)Ga(24.5±0.8), as verified by EDXS analysis, grown on MgO(100) substrate on the top of a Cr under-layer 50 nm thick. The epitaxial relationships have been verified and are the same observed for the thinner films reported in the previous Chapter. In particular, at the deposition temperature (where the austenite is stable), they can be summarized as:

- Cr (001)[110] || MgO (001)[100];
- NiMnGa (001)[100] // Cr (001)[100]// MgO (001)[110] and NiMnGa (001)[010] // Cr (001)[010] // MgO (001)[-110].

The martensitic transformation, occurring for these films slightly above RT (≈ 325 K), transforms the cubic austenitic phase, stable at the deposition temperature, into the monoclinic martensitic phase. The crystal structure and the lattice parameters will be given in the next Section, in which a complete TEM characterization is presented.

Changing the deposition parameters it is possible to induce a preferential orientation in the martensitic microstructure. In particular, by applying different stresses on the substrate, depending on the way in which they are mounted on the sputtering sample holder, different distributions and orientations of twin variants can be induced due to the variation of the stress on the NiMnGa cell. In particular, three samples with different microstructure will be described. The samples are named A, B and C.

Large-scale SEM images of the three different NiMnGa thin films are reported in Fig. 4.2a, c and e respectively, recorded using a back-scattered electron detector (BSED). In all the images the [100] direction of MgO corresponds to the vertical edge of the image.

The first film, the sample A (Fig. 2a), displays by two different martensitic plates mixed together in the entire area, showing areas with bright and dark contrasts. The plates, which look brighter in the image, have approximately a rectangular shape with a high aspect ratio, with the longer edge along the [100] direction of the MgO. As can be seen in the image at higher magnification in Fig. 4.2b, these twin plates show an internally twinned structure with lamellae of 20 nm in width, running along the [100] direction of the MgO.

On the base of the TEM analyses, previously reported in Chapter 3, in these plates we expect a twinned martensitic microstructure characterized by 90° lamellae separated by twinning planes perpendicular to the film plane. On the contrary, the zones with a dark contrast exhibit a twinned microstructure with lamellae that intersect the surface of the film forming lines at 45° with respect to the [100] direction of MgO; for these regions, we can predict a microstructure with 45° lamellae.

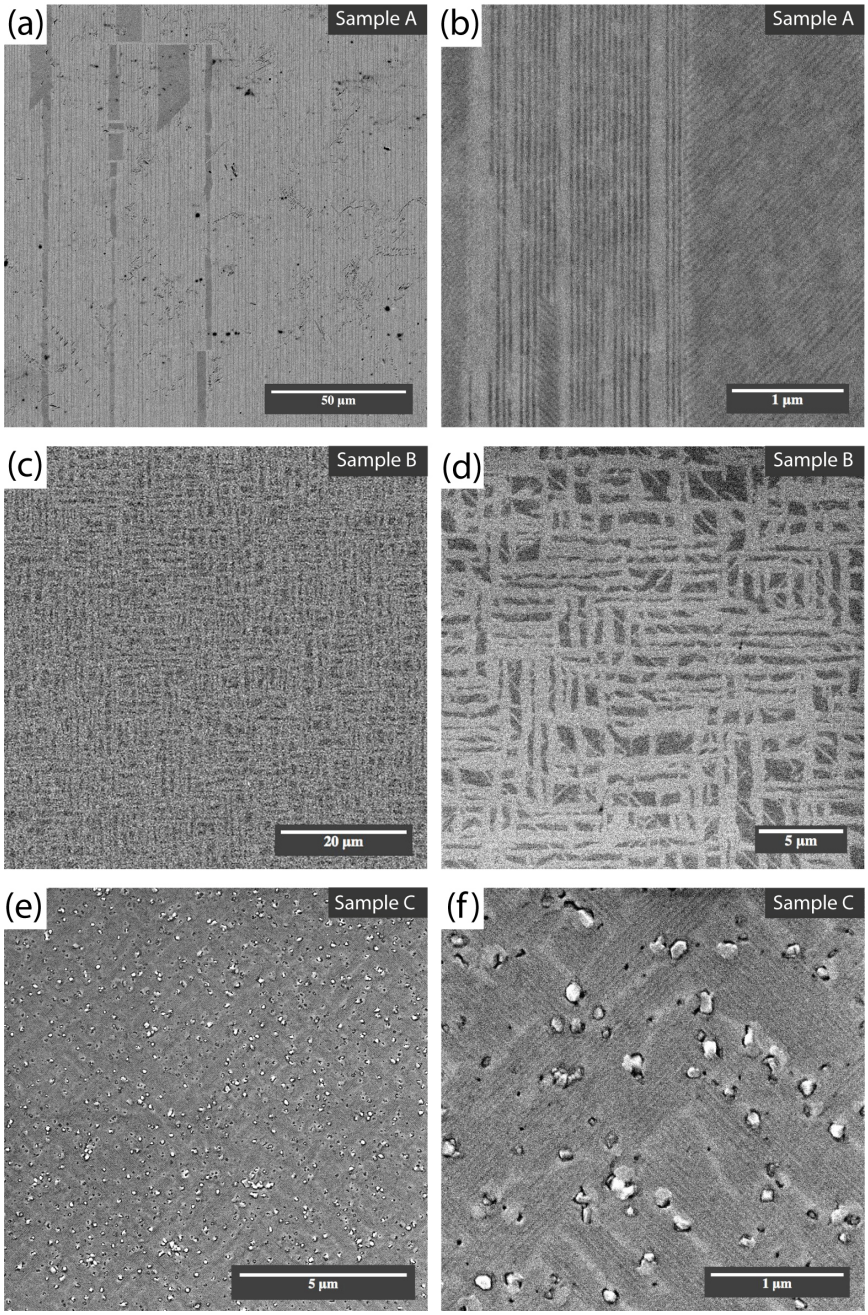

Fig. 4.2 (a), (c) and (e): Large-scale SEM-BSED images of three different NiMnGa thin films, respectively named A, B and C. The $[100]_{MgO}$ direction corresponds to the vertical edge of each image. (b), (d) and (f): SEM-BSED images at higher magnifications of the A,B and C films showing the twinned martensitic microstructure at a finer scale.

The most noteworthy aspect of the film morphology is that a strong preferential orientation of the martensitic microstructure exists: the 90° lamellae, in the brighter area of the image, run parallel to only one edge of the substrate, corresponding to the [100] direction of MgO, while the same lamellae are not displayed along the equivalent [010] direction of MgO.

The second film, the sample B (Fig. 4.2c), has a microstructure very similar to the sample A, showing two different martensitic plates appearing as bright and dark areas in the image. Inside each martensitic plate the sample has a microstructure internally twinned in the same way as was for the sample A. However, two remarkable differences between B and A appear evident: first, the B sample shows an homogeneous distribution of the different twin plates (in particular, no preferential orientations are observed for plates containing 90° lamellae, which run parallel to both the [100] and [010] directions of the substrate); moreover, the two families of twin variants are finely mixed together down to a scale length of few microns, as demonstrated by the SEM image at higher magnification (Fig. 4.2d).

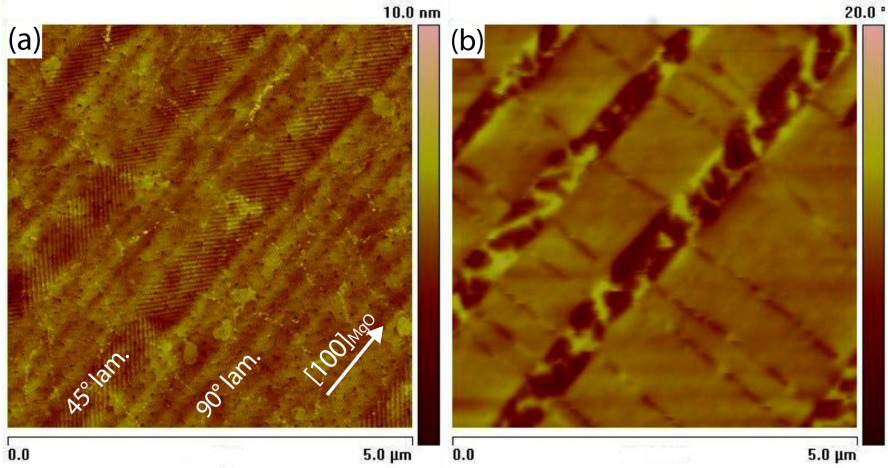

Fig. 4.3 (a) AFM image of the sample A. The [100] of MgO is oriented along the diagonal of the image. 45° lamellae are easily recognized thanks to their typical surface modulation. (b) MFM image of the same area of the sample, showing a strong out-of-plane magnetic signal from the martensitic plates with 45° lamellae.

The third film, sample C (shown in Fig. 4.2e), differs significantly from the A and B samples since only the family of twin plates displaying 45° lamellae is present. The lamellae are oriented in such a way that they emerge on the film surface forming line parallel to both the in plane diagonal of the MgO cell. Beside this isotropic orientation, a finely mixing of them occurs at a short length scale, as visible in the image at higher magnification shown in Fig. 4.2f.

The surface morphology and the magnetic properties of the films have been studied by AFM and MFM, with the aim to correlate the microstructure to the magnetism of the twin plates at the micrometric scale. The results obtained on the sample A are reported as an example; they can be considered significant also for samples B and C which display the same kinds of twin plates, solely characterized by a different organization and distribution of the twin plates and variants.

As expected, in the AFM investigation (Fig. 4.3a) the typical contrast due to surface corrugations [18] is observed in the regions containing 45°lamellae, while the plates containing 90° lamellae appear flat at the nanometre scale. In the MFM image (Fig. 4.3b), which is a map of the out-of-plane magnetization, a strong magnetic signal can only be revealed in correspondence of twin plates with 45° lamellae. No significant magnetic contrast is visible in twin plates with 90° lamellae; in these regions, the only detectable features are narrow stripes orthogonal to the longest direction of the twin plates. These features can be attributed to domain walls between regions in which the magnetization is oriented in the plane of the film along different directions.

In Fig. 4.4 the magnetization curves for the three described samples are shown. The sample A shows a peculiar anisotropic metamagnetic behaviour (Fig. 4.4a): in fact, by applying a field along the [100] direction of the MgO a huge jump in the magnetization, outreaching 55% of the saturation value, occurs. In analogy with the already reported case of MIR effect in NiMnGa thin films, the shape of the magnetization curve and the reversibility of the effect can be ascribed to the twin variants reorientation process, but the magnetization variation here observed is unprecedented. The twin boundary

motion occurs between two field values from which we can evaluate the average field for the MIR process, which is H_{MIR} = 78 mT. The low applied magnetic field needed to reorient the twin variants is a direct demonstration of the existence of twin boundaries with high mobility and the entity of the magnetization jumps is a proof of the large scale on which the phenomenon happens. It is here worth to remark that the described behaviour is displayed only in one direction, the one which correspond to the preferential orientation of the 90° lamellae (as previously observed in the morphology description), whereas by applying the field along other high-symmetry in-plane directions (i.e. [110], [010]) of the MgO substrate a conventional easy magnetization curve is observed (Fig. 4a, blue and black curves).

The hysteresis loops for the sample B, reported in Fig. 4.4b, show a MIR effect in both the two directions [100] and [010] of the MgO substrate. The magnetization jumps are equivalent for the two directions and their absolute value (≈ 25 - 30%) is lower than the one achieved in the sample A. The hysteresis loops for the sample C (Fig. 4.4c), instead, do not show any difference between the two directions and, moreover, no evidence of MIR effect is observed.

These experimental results demonstrate the important role of the microstructure in the magnetization processes of NiMnGa thin films and that it is possible to achieve a substantial enhancement of the MIR effect by controlling the film microstructure.

In the following Section an in-depth TEM analysis on the sample A is presented: by combining different techniques, a full characterization of the structural and magnetic properties of the materials is achieved. In the analysis a direct correlation between the properties at the nanoscale and the microscopic morphology is always afforded.

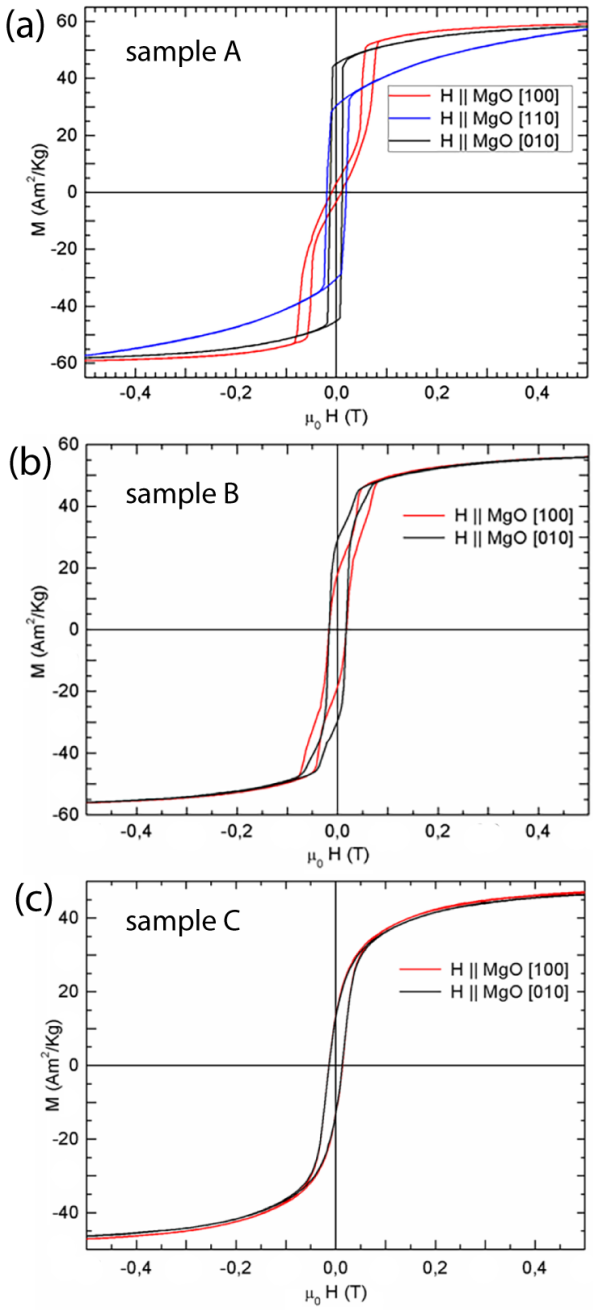

Fig. 4.4 (a), (b) and (c): magnetization curves along different in-plane directions (different colours) or the A, B and C samples respectively. The A sample show a huge anisotropic MIR effect along the [100]MgO direction, whereas the B sample show a smaller MIR effect in both in-plane directions given by [100] and [010] MgO. No MIR is observed in the magnetic measurements performed on the C sample.

4.4 Microstructure-induced giant anisotropic MIR: an in-depth TEM analysis

The TEM characterization is organized in the following way: first of all, the structural properties of the films are discussed, focusing the attention to some open problems concerning martensitic thin films, which are clarified by a deep structural/crystallographic investigation; in the second part a magnetic characterization at the nanoscale is provided by electron holography, keeping in mind the strong relationship between structure and magnetism which governs the behaviour of martensitic shape memory alloys.

4.4.1 Structural properties: from the unit cell to the microstructure

4.4.1.1 Crystal structure and twin variants

The morphology and the structural properties of sample A have been investigated by the use of transmission electron microscopy in both cross-sectional/planar views.

From the STEM images acquired using the HAADF detector, shown in Fig. 4.5, it is easy to recognize in both cross-sectional (Fig. 4.5a) and planar (Fig. 4.5b) views the two regions characterized by bright and dark contrast in the SEM-BSED images (shown in the previous Section). The set of axes for the two TEM specimens, with respect to the principal directions of the MgO substrate, is given in Fig. 4.5c. As can be noted from the STEM-HAADF images, the anisotropic microstructure is not lost in the TEM prepared samples since the preferential orientation of the bright areas is conserved, as can be seen in the planar specimen.

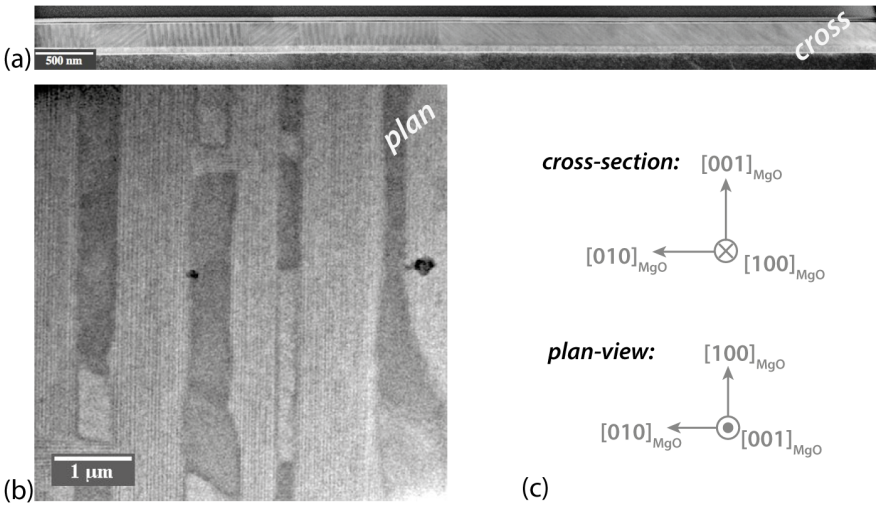

Fig. 4.5 Low magnification STEM-HAADF images of the prepared TEM specimens on sample A: (a) cross-sectional view, (b) planar view. The bright and dark areas observed in SEM images reported in Fig. 4.2 can be recognized. (c) Set of axes, with respect to the principal directions of the MgO substrate, for the cross-sectional and planar TEM specimens.

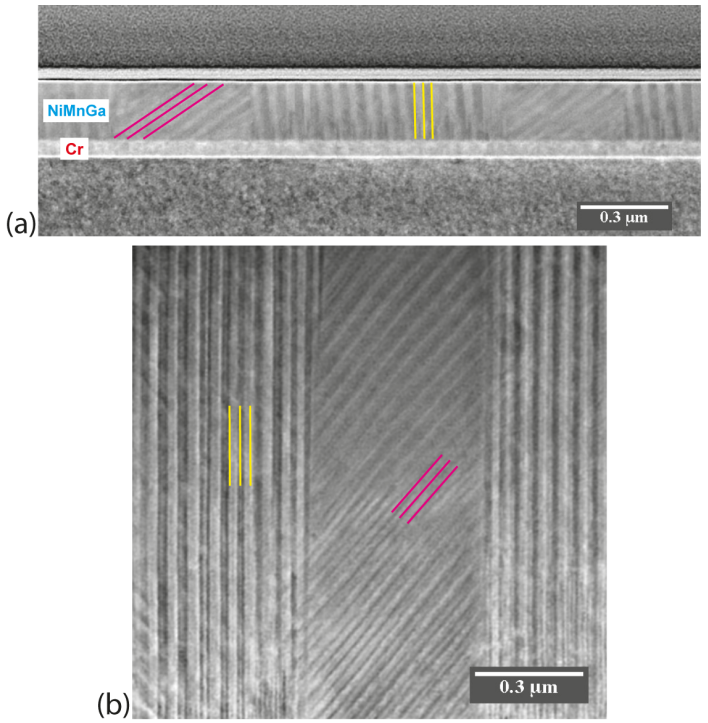

Fig. 4.6 STEM-HAADF images of the (a) cross sectional and (b) planar specimens. The twin variants families inside each martensitic plate are visible. The twinning planes of 90° lamellae are drawn in yellow, twinning plane between 45° lamellae in purple.

Analysing the TEM specimens at a higher magnification (Fig. 4.6: (a) cross-section, (b) planar view), it is evident that also the correspondence between the twin plates with different contrast and the fine twinning of the microstructure observed by SEM analysis is conserved. In particular, the same colour notation introduced in the previous Chapter to indicate twin boundaries between different twin variants is used: 90° lamellae are generated by the twinning planes perpendicular to the plane of the film, schematically represented by yellow lines, while 45° lamellae are generated by tilted twinning planes, drawn in purple.

The 90° lamellae are preferentially oriented along the [100] direction of MgO, the direction in which the anisotropic MIR effect is observed. The reported images demonstrate that the TEM samples preparation, by means of focus ion beam (FIB) for the cross-sectional specimen or by conventional preparation (dimple grinder and ion milling) in the case of the planar one, does not alter the martensitic microstructure and the relative abundance of different martensitic plates and families of twin variants.

Since this 200 nm thick film is deposited above an under-layer of Cr 50 nm thick using a single target with the same composition to the one used to deposit the films with lower thicknesses described in the previous Chapter and setting the same growth parameters, it is not surprising that both the twin variants families coexist in the martensitic microstructure. On the basis of the thickness-dependent model for the twin variants formation developed in Chapter 3, in fact, the two twin variants families are expected for thicknesses higher than 100 nm.

Following the methodological analysis previously proposed, the employment of electron diffraction can be very useful to understand the epitaxial relationships between the different layers, whereas HRTEM performed on the two different regions (containing respectively 45° and 90° lamellae) of the NiMnGa thin film allows investigating the relationship between the morphology of the twinned lamellae and the crystal cell orientations, providing a clear view on the twinning involved.

System	Lattice parameters
Monoclinic (I2/m)	a′ = 4.32 Å, b′= 5.52 Å, c′ = 4.23 Å β = 93°
Pseudo-orthorhombic	a = 6.20 Å, b = 5.89 Å, c = 5.52 Å

Table 4.1 Lattice parameters for the 200 nm thick NiMnGa films grown on Cr under-layer. The lattice parameters are given for both monoclinic and pseudo-orthorhombic settings.

As already demonstrated in the previous Chapter and here not reported, the Cr buffer layer grows with the cubic [110] direction parallel to the cubic [100] direction of the MgO substrate; for the considered thickness, the tensile strain in Cr layer is released thanks to the formation of misfit dislocations at the interface wit the substrate. The NiMnGa thin film grows in the austenitic phase with the [100] axis parallel to the [110] direction of the MgO. At room temperature, the NiMnGa thin film shows a martensitic structure characterized by lamellae with a width of about 20 nm and a length, in the longest directions, up to tens of microns.

The crystal structure of the martensitic phase can be properly described within the monoclinic system. In particular, HRTEM analysis points out a 7M modulated structure with lattice parameters a′= 4.23, c′ = 4.32 Å, b′=5.52 Å and a monoclinic angle β = 93°, the b′ axis in the monoclinic setting corresponding to the short pseudo-orthorhombic c axis following the established convention. The modulation runs along the c′ axis, which corresponds to the [110] direction (basal plane diagonal) in the pseudo-orthorhombic setting. The details of the crystal structure in both monoclinic and pseudo-orthorhombic settings are given in Table 4.1. It is worth to note that the crystal structure observed in the films is closely comparable to the monoclinic one reported for 7M martensitic bulk samples with similar compositions [19].

The effect of the twinning planes in martensitic plates characterized by 90° lamellae is clearly visible in HRTEM image of the planar specimen (Fig. 4.7a). In

the FFT of the HRTEM image, shown in Fig. 4.7b, the reciprocal lattices cells (in the pseudo-orthorhombic setting) of the two twinned crystals are drawn with continuous and dashed lines respectively. The two configurations of the unit cells in the twinned lamellae are schematized in Fig. 4.7c.

The effect of the twinning planes in the second family of martensitic plates, showing 45° lamellae, is intrinsically difficult to observe since the twinning planes are rotated in the plane of the film by 45° with respect to the [100] direction of MgO and at same time they are tilted 45° from the normal to the film plane. Hence, neither in planar or in cross-sectional views, we are able to eliminate the superimposition of the twinned crystals. Their effect on the martensitic cell can anyway be understood in the HRTEM images of the cross-sectional specimen. The image reported in Fig. 4.8a, in fact, shows the different orientations of two adjacent twinned lamellae indicated by the presence of two different projection of the 7M modulation in the FFT of the image (Fig. 4.8b): the structural modulation runs along the [110] direction in the pseudo-orthorhombic setting and thanks to the twin it can occur in the plane of the film, if the unit cell is oriented with the short c axis (easy magnetization axis) perpendicular to the film plane, or at 45° with respect to the plane of the film, if the unit cell is oriented with the short c axis lying in the plane of the film, parallel to the [110] direction of the MgO substrate.

The two described configurations, as well as the geometrical considerations used to demonstrate the effect of the twins in plates containing 45° lamellae, can be more easily understand if the scheme reported in Fig. 4.8c is considered. In both the schemes shown in Fig. 4.7c and Fig. 4.8c the twinning planes are represented in the same colours used in Fig. 4.6a and 4.6b.

Since the giant anisotropic MIR effect for the A sample is observed if the external magnetic field is applied along the preferential orientation of the 90° lamellae and taking into account that the C sample, in which only 45° lamellae are observed, does not show any evidence of twin variants reorientation under an applied field, it can be deduced that the martensitic plates containing 90° lamellae play a pivotal role in the metamagnetic transition.

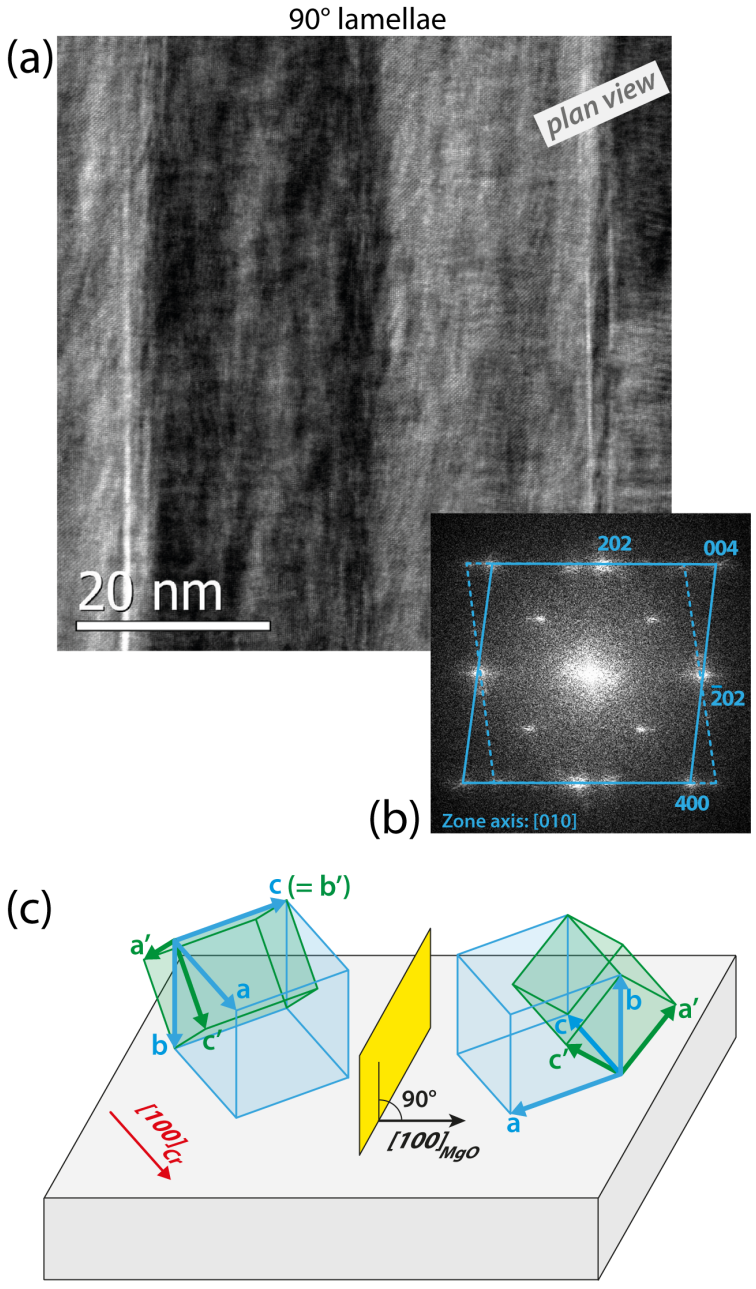

Fig. 4.7 (a) HRTEM image of twin variants with 90° lamellae. (b) FFT of the image; the two twinned reciprocal lattices cells are sketched. (c) Scheme of the twinning planes involved and the relative martensitic cell orientations: in green the cells in the monoclinic setting, in blue the cells in the pseudo-orthorhombic setting.

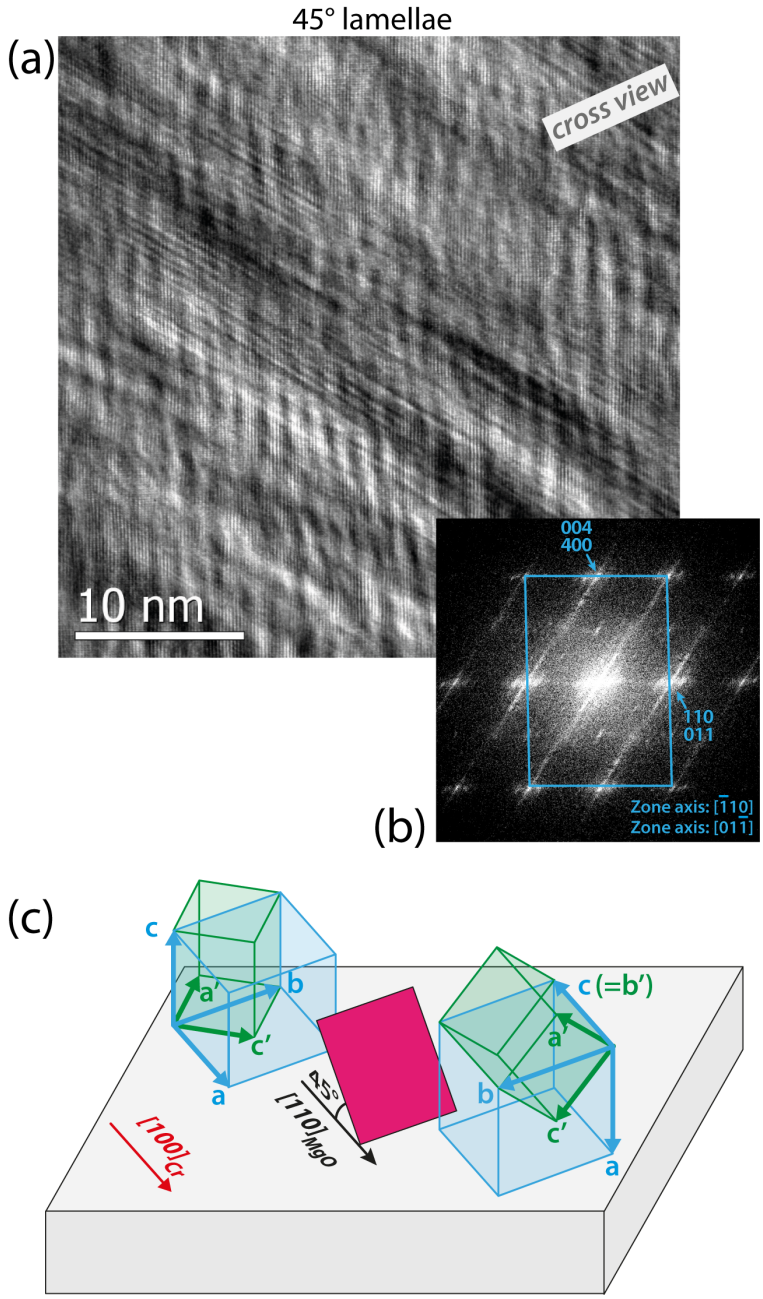

Fig. 4.8 (a) HRTEM image of twin variants with 45° lamellae. (b) FFT of the image; the two twinned reciprocal lattices cells are superimposed. (c) Scheme of the twinning planes involved and the relative martensitic cell orientations: in green the cells in the monoclinic setting, in blue the cells in the pseudo-orthorhombic setting.

The peculiar aspect emerging from the analysis of this family of twin variants (90° lamellae) is that the twinning planes, up to now described as {101} in the pseudo-orthorhombic setting for the sake of simplicity, are type-II twinning planes characterized by irrational indices. To make a step forward in the comprehension of the magnetic properties of the films, a more accurate analysis of the twinning system in the twin variants with 90° lamellae is required.

In Fig. 4.9a a cross-sectional HRTEM image of a boundary between twin variants with 90° lamellae is shown. The zoom of the rectangular area across the twin boundary, marked by the white dashed square in the figure, is superimposed to the image.

Since the two twinned crystals in type-II twin boundaries are related by a rotation of π around the η_1 axis [20], being this axis the twinning direction, the diffraction pattern acquired orienting the sample along the η_1 direction does not change across the twin.

The FFT of the HRTEM image in cross-sectional view (Fig. 4.9a) shown in Fig. 4.9b demonstrates that along the [101] direction of the pseudo-orthorhombic setting only a single diffraction pattern is observed. The observed pattern is therefore compatible with a rotation of π of the crystal around the η_1 axis. A scheme of the symmetry element related to the effect of the type-II twin in this projection is given in Fig. 4.9c. It is worth to note that even in the enlargement of the HRTEM image a clear continuity of the atomic planes across the twin boundaries is visible, a further confirmation that in this zone axis the twinned crystal is perfectly generated by a rigid rotation of one of the two twin variant around the twinning direction.

The crystallographic theory asserts that the effect of a type-II twin can also be seen as a reflection across a plane that is normal to the twinning direction in reciprocal space [20]. A mirror plane must therefore be present in the diffraction pattern of the 90° lamellae when are observed along a crystallographic direction normal to η_1. The FFT (fig. 4.10b) of the HRTEM image in planar view (shown in Fig. 4.10a) in fact shows that, if the sample is

oriented along a zone axis perpendicular to the twinning direction (as in the case of a sample seen in planar view), a mirror plane normal to η_1 is observed in the reciprocal lattice. A scheme of the symmetry element in this projection is given in Fig. 4.10c. The enlargement of the twin boundary reported in Fig. 4.10a also highlights how in HRTEM observations along an axis that differs from the twinning direction an overlap of the twinning crystals in unavoidable at the type-II twin interface, because of an irrational K_1 plane that does not correspond to an exact crystallographic plane.

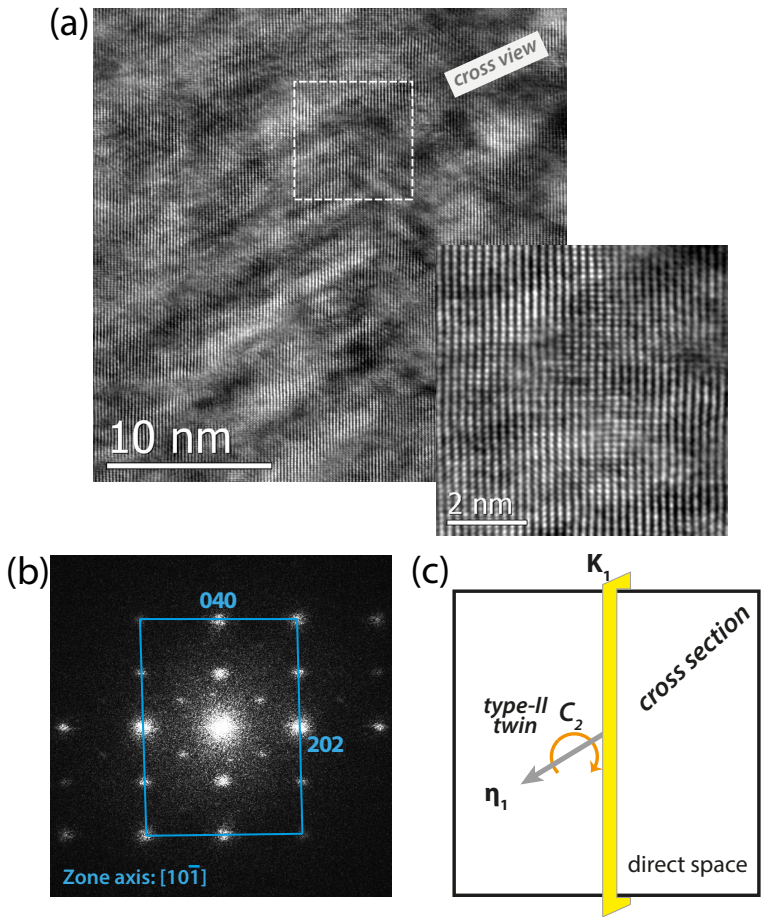

Fig. 4.9 (a) HRTEM images of 90° lamellae in cross-sectional view. An enlargement of the square area marked by the dashed line across the twinning plane is also given. (b) FFT of the HRTEM image; no noticeable effect of the twin is visible in this projection. (c) Schematic representation of the typical symmetry element characterizing a type-II twin in the direct space, when observed along the twinning direction η_1.

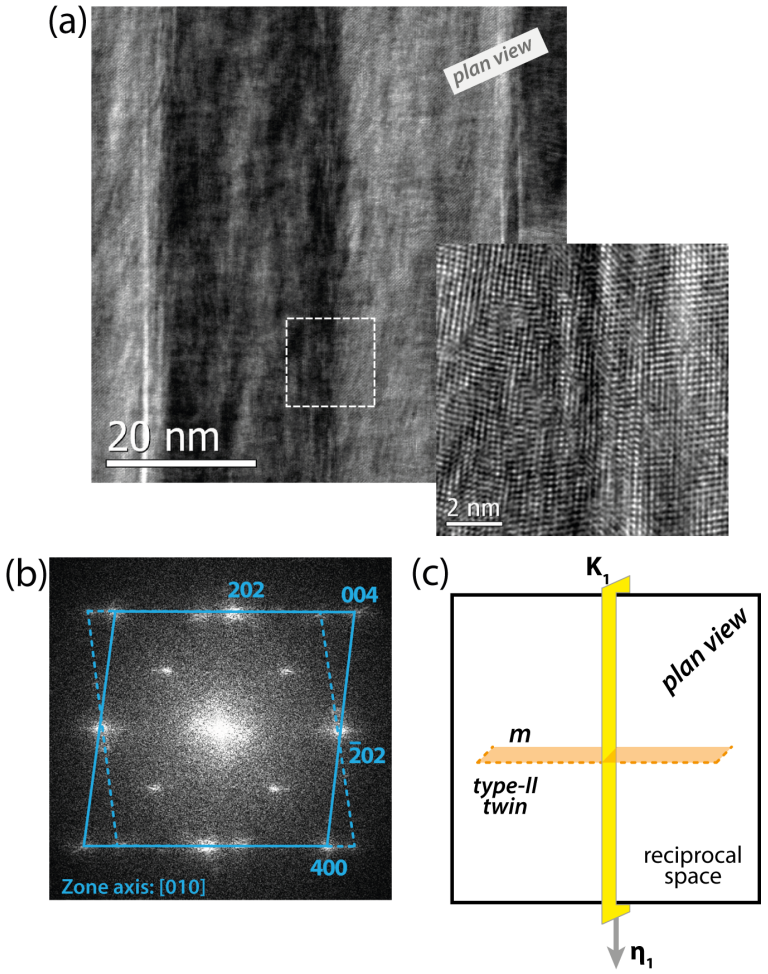

Fig. 4.10 (a) HRTEM images of 90° lamellae in planar view. An enlargement of the square area marked by the dashed line across the twinning plane is given. (b) FFT of the HRTEM image; a clear effect of the twin is visible in this projection. (c) Schematic representation of the typical symmetry element characterizing a type-II twin in the reciprocal space, when observed along a direction orthogonal to the twinning direction η_1.

The presented analysis permits to establish a well-define correlation between crystal structure and the martensitic microstructure, which is fundamental to comprehend the peculiar properties of the described film. The type of the twin boundaries in the regions directly involved in the MIR effect

has been described and the results demonstrate that the involved twin boundaries are type-II active twins for magnetic induced twin variants reorientation.

4.4.1.2 NM or 7M martensite? Visibility of structural modulation in different projections

The indexing of the electron diffraction patterns in such complex structures is sometimes tricky and ambiguous, since some peaks can be indexed in different phases with different symmetries, within the experimental error of the diffraction measurements.

For example, in literature up to now several authors have reported about the co-presence of modulated (with a monoclinic symmetry, e.g. [19, 21]) and non-modulated (abbreviated as 'NM', with a tetragonal symmetry, e.g. [22]) phases, as well as residual austenitic phase (e.g. [11]), in martensitic thin films. In particular, the absence of satellites spots in diffraction patterns of twin plates containing 90°lamellae has induced to interpret the martensitic phase involved in these twin variants as NM.

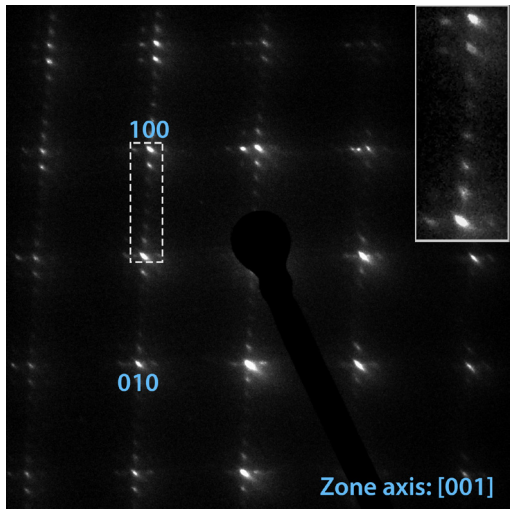

Fig. 4.11 Electron diffraction pattern of a twin plate containing 45° lamellae, in planar view. In the inset (enlargement of the area marked by the dashed line) shows the extra spots due to structural modulation, confirming the 7M character of the martensitic phase.

Chulist et al. [23] in their work have demonstrated that the structural modulation is not visible in X-ray synchrotron experiments carried out at high energy (100 keV) unless the beam direction is parallel to the c axis of the pseudo-orthorhombic structure, since the shuffling of the atomic planes distorted by the structural modulation is solely visible if it lies in the plane normal to the beam direction.

In Fig. 4.11 an electron diffraction pattern of a twin plate containing 45° lamellae observed in planar view is reported. The pattern is generated by the unavoidable superimposition of the two twinned crystals. However, one of the two twin variants is oriented with its c axis (in pseudo-orthorhombic setting) perpendicular to the plane of the film and consequently parallel to the observation direction. For these twin variants, the direction of the structural modulation lies in the plane of the film. The indexes of the main reflection for these twin variants are given in the image; six satellites are visible along the [1-10] direction of the cell, as highlighted by the inset in the figure, thus directly demonstrating that the phase is 7M.

No direct evidence of 7M modulated structure is on the contrary achieved for the twin variants with 90° lamellae, since extra spots are not visible in the electron diffraction patterns of these variants (see Fig. 4.7 and Fig. 4.10).

However, as a direct consequence of the properties displayed by the A sample, which shows a huge MIR effect that has to be related to the 90° lamellae for the considerations discussed above, we expect that the martensitic phase in the twin plates with 90° lamellae is modulated. In fact, the twinning stress of the NM martensitic phase is significantly higher than those of the modulated structures [24], hindering the magnetic induced twin variants reorientation in NM phases [25]; this phase is thus not compatible with the observed magnetic properties of our film, which display a clear MIR effect under small applied magnetic fields.

In order to achieve an experimental proof of the structural modulation from the TEM analysis, it is necessary to perform simulations and analyse more in details some not obvious features present in the experimental images.

If for example an HRTEM image of the 90° lamellae is considered in cross sectional view (Fig. 4.12a), it is clear that the alternating bright and dark stripes in a *fishbone*-like geometry cannot be simply related to some imperfection of the specimen due to the preparation processes, since they appear regularly in all the similar regions of the sample.

The simulations have been carried out using STEMCELL software [26]. This software consents to create and manipulate complex multi-domains crystalline structures and to simulate the images by the multi-slice method [27]. It is moreover possible to apply a continuous distortion to the crystal structure, with a tuneable amplitude and frequency.

In order to perform the simulations of the modulated structure the monoclinic setting is the most convenient reference system, since as described in Section 1.3.1 the structural modulation occurs along the c' axis of the monoclinic structure. In the first step, the monoclinic unit cell has been replicated in order to create a martensitic non-modulated crystal. After the crystal is created, a sinusoidal distortion along the [001] monoclinic direction is applied with a period of 14 unit cells and setting the amplitude of the distortion at the value reported for the 7M modulation in bulk crystals [19]. In this way a commensurate modulated crystal structure is created.

On the base of the analysis of the twinning plane provided in previous Section, it is evident that in order to create a twinned crystal the most convenient way is to take advantage of the projection in which the twinning can be described by an exact symmetry operation. In particular, since the 90° lamellae involve type-II twinning planes, the most suitable geometry is the one in which the observation direction is parallel to the twinning direction, being the effect of the twinning plane simply described by a C_2 axis in this projection.

Therefore to create the twinned crystal we put the sample in the monoclinic [11-1] zone axis (corresponding to the [10-1] direction in pseudo-orthorhombic setting) and we generate the second twin variant by means of a rotation of π around the zone-axis.

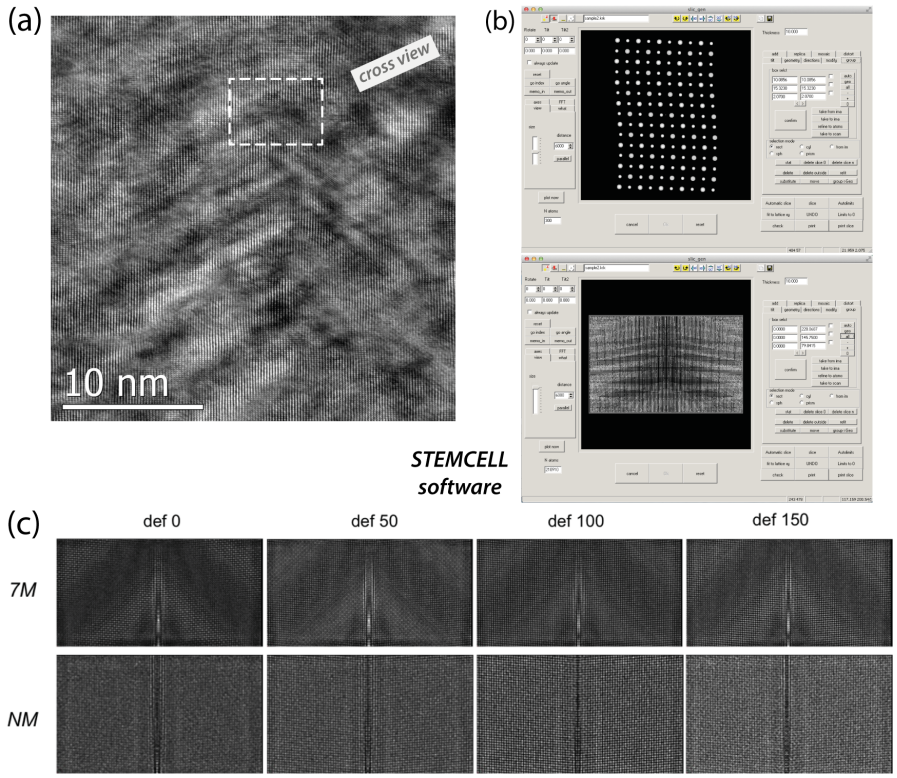

Fig. 4.12 (a) HRTEM image of 90° lamellae in cross-sectional view. (b) STEM cell software: in the slice generator tool the modulated structure and the twinned crystal are created. (c) Simulated images at different defocus values of the twinned structure created using the modulated 7M and the non-modulated (NM) cell. The features in the simulated image for the 7M structure are in good agreement with the one observed in the experimental image (e.g. dashed box in (a)).

Two screenshot of STEMCELL software windows are reported in Fig. 4.12b, the first concerning the creation of the modulated structure, the second showing the twinned superstructure. In Fig. 4.12c the simulated images at different values of defocus are shown: as can be immediately deduced, only the simulations performed using the modulated superstructure display a fishbone-like features, comparable to the ones observed in the experimental images. These features, related to local changes in diffraction contrast due to the effect of the structural modulation that is able to locally alter the Bragg diffraction conditions, are totally absent in the simulated images for the NM phase. This result is a further demonstration that the visibility of the

modulation is strongly affected by the observation direction but its effects in not-favourable projections are anyway noteworthy and discernible in high-resolution TEM images. Hence, sample A presents a 7M modulated martensitic phase also in the twin plates with 90° lamellae, accordingly to the low twinning stress observed in magnetic measurements.

4.4.1.3 Effect of external applied stress on twin variants formation

Starting from geometrical considerations and taking into account the results achieved by the TEM characterization, we are able to propose a model describing the formation of twin plates displaying a preferential orientation of the martensitic microstructure in the sample A.

This film was deposited applying a tensile shear stress on the substrate along the [100] direction of the MgO, induced by mounting the substrate on the holder of the sputtering chamber with claws along the [100] of MgO.

If we consider an unperturbed austenitic cell in the reference system of the MgO principal directions (grey cell in Fig. 4.13a), it can be easily seen that a shear stress along the [100] of MgO can produce a distortion of {1-10} atomic planes of the cubic austenite, with a small bending of the orthogonal planes {110}. Distorted cells are drawn in orange and red in Fig. 4.13a. If we image to apply a strong stress on the cell, when it is cooled down below the martensitic phase transformation temperature the most convenient twin variants that minimize the system elastic energy are the ones related by a type-II twin boundary with a twinning direction parallel to the direction of the applied stress (Fig. 4.13b): in this way, in fact, the twinning configuration minimizing the global distortion of the structure is accomplished.

From this simply geometrical analysis of the stress-induced preferential orientation of the twin variants, some other important aspects can be underlined. If we consider, for example, the martensitic axes of the displayed twinned structure (see Fig. 4.13b), we can observe that the pseudo-orthorhombic a and c axes are almost perpendicular one respect to the other but they are not collinear along the [110] direction of MgO (Fig. 4.14a).

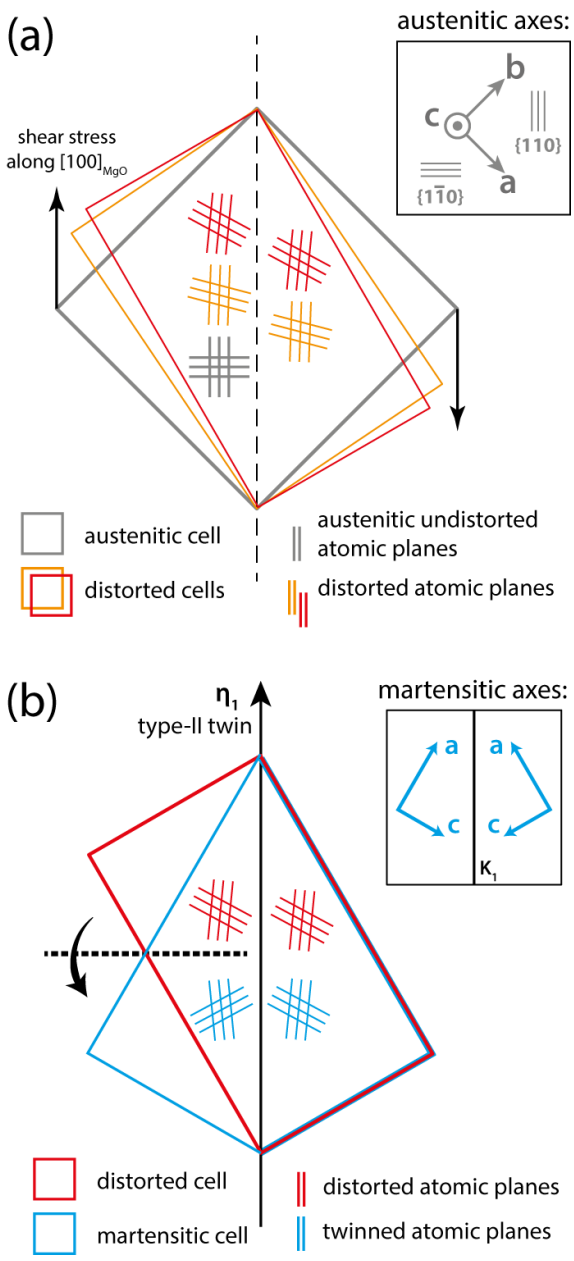

Fig. 4.13 (a) Effect (exaggerated) of a shear stress applied along the [100] direction of the MgO on the austenitic cell and its atomic planes; (b) twin variants structure generated in the described situation in order to minimize the global distortion: a type-II twin boundary is created.

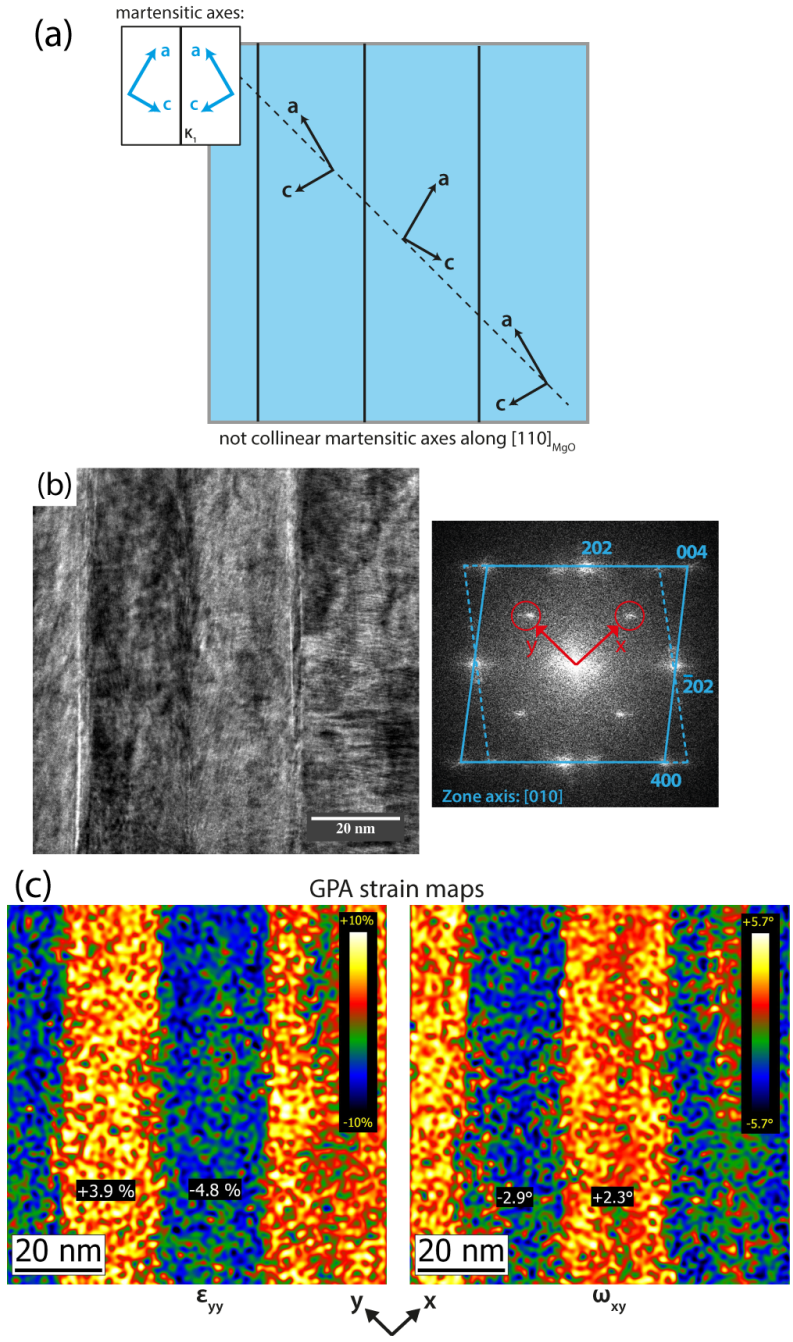

Fig. 4.14 (a) Schematic representation of the configuration of martensitic axes generated by a type-II twin boundary, corresponding to the variants shown in the HRTEM image in (b). (c) Strain maps calculated from the FFT of the HRTEM image, by means of GPA algorithm: ε_{yy} and ω_{xy} maps are shown.

This feature, strictly related to the irrational character of the twin boundary, is experimentally confirmed if a strain analysis is carried out on the HRTEM image of the planar specimen.

In order to study the effect of the type-II twin on the crystallographic axes, a non-conventional use of the Geometry Phase Analysis (GPA) algorithm is used. In particular, in the FFT of the image shown in Fig. 4.14b the two circular masks are placed in such a way so that the one along the x axis contains the (002) spot of the reciprocal lattice primary cell and the (200) spot of the twinned cell, while the masked area along the y axis contains the (200) spot of the reciprocal lattice primary cell and the (002) of the twinned cell (Fig. 4.14b, right).

Extracting the ε_{yy} map (Fig. 4.14c, left) it is possible to verify, as expected, that the pseudo-orthorhombic a and c axes alternate along the [110] MgO. In fact, for the chosen spots in the FFT of the image, the ε_{yy} map corresponds to a strain analysis along the y direction which is parallel to the [110] of MgO.

Moreover, the measured strain values are in perfect agreement with the typical lattice parameters of the martensitic phase. In fact, if the ε_{yy} map is equalized in a way so that the 0% strain corresponds to the 5.82 Å parameter of the austenite, the measured strains in two adjacent variants are -4.8% and +3.9%: the corresponding local lattice parameters are therefore the martensitic c and a axes that, as already described in Section 1.3.1, arise for a contraction and an elongation respectively of the austenitic axes.

In addition, the ω_{xy} map (Fig. 4.14c, right) clearly demonstrates that the two axes alternate along the [110] direction of MgO with a misalignment angle θ_{mis} = +2.3° for the short c axis and an angle θ_{mis} = -2.9° for the long a axis, in agreement with the proposed geometrical model (see Fig. 4.14a).

4.4.2 Magnetic properties: from the twinned domain to the macroscopic MIR

From the TEM analysis it has been demonstrated that the two different types of twin variants are generated by the presence of {101} twinning planes in the pseudo-orthorhombic setting starting from two different orientations of the martensitic unit cell, in a similar manner to what was observed in the thinner films.

In particular, it has been demonstrated that in the twin plates constituted by 90° lamellae the presence of these twinning planes induces the pseudo-orthorhombic c axis, which is associated to the easy magnetization axis of the martensitic cell of NiMnGa in the bulks, to assume two symmetric in-plane directions at the two different sides of the twin boundary (Fig. 4.7); on the contrary, in the twin plates with 45° lamellae the same twinning planes induce a flipping of the pseudo-orthorhombic c axis from an in-plane direction to an out-of-plane one (Fig. 4.8).

From the described MFM measurements, previously reported (Section 4.3), an out-of-plane component of the magnetization was observed in the twin plates constituted by 45° lamellae, while an in-plane configuration of the magnetization was compatible with the absence of magnetic signal for the twin plates with 90° lamellae. It must be stressed, however, that MFM is not sufficient to completely describe the local magnetic properties of the martensitic phase.

In fact, beside the lack of information about the twin variants having their magnetization lying in the plane of the film, the results achieved by scanning probe techniques on large areas do not consent a direct correlation between the structure and the magnetism of each fine twinning domain in the martensitic microstructure.

To achieve this deeper comprehension, electron holography was employed to study the magnetic properties of the martensitic phase at the nanoscale.

As described in Section 1.4.4.1, performing an experiment of electron

holography we are able to restore the magnetic phase shift and hence the in plane components of the magnetic induction.

Since we are able to study the planar components of the magnetization, on the basis of the aforementioned crystallographic orientations the most convenient solution in order to study the magnetic domains of the film in the different configuration of twin variants is to analyse the twin plates showing 90° lamellae in planar view and analyse the twin plates with 45° degrees lamellae in cross-sectional view.

In Fig. 4.15a a hologram acquired close to the vacuum in the planar specimen is reported. It is possible to recognize the 90° lamellae which show a lateral size of about 20 nm. From the magnetic induction flux map (Fig. 4.15b), approximated by contours of equal phase shift, it is clear that the magnetization inside each lamella is oriented parallel to the easy axis of magnetization. Moreover, it is worth to note that, accordingly to the analysis reported above, the angle between the magnetization vectors of two adjacent lamellae slightly differs from 90°. Remarkably, the observed angular deviation is in very good agreement with the previously reported analysis regarding the slight misalignment of the c axes of the cells with respect to the [110] of MgO (see Fig. 4.14).

In Fig. 4.15c, the magnetic induction colour map is shown; the colour is related to the direction of the magnetization vector, the saturation to its intensity. As can be seen from the uniformity of the colour inside each lamella, in the area corresponding to the field of view of the image no domain boundaries between different planar configurations with antiparallel magnetizations are visible inside each lamella. It has to be underline, however, that the domain boundaries observed by means of MFM measurement in the twin plates with 90° lamellae (Fig. 4.3b) separate magnetic domains with a lateral size in the range from hundreds of nm to few μm. The size of the region analysed by electron holography is remarkably smaller than the typical lateral size of this kind of domains.

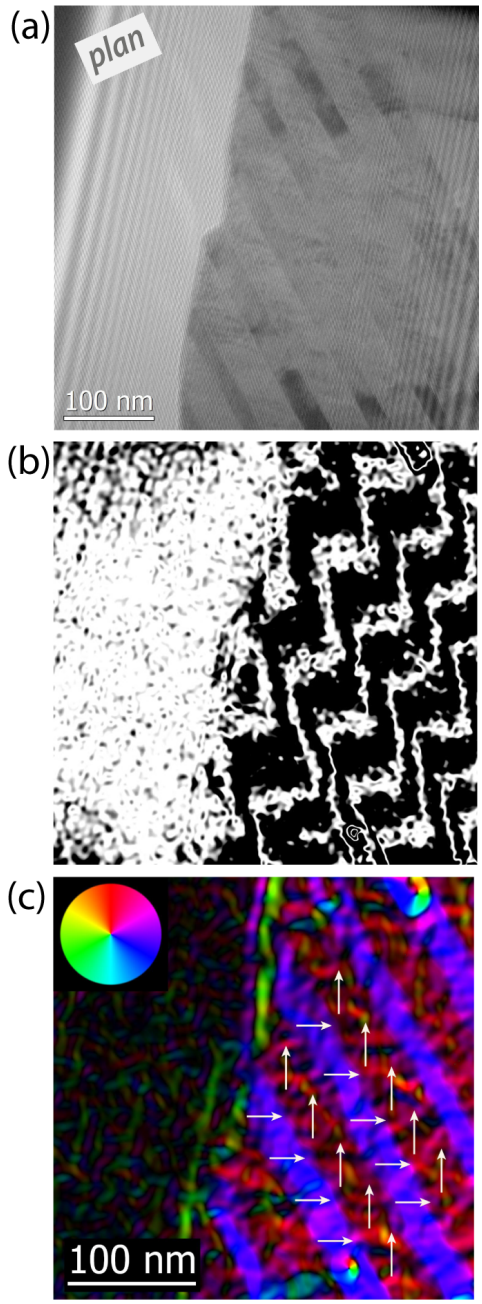

Fig. 4.15 (a) Electron hologram of twin plates with 90° lamellae, in planar view. (b) Contour map showing the magnetic induction flux lines. (c) Magnetic induction colour map: the colour gives the magnetization vector direction, the saturation its intensity. The magnetization of each lamella is schematized by the white arrows.

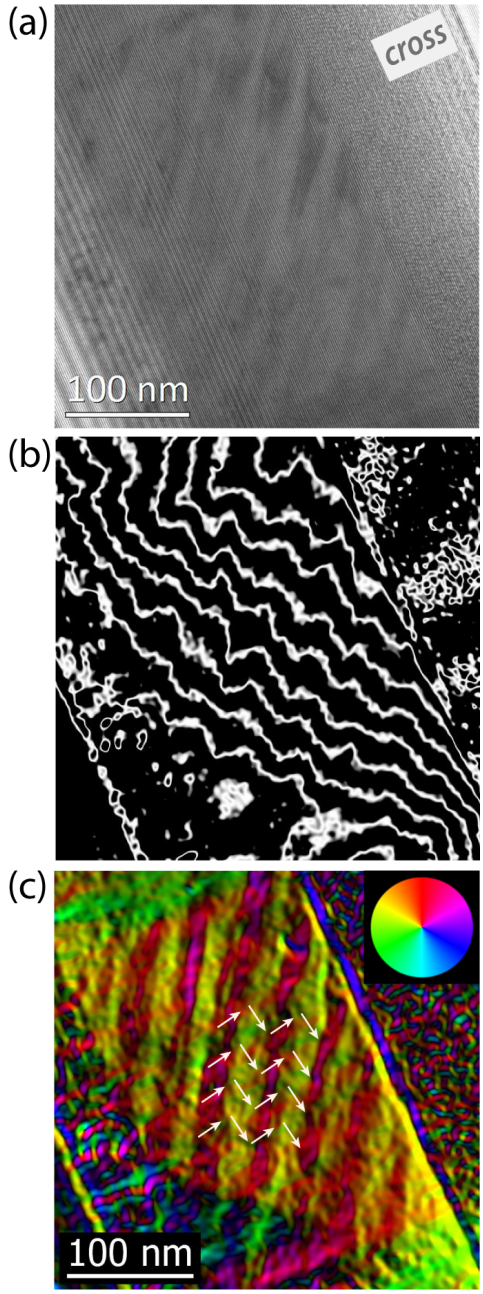

Fig. 4.16 (a) Electron hologram of twin plates with 45° lamellae, in cross-sectional view. (b) Contour map showing the magnetic induction flux lines. (c) Magnetic induction colour map: the colour gives the magnetization vector direction, the saturation its intensity. The magnetization of each lamella is schematized by the white arrows.

In Fig. 4.16a a hologram of a twin plates showing 45° lamellae in cross-sectional view is shown. On the base of the structural analysis, the easy axis of magnetization is twinned from a direction contained in the film plane to a direction out of the film plane. From the magnetic induction flux lines (Fig. 4.16b) it is evident that the correspondence of the easy axis of magnetization and the magnetization inside each lamella is respected. In Fig. 4.16c, the magnetic induction colour map is shown. It can be concluded that the out of plane signal seen in the MFM measurement for twin plates with 45° lamellae is generated by half of the twin variants constituting the plates.

The holographic measurements confirm and validate the structural analysis for both the configuration with 45° and 90° lamellae. The presented results, moreover, demonstrate that in NiMnGa martensitic thin films there is a one to one correspondence between the easy direction of magnetization and the magnetization of each lamella inside the twin plates. This is a key aspect that must be taken into account in the development of a magnetic model for the MIR process.

In particular, on the basis of the different magnetic behaviours displayed by the considered thin films, which are correlated to their different microstructure, after an in-depth TEM analysis finalized to characterize the structural and magnetic properties from the micro to the nanoscale, the following conclusions can be asserted:

i. The MIR effect is displayed in thin films characterized by a martensitic microstructure in which different twin plates, constituted by 45° and 90° lamellae respectively, coexist. In fact, no MIR effect is observed in the thin film displaying only one family of twin variants (as observed for sample C).
ii. The films displaying a martensitic microstructure in which twin plates constituted by 45° and 90° lamellae coexist, display a MIR effect if an external magnetic field is applied along one of the principal direction of the MgO substrate (as observed for sample B). The reported results

reveal that a strong interaction between the different plates with 45° and 90° lamellae occur.

iii. The entity of the observed MIR can be highly enhanced if a preferential orientation of the martensitic microstructure is induced in the film (as observed for sample A). In this case, such MIR effect is huge and anisotropic. Since the effect is only displayed along the preferential orientation of the twin plates containing 90° lamellae, which are separated by highly mobile type-II twins, these twin variants are the ones involved in magnetic induced twin variants reorientation. On the base of the described experimental results, it is evident that a model for the MIR effect should be developed taking into account, in addition to the conservation of the film shape due to epitaxial constrains, the complex magnetic structures of both twin plates containing 45° and 90° lamellae respectively.

4.5 From the constrained thin film to free-standing structure

In this Section, the realization procedure and the preliminary characterizations of a free-standing films are reported, highlighting the peculiar aspects of the martensitic structure and microstructure and investigating the martensitic phase transition.

4.5.1 Preparation of the free-standing film

The described film, displaying the anisotropic MIR effect (sample A), has been removed by the substrate by means of a selective wet etching for the Cr layer. In particular, the etching was carried out following the procedure reported in literature by using a solution of ceric nitrate [13-15]. To perform the etching, a 2x3 mm^2 portion of the film was immersed in the etchant solution;

after 15 min, the release of the film begins and it is completed after about 30 min. The obtained free-standing film, floating on the solution surface, is caught using a TEM Cu-grid and, after several washes with de-ionized water, dried in a desiccator. In order to make the film thin enough for the TEM observation, a further thinning by precision ion polishing system (PIPS) or by ion-beam milling is necessary. It this way it is possible to reduce the thickness of the film from the nominal value of 200 nm down to tens of nm permitting its observation as a planar specimen.

In the next paragraphs, the martensitic microstructure and the martensitic phase transition in the free-standing structure are analysed by means of TEM investigations.

4.5.2 Martensitic microstructure and phases

The prepared sample shows a martensitic microstructure in which martensitic twin plates are easily identifiable. In Fig. 4.17, a conventional TEM image at low magnification is reported.

The two kinds of martensitic plates constituted by 90° and 45° lamellae are visible in the most part of the image; the line generated by twinning planes at the surface are marked in the figure for both the twin plates with 45° and 90° lamellae, by purple and yellow lines respectively. The preferential orientation of the microstructure is preserved and it is displayed in the figure along the direction indicated by the white arrow. However, twin plates oriented in the perpendicular direction are also present (marked in the figure by dashed arrows). In the left part of the image, an area that does not display the martensitic microstructure is visible: the sample preparation processes damaged the film in this part of the sample.

In order to analyse the structural properties of the free standing specimen, high-resolution TEM was employed. An HRTEM image of a twin boundaries separating 90° lamellae is reported in Fig. 4.18a.

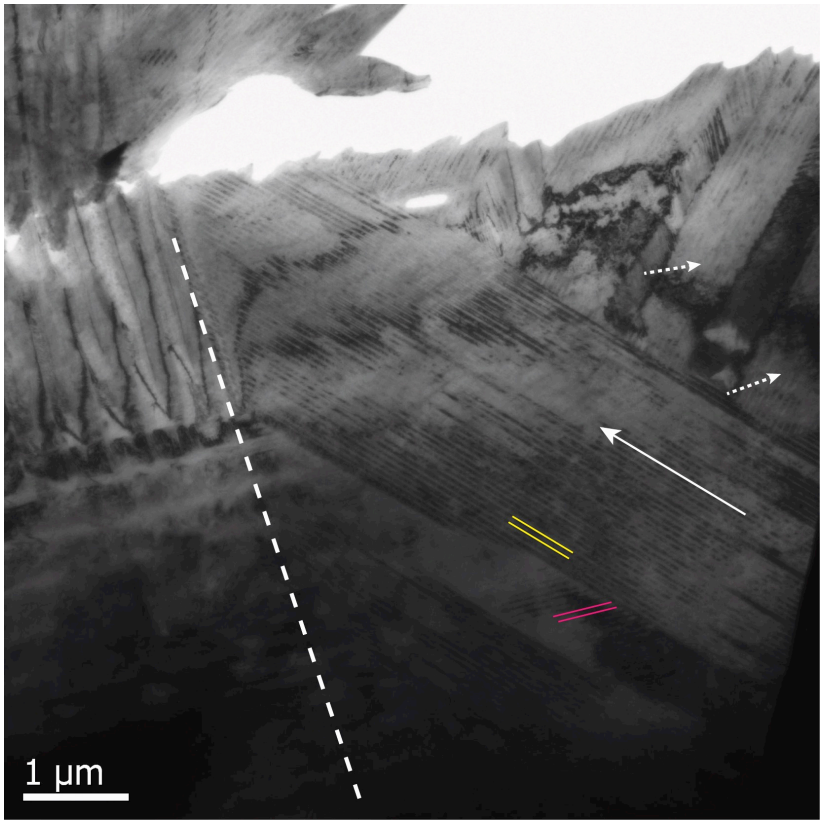

Fig. 4.17 Low magnification TEM image of the free-standing film obtained by the sample A, after the further preparation by PIPS. 90° and 45° lamellae are recognizable (yellow and purple lines, respectively). The preferential orientation of the microstructure is preserved (along the direction indicated by the white arrow) but twin plates oriented in the perpendicular direction are also visualized (dashed arrow). The area of the sample in the left part of the image, indicated by the dashed line, was damaged in the sample preparation.

The two lamellae in the centre and in the right part of the image exhibit a monoclinic phase, as highlighted from the FFT shown in the inset. In addition to the monoclinic phase (that was the only one observed in the starting film) a small amount of tetragonal phase is present in the free-standing film. The presence of this additional phase is demonstrated by the FFT of the twin variant in the left part of the image, in which the spots can be indexed in the tetragonal system. The crystal structure and lattice parameter are for the tetragonal phase are given in Table 4.2.

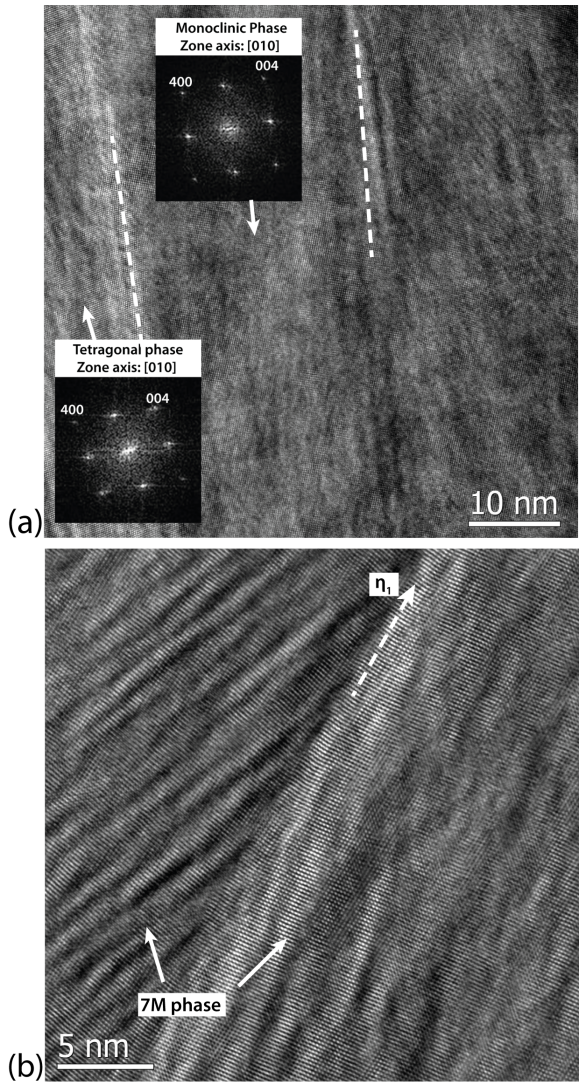

Fig. 4.18 (a) HRTEM image of 90° lamellae in the free-standing film. The FFT in two different areas are shown in the insets. Beside the monoclinic phase, also the tetragonal one is observed. (b) HRTEM image at higher magnification of a type-II twin boundary between 90° lamellae showing a monoclinic 7M phase. The twinning direction is marked by the dashed line.

System	Lattice parameters
Tetragonal (I4/mmm)	a = b = 5.45 Å, c = 6.65 Å

Table 4.2 Lattice parameters for the tetragonal phase observed in the free-standing film.

In Fig. 4.18b, a HRTEM image at higher magnification of a twinning plane between two 90° lamellae displaying a monoclinic 7M phase is shown: the interface region between the twin variants is characterized by a superimposition of the two crystals, thus demonstrating that even in the free standing film the boundaries are type-II twins. The modulation in the monoclinic phase is not directly visible in the diffraction patterns of these areas for the already discussed visibility problems, being a fishbone-like modulation in the contrast of the image the only indirect evidence of the modulated character of the martensitic phase.

However, a direct analysis of the modulation can be carried out taking into account the twin variants containing 45° lamellae. In Fig. 4.19, an electron diffraction pattern of twin variants with the c axis out-of the plane of the film is reported. Besides strong dynamical diffraction effects, due to the sample thickness, the presence of 6 satellites is immediately visible thus confirming the 7M modulated phase.

Since the presence of small amounts of tetragonal phase was observed in the thinner areas of the sample, it is reasonable to think that the specimen phase is preserved during the etching of the Cr layer, while defects and local alteration of the martensitic phase can be induced by the further thinning procedure for the TEM analysis by ion milling/PIPS.

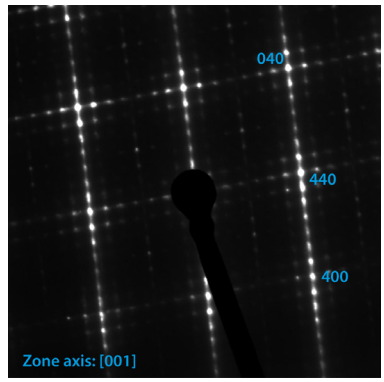

Fig. 4.19 Electron diffraction pattern acquired in a zone showing 45° lamellae. In particular the monoclinic phase is oriented with its c axis perpendicular of the film planes. The satellites of the modulated structure are therefore directly visible in this projection

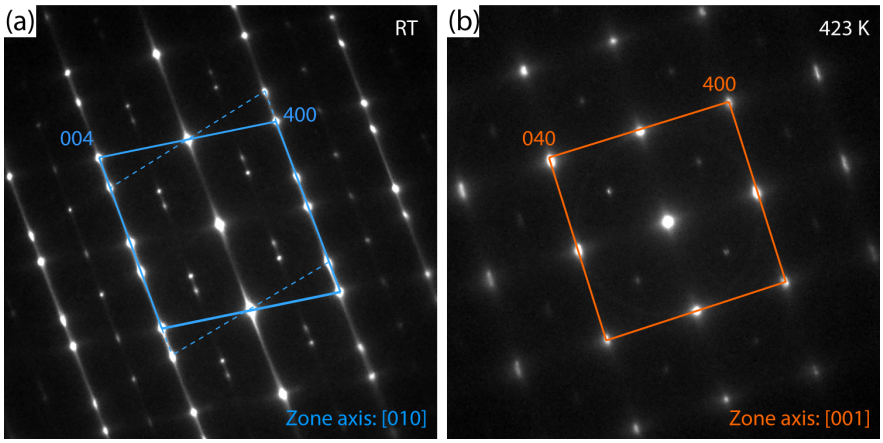

Fig. 4.20 (a) Electron diffraction pattern taken at RT in a region containing 90° lamellae. The two reciprocal lattice cells are marked by the continuous and dashed blue lines respectively. (b) Electron diffraction pattern showing the peaks of the austenitic cubic phase observed after heating the free-standing film at 423 K.

4.5.3 Exploring the martensitic phase transition

The behaviour of the obtained free-standing film has also been analysed in function of the temperature; in particular, employing an heating holder is possible to heat the sample above the martensitic phase transformation temperature to investigate the austenitic phase. Since the free-standing sample was deposited on a TEM grid the heating process by thermal conduction in the system was not optimal.

We observed a complete transition from the martensitic to the austenitic phase at a nominal temperature of the holder of 423 K, but probably corresponding to a lower temperature on the specimen. It is remarkable to note that the first twin plates which disappear are the ones containing 45° lamellae. Then, after the twin plates containing 45° lamellae are completely disappeared, the phase transformation also occurs for the twinning plates with 90° lamellae.

In Fig. 4.20a the diffraction patter acquired at RT in a zone containing 90° lamellae is shown. In Fig. 4.20b, the electron diffraction pattern of the austenitic phase at 423 K is shown. The estimated lattice parameter for the

austenitic phase is a_A= 5.79 Å, in well agreement with the typical values reported for NiMnGa bulk single crystals. From the electron diffraction investigation it is possible to conclude that the habit plane is a plane (101) of the pseudo-orthorhombic structure, which corresponding to a (12-1) plane in the monoclinic setting.

References

[1] M. Acet, L. Mañosa and A. Planes, *Handbook of Magnetic Materials,* 2011, 19,231.

[2] K. Ullakko, J. K. Huang, C. Kantner, R. C. O'Handley, V. V. Kokorin, *Appl. Phys. Lett.* 1996 69, 1966.

[3] D. C. Dunand and P. Müllner, *Adv. Mater.,* 2011, 23, 216.

[4] M. Thomas, O. Heczko, J. Buschbeck, Y. W. Lai, J. McCord, S. Kaufmann, L. Schultz and S. Fähler, *Adv. Mat.,* 2009, 21, 3708.

[5] K. Bhattacharia, S. Conti, G. Zanzotto and J. Zimmer, *Nature,* 2004, 428, 55.

[6] A. N. Vasil'ev, V. D. Buchel'nikov, T. Takagi, V. V. Khovailo and E. I. Estrin, *Phys. Usp.,* 2003, 46, 559.

[7] A. A. Cherechukin, I. E. Dikshtein, D. I. Ermakov, A. V. Glebov, V. V. Koledov, D. A. Kosolapov, V. G. Shavrov, A. A. Tulaikova, E. P. Krasnoperov and T. Takagi, *Phys. Lett. A*, 2001, 291, 175.

[8] R. Kainuma, Y. Imano, W. Ito, Y. Sutou, H. Morito, S. Okamoto, O. Kitakami, K. Oikawa, A. Fujita, T. Kanomata and K. Ishida, *Nature*, 2006, 439, 957.

[9] I. Aaltio, A. Saroka, Y. Ge, O. Soderberg and S. P. Hannula, *Smart Mater. Struct.*, 2010, 19, 075014.

[10] K. Bhattacharia and R. D. James, *Science*, 2005, 307, 53.

[11] M. Thomas, O. Heczko, J. Buschbeck, U. K. Rossler, J. McCord, N. Scheerbaum, L. Schultz and S. Fähler, *New J. Phys.*, 2008, 10, 023040.

[12] O. Heczko, M. Thomas, J. Buschbeck, L. Schultz and S. Fahler, *Appl. Phys. Lett.*, 2008, 92, 7, 072502.

[13] Y. Zhang, R. A. Hughes, J. F. Britten, J. S. Preston, G. A. Botton and M. Niewczas, *Phys. Rev. B*, 2010, 81, 054406.

[14] C. A. Jenkins, R. Ramesh, M. Huth, T. Eichhorn, P. Pörsch, H. J. Elmers and G. Jakob, *Appl. Phys. Lett.*, 2008, 93, 234101.

[15] A. Backen, S. R. Yeduru, M. Kohl, S. Baunack, A. Diestel, B. Holzapfel, L. Schultz and S. Fähler, *Acta Mater.*, 2010, 58, 9, 3415-3421.

[16] O. Heczko, M. Thomas, J. Buschbeck, L. Schultz, and S. Fähler, *Appl. Phys. Lett.*, 2008, 92, 072502.

[17] O. Heczko, *IEEE Trans. Magn.*, 2014, 50, 11.

[18] P. Ranzieri, S. Fabbrici, L. Nasi, L. Righi, F. Casoli, V. A. Chernenko, E. Villa and F. Albertini, *Acta Mater.*, 2013, 61, 263.

[19] L. Righi, F. Albertini, E. Villa, A. Paoluzi, G. Calestani, V. Chernenko, S. Besseghini, C. Ritter and F. Passaretti, *Acta Mater.*, 2008, 56, 4529.

[20] Y. Zhang, Z. Li, C. Esling, J. Muller, X. Zhao and L. Zuo, *J. Appl. Cryst.*, 2010, 43, 1426-1430.

[21] U. Gaitzsch, S. Roth, B. Rellinghaus and L. Schultz, *J. Magn. Magn. Mater.*, 305, 1,

2006, 275-277.

[22] S. Kaufmann, R. Niemann, T. Thersleff, U. K. Rößler, O. Heczko, J. Buschbeck, B. Holzapfel, L. Schultz and S. Fähler, *New J. Phys.*, 2011, 13, 053029.

[23] R. Chulist, C.-G. Oertel, W. Skrotzki and T. Lippmann, *Scripta Mater.*, 2010, 62, 235-237.

[24] A. Sozinov, A. A. Likhachev, K. Ullakko, *IEEE Trans. Magn.*, 2000, 36, 3266.

[25] A. Sozinov, A. A. Likhachev and K. Ullakko, *Proc. SPIE*, 2001, 4333, 189.

[26] V. Grillo, F. Rossi, *Ultramicroscopy*, 2013, 125, 112-129.

[27] E. J. Kirkland, *Advanced Computing in Electron Microscopy*, Springer Science, 2010.

5 The reduction of dimensionality in NiMnGa martensitic systems: from thin films to nano-disks

5.1 Introduction

In many fields of physics the reduction of the dimensionality of a system induces a strong modification in its peculiar properties, sometimes opening new perspective in already known phenomena. In particular, in the recent past the advent of nanostructured materials, able to bridge the gap between properties of bulk materials and the discrete atoms has revolutionised some conventional concepts of physic and materials sciences [1-5]. The possibility to obtain new functional properties in known materials by scaling down the dimensionality of the system represents an extraordinary challenge to deepen the basic acknowledge regarding complex systems and, at the same time,

offers new prospects in technological innovation [6-9].

Very different materials have been reported to show very strong effects at the reduction of their dimensionality [10-14]. In this framework, shape memory alloys are intrinsically very interesting since yet their macroscopic behaviour is strongly influenced by the micro and nanostructure.

In the recent past a great attention was devoted to the realization of martensitic thin film exploitable in micrometric devices [15-17]. The fruitful efforts in the achievement of martensitic thin films have promptly raised inevitably issues about the effects of the epitaxial constrains on the microstructure of martensitic thin films. In the previous Chapters these aspects have been widely discussed and the complex behaviour of martensitic films was described.

This emerging interest on the martensitic materials in the form of thin films, promising thanks to their easy feasibleness, opens at the same time new relevant questions concerning the reduction of the dimensionality from the bulk single crystals, that can be ascribed as the three-dimensional (3D) martensitic phase, toward the two-dimensional (2D) systems, as martensitic films. In martensitic thin films, as demonstrated by the analysis proposed in the previous Chapters, the complex structure of the martensitic phase is organized in a hierarchical configuration involving different length scales of the material.

At the lower scale length, the nanostructured thin lamellae represent the smaller entities of the martensitic system. Each lamella is univocally defined by its structural and magnetic properties and it is in a strict relationship with the other adjacent lamellae, thanks to complex symmetry elements.

At an higher level of this hierarchical structure, the existence of twin plates constituted by a huge number ($> 10^2$) of twin variants with well-defined orientations determines the final film microstructure and, as demonstrated in the previous Chapter, has also a primary role on the macroscopic properties exhibited by the film.

As a direct consequence of this strong correlation at different length scales, also the magnetic properties at the macroscopic scale cannot be correctly

described if the system is not considered in all its constituent parts. In particular, the ability of inducing high strains in MSM alloys by applying an external magnetic field involves a deep modification of the material properties on all the characteristic lengths of its hierarchical structure: the MIR effect, for example, is possible thanks to a rearrangement of atoms inside the lamellae, due to the mobility of twin boundaries. This arrangement is the result of a complex and dynamical equilibrium between the elastic and magnetic energies, which finally determines the most stable microstructure displayed by the film.

In this Chapter the effects of the further reduction of the dimensionality of the NiMnGa systems, from the thin films to nano-disks, are discussed. For this new kind of sub-micrometric materials, the transmission electron microscopy characterization, carried out by combining different techniques, represents a unique tool to investigate the structural and magnetic properties and the effect of lateral confinement on the martensitic phase, characterizations not achievable by any other technique.

In Section 5.2 the experimental procedures for the preparation of the NiMnGa nano-disks are described. In Section 5.3 a step-by-step TEM characterization, from the continuous thin film to the free-standing nano-disks, is given with the aim to highlight the structural modifications induced by both the lateral confinement and the release of the epitaxial constrains. In Section 5.4 the magnetic characterization of the free-standing disks by means of Lorentz microscopy is presented and the results are correlated to the observed martensitic structure. In Section 5.5 and 5.6, the effects of the martensitic phase transition on the martensitic structure and the magnetic properties of the disks are discussed, revealing the actuation mechanisms that remain active at the reduction of the NiMnGa system dimensionality.

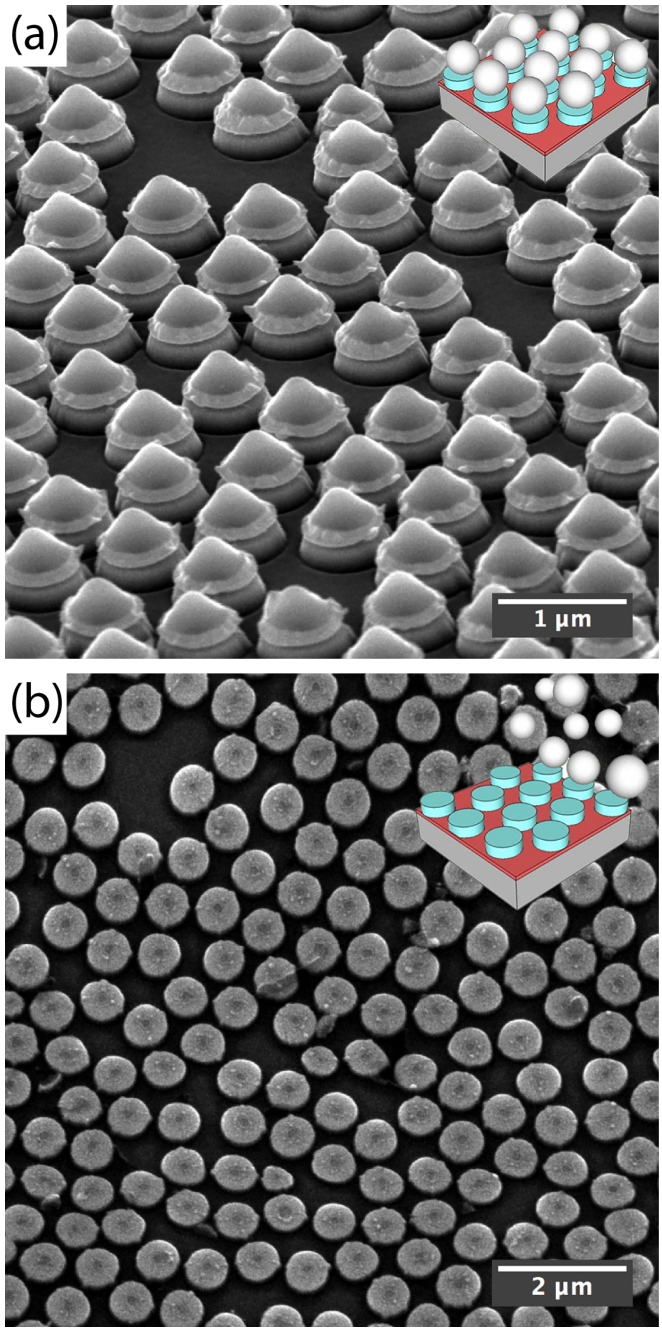

Fig. 5.1 (a) SEM image of the patterned film after the reduction of the sizes of polymeric spheres, used as capping agent, by RIE process. (b) SEM image of the patterned film after the removal of the spheres: martensitic nano-disks are obtained.

5.2 Nano-disks preparation

The preparation of NiMnGa nano-disks starts from the continuous thin film, which can be considered as a 2D system confined along the direction perpendicular to the film plane.

The realization of the structures at lower dimensionality was carried out by exploiting a top-down approach. In particular, by combining lithographic techniques and taking advantage of the availability of a selective etchant for the sacrificial Cr under-layer (as already mentioned in the previous Chapters), it is possible to create a patterned structure of martensitic nano-disks on the substrate, as well as a suspension of free-standing disks.

The realization of the patterned structure is done by means of the *nanospheres lithography* process [18]. The first step of the process consists in depositing on the continuous thin films a self-assembled layer of polymeric spheres, which acts as a protective mask for the regions of the film that we would like to preserve. The as-deposited spheres are in contact one to each other and, in order to create isolated structures, the lateral size of the spheres needs to be reduced removing the contact points between them. This can be done by using a reactive ion etching (RIE) ablation [18].

Once the spheres diameters have been reduced, removing the contact points between them, the patterning of the NiMnGa film is realized by a sputter etching process, which removes the film in the areas not protected by the spheres. In this way a patterned film constituted by a large number of nano-disks, covered by the protective polymeric spheres, is obtained, as shown in SEM image reported in Fig. 5.1a.

The subsequent step, consisting in washing the patterned film in methylene in an ultra-sonicating bath, permits to eliminate the capping layer of protective spheres. A patterned NiMnGa film on the Cr under-layer is thus successfully obtained, as confirmed by the SEM image reported in Fig. 5.1b.

In order to obtain the free-standing nano-disks another step is required, consisting in the etching of the Cr under layer using the same etchant solution

employed in the realization of free-standing thin films (see also Section 4.5.1). When the etching is completed, the obtained suspension is filtered to remove the by-products of the etching. The filtered suspension is then subjected to a sequence of repeated steps of centrifuging and redispersion in milliQ water, necessary to remove the residual ceric ammonium nitrate from the suspension. In this way, an aqueous suspension of free-standing NiMnGa disks is obtained.

Following the described procedure, martensitic disks with different diameters can be obtained. Starting with polymeric spheres with a diameter of 800 nm, thanks to the reduction of the lateral size by RIE process, NiMnGa nano-disks with a diameter of 600 nm are produced. By properly tuning the sputter etching parameters, moreover, it is possible to ablate films with different thicknesses and obtain different martensitic nanostructures.

From a preliminary work, the optimal conditions for the lithographic process have been established. In particular, it is worth to remember that even by opportunely tuning the process parameters, in order to reduce the ablation yield and rate, unavoidable damages are produced in the films with thicknesses lower than 75 nm. The films with thicknesses equal or higher than 75 nm are instead successfully patterned by the nanospheres lithography, process without evident damaging of the martensitic film.

In this Chapter, the TEM characterization carried out on disks obtained by the patterning of the continuous NiMnGa thin film 75 nm thick, previously described in Section 3.4.1, is reported. The TEM characterization of disks obtained starting from film with higher thicknesses, instead, results difficult or unachievable.

5.3 Structural and magnetic properties of the patterned film

A step-by-step TEM investigation allows a complete characterization the samples structure and morphology during the patterning processes. In Chapter 3, the NiMnGa films grown on Cr under-layer were analysed in details:

in particular, for thicknesses below 100 nm a martensitic microstructure characterized by 90° lamellae and an in-plane easy axis of magnetization was observed. A low magnification bright field TEM image of the cross sectional specimen of the continuous film 75 nm thick is reported in Fig. 5.2a.

After the last step of the nanospheres lithography process consisting, as explained above, in the removal of the capping protective spheres from the top of the laterally confined martensitic structures (Fig. 5.1b), a new TEM cross-sectional specimen was prepared by means of focus ion beam to check the effects induced by the lithographic processes on the martensitic phase. A low magnification bright field TEM image of this specimen is shown in Fig 5.2b.

The section of the disks is recognizable and the peculiar features of the martensitic microstructure appear to be preserved; in particular, the same microstructure with 90° lamellae which was observed in the continuous film is displayed also in the disks. In addition, the reported image shows that the patterning process remove the also the Cr layer in the unprotected zones. In Fig. 5.2c, an HREM image of the Cr/NiMnGa interface demonstrate that the epitaxial relationships and the martensitic cell orientation are unchanged (see for comparison Fig. 3.5 in Chapter 3), preserving the same preferential orientation of the magnetization easy axis in the plane of the film and parallel to the [110] direction of the MgO substrate.

Also the magnetization measurements confirm the observed morphology: in Fig. 5.3a the in-plane hysteresis loops measured with the external magnetic field applied parallel to [100] direction of MgO are shown for both the continuous thin films (“as prepared”) and the patterned film (“dotted”). No significant differences in the coercivity are observed, thus demonstrating the lack of structural changes in the martensitic phase due to the lateral confinement produced by the patterning. In the curves, the magnetization values have been normalized to the saturation value in order to compare the trends and thus avoiding misleading effects due to the reduce amount of magnetic material in the patterned film compared to the continuous one.

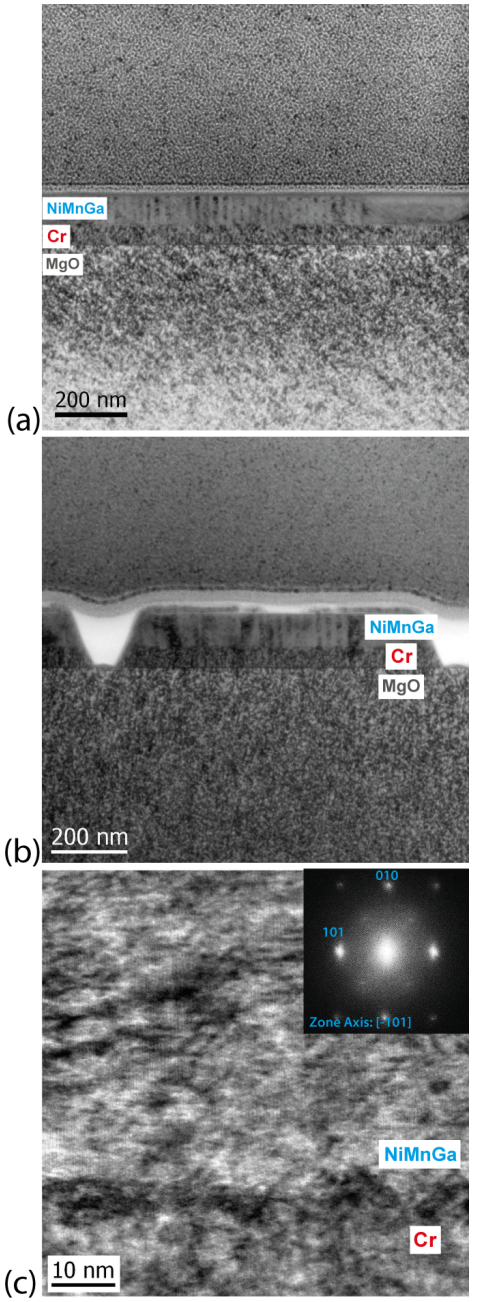

Fig. 5.2 Low magnification bright field TEM images of (a) the continuous NiMnGa thin films 75 nm thick on Cr under-layer (50 nm) and (b) patterned thin film obtained after the removal of polymeric spheres. (c) HRTEM image of the interface between Cr and NiMnGa, in a NiMnGa disk.

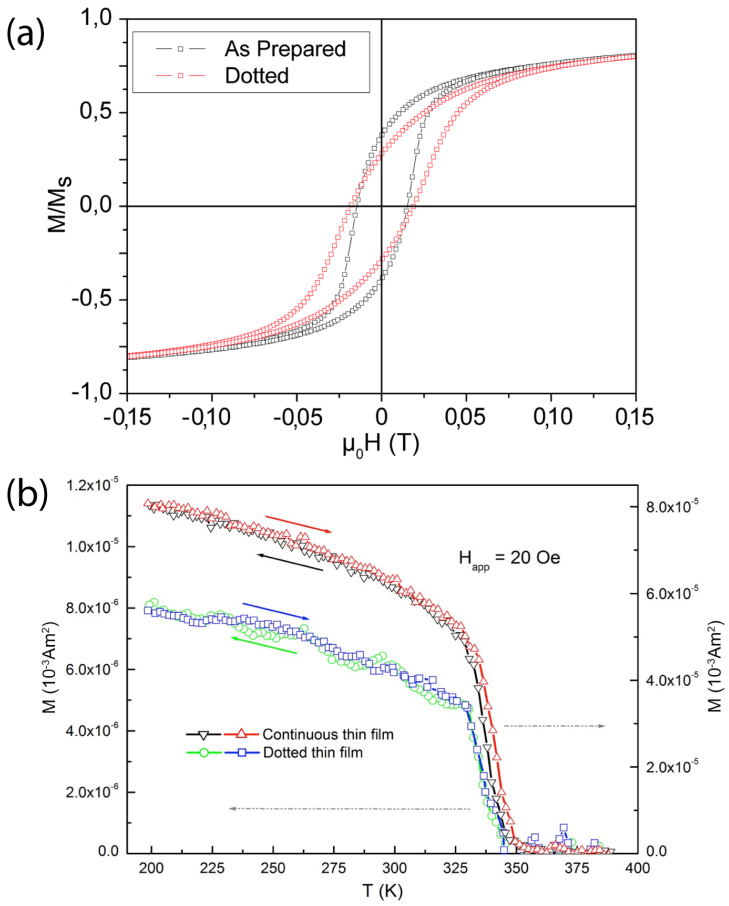

Fig. 5.3 (a) Hysteresis loops for the as-deposited film and the patterned one, measured by applying the external magnetic field along the [100] direction of MgO. No significant differences in coercivity are observed. (b) Temperature behaviour of magnetization under an applied magnetic field (1.6 kA/m) along the (100) direction on MgO for both the continuous and the patterned thin films.

In Fig. 5.3b the temperature dependent behaviour of the magnetization is reported, demonstrating the survival of the martensitic phase transformation, which is observed at the same temperature ($T_M \approx 346 \pm 3$ K) for both the continuous and patterned films.

The characterizations demonstrate that the patterning of the film does not alter the martensitic microstructure and the salient magnetic properties of the martensitic phase of the NiMnGa film.

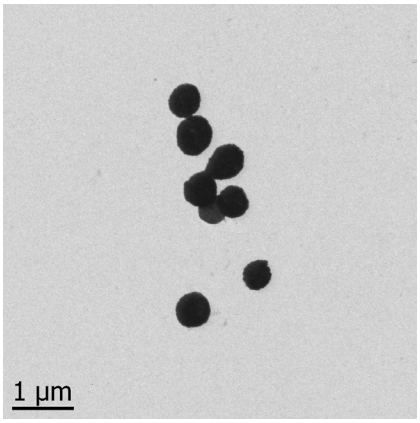

Fig. 5.4 Low magnification bright field TEM image of disks deposited on TEM carbon coated grid.

5.4 Structure and magnetism in free-standing NiMnGa disks

5.4.1 Morphology and crystal structure

After the etching of the Cr under-layer, the suspension of free-standing disks is obtained. If some drops of the suspension are deposited on a TEM carbon grid, the disks can be analysed by transmission electron microscopy.

The analysed TEM specimen (of disks 75nm thick) displays different structures of martensitic disks. In particular, isolated disks but also groups constituted by few disks connected by small linking points are observed, as shown in the low magnification TEM image reported in Fig. 5.4.

The STEM-HAADF image in Fig. 5.5a shows a group of three disks, which are connected by small bridges of not properly removed material. These linking points between the disks can be ascribed to local irregularities of the capping layer of polymeric spheres that affect the efficiency of the RIE process in reducing of the spheres size.

Acquiring an image at a higher magnification (Fig. 5.5b) of the disk marked by the orange rectangle in Fig. 5.5a, different martensitic plates are visible with a slightly different contrast in the image.

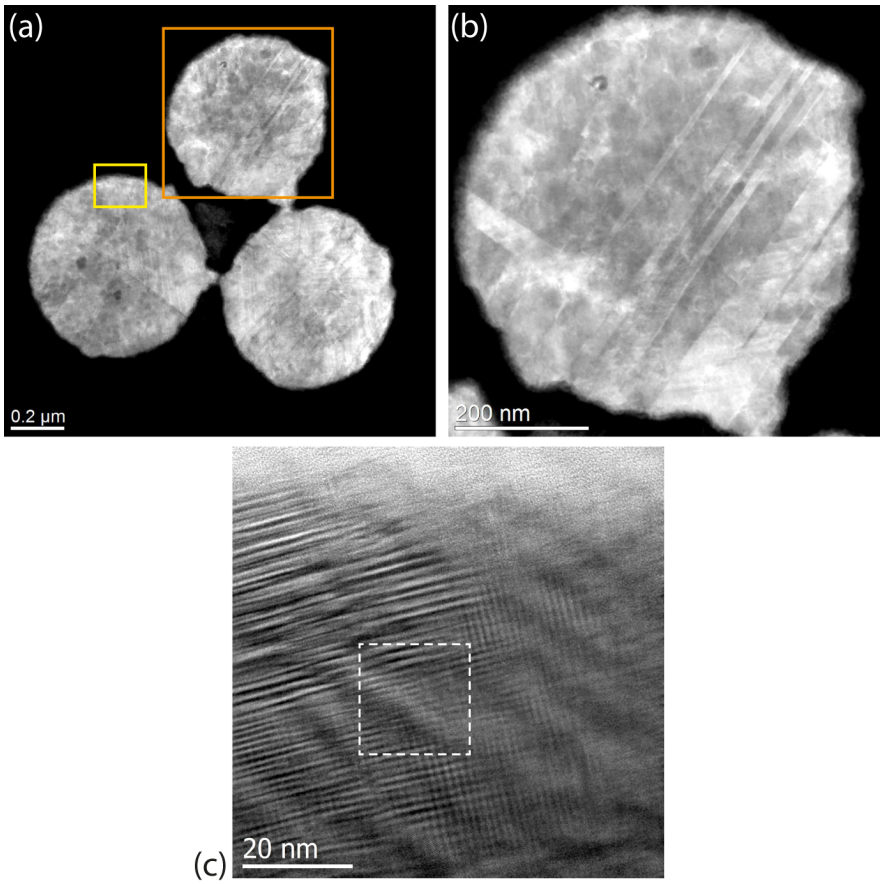

Fig. 5.5 (a) STEM-HAADF image of a group of three disks connected by small bridges. (b) Zoom of the disk marked by the orange square in (a): the twin variants of the martensitic microstructure are recognizable for their different contrast in the image. (c) Conventional TEM image showing a zoom of the region marked by the yellow rectangle in (a) showing the presence of areas, at the edges of the disks, in which the structural modulation lies in the plane of the disk.

If we observe at a higher magnification the region at the edge of the disk marked by the yellow rectangle in Fig. 5.5a, a martensitic phase with the structural modulation in the plane of the disk is observed, as visible in the conventional TEM image shown in Fig. 5.5c.

Moreover, from the high resolution TEM analysis of the region marked by the white dashed box in Fig 5.5c, reported in Fig 5.6a, the modulation is directly visible and confirmed by the FFT in which satellite spots are clearly identifiable. In the free-standing disks both the 7M and the 5M modulated

structures were observed.

As already pointed out in the previous Chapters, since the modulation occurs along the [110] direction of the pseudo-orthorhombic setting, the presence of the modulation in the plane of the disks is a direct proof of the orientation of the martensitic cell with the magnetization easy axis in the direction perpendicular to the disk plane.

Since this orientation of the martensitic cell was not observed neither in the continuous thin film or in the patterned film analysed by TEM in cross-sectional views, it can be ascribed to the relief of epitaxial constrain achieved after the etching of the Cr under-layer.

It is remarkable that this phase is observed at the edge of the disks where the thickness of the film decreases, while in the centre of the disks, where the thickness is constant, a monoclinic martensitic phase with 90° lamellae similar to the ones observed in the continuous thin film is observed. In in addition, small amounts of tetragonal phase are also observed, probably due to a damaging of the disks induced by the sputtering process. In Fig. 5.6b two diffractograms showing the diffraction spots of monoclinic and tetragonal phases observed in the 90° lamellae are shown.

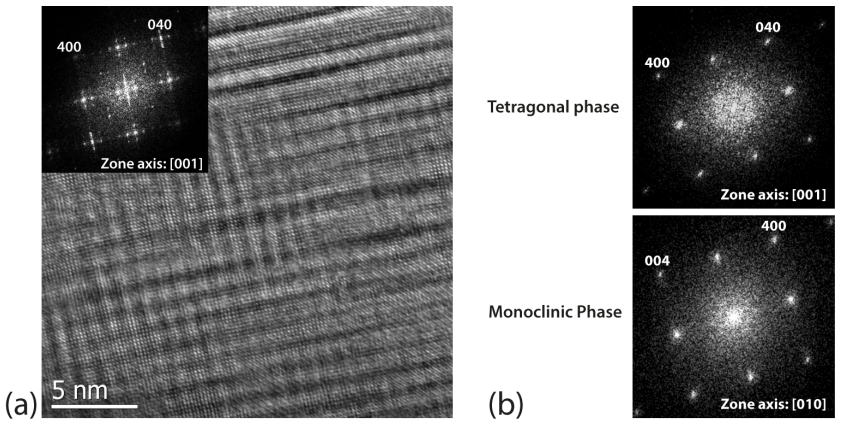

Fig. 5.6 (a) HREM image taken in the white dashed square drawn in Fig. 5.5c. In these regions the easy magnetization axis c is pointing in an out-of-plane direction. The satellites of the 7M modulated phase are visible in the FFT of the image. (b) Diffractograms demonstrating the presence of both monoclinic and tetragonal phases. (in small amounts) in 90° lamellae.

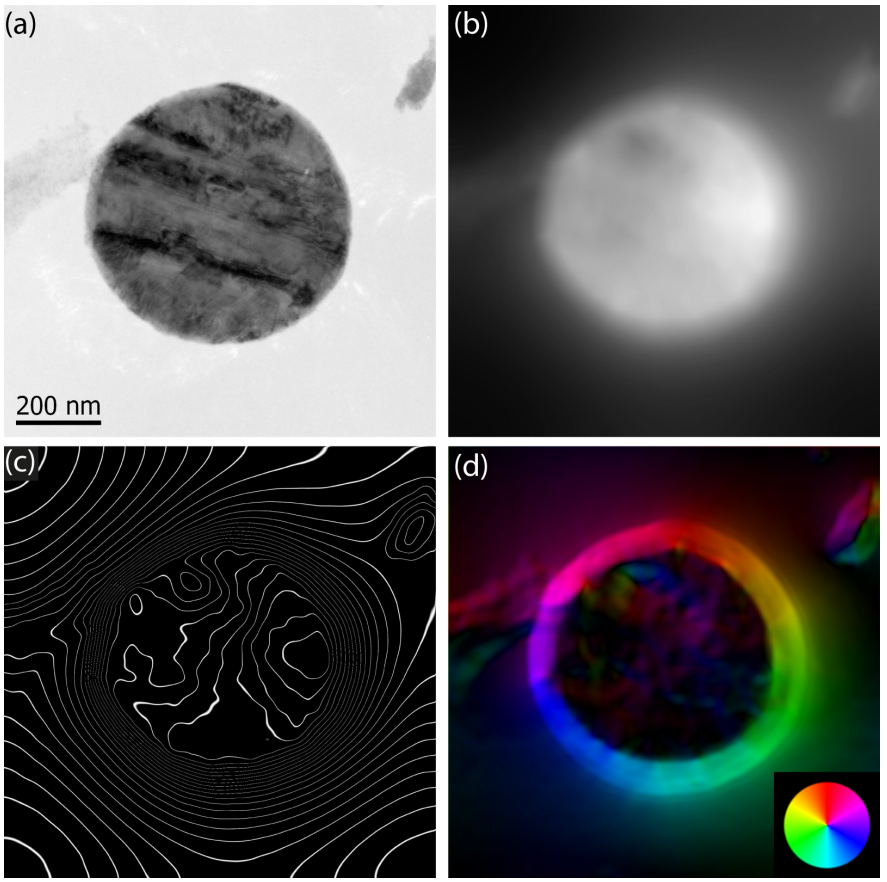

Fig. 5.7 Lorentz microscopy on a NiMnGa disk: (a) in-focus image, (b) restored phase, (c) contour lines of the phase (amplified 5x) showing magnetic flux lines and (d) corresponding magnetic induction colour map (the colour gives the direction of the magnetization vector, the saturation gives its intensity).

5.4.2 Magnetism unveiled by Lorentz microscopy

The magnetic properties of the NiMnGa free-standing disks have been investigated mainly by Lorentz microscopy, since the small amount of obtained material hampers any magnetic signal in magnetic measurements.

In order to analyse the magnetic properties of the disks by Lorentz microscopy, it has to be firstly noted that the employment of the separation

method to isolate the magnetic phase shift is strictly required to correctly characterize the system.

In Fig. 5.7a the in focus image of the Fresnel series acquired on a single NiMnGa disks is shown. The phase reconstructed by a single focal series and the relative contour lines map are shown, respectively, in Fig. 5.7b and 5.7c.

At a first glace, the obtained contour map could be wrongly interpreted as arising from a *onion*-like closure of the magnetization at the disk edge, as also emerges from the colour map shown in Fig. 5.7d of the in-plane component of magnetic induction, showing a *vortex-like* behaviour.

Acquiring a Fresnel series at the same values of defocus after turning upside-down the sample, the two contributions due to mean inner potential and magnetic phase shift can be isolated by the separation method. It is worth to remember that for complex structures constituted by differently oriented magnetic domains, as usually happens in martensitic structures, turning upside down the specimen represents the most convenient way in which the separation method can by performed, since an exact reversal of the magnetization can not be obtained by simply applying a magnetic field to the specimen.

A Lorentz microscopy characterization performed applying the separation method on the same disk shown in Fig. 5.7 is shown in Fig. 5.8. The disk, as already said, presents a martensitic microstructure with some regions in which the structural modulation appear in the plane of the disk. These regions, as proven by the HRTEM analysis previously shown, are characterized by a different orientation of the unit cell with the easy axis of magnetization (c axis) along a direction perpendicularly to the plane of the disk. A dashed line in Fig. 5.8a marks one of these regions. The enlargement, shown in Fig. 5.8d, demonstrates a contrast arising from the modulation in the plane of the disk.

In Fig. 5.8b and c the mean inner potential and the magnetic phase shift are shown, respectively. As can be seen from the mean inner potential, there is a clear side effect at the edge of the disk on a region with a width of 65 nm, producing a rapid decrease to zero of the MIP. The extension width of this

annular region is in good agreement with the length scale on which the disk thickness drop down to zero at the edge of the disks, as can be seen in Fig. 5.2b.

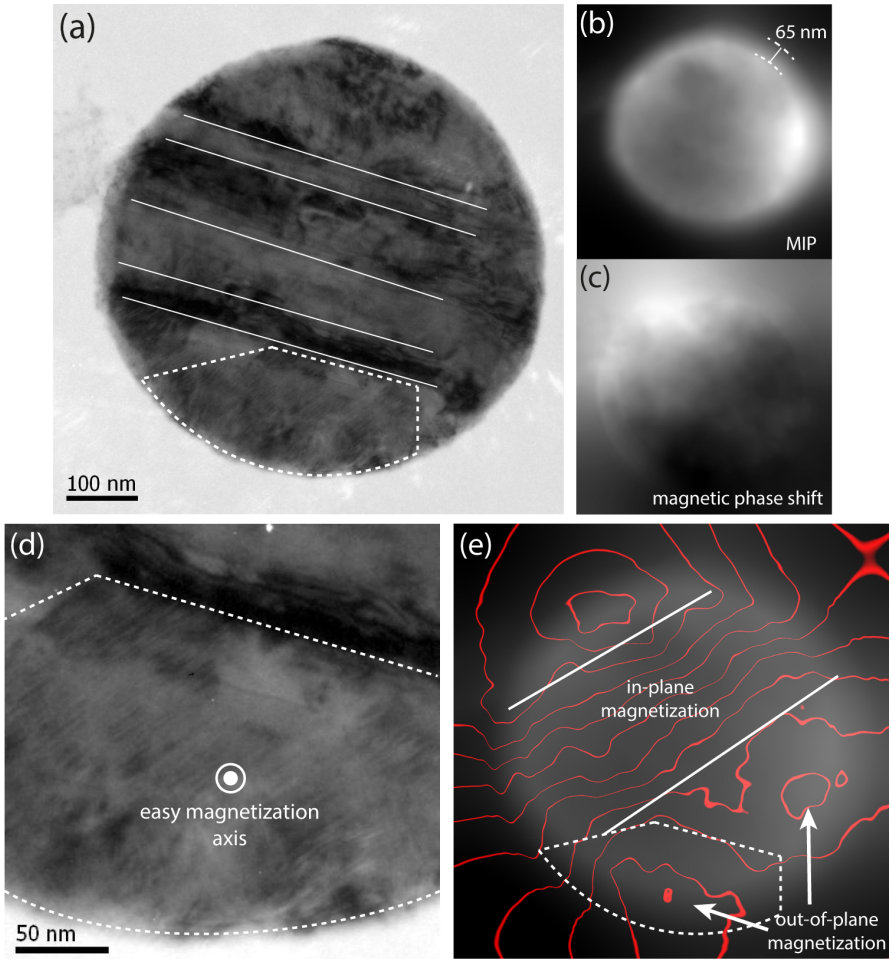

Fig. 5.8 Lorentz microscopy performed on the same disk shown in Fig. 5.7 by applying separation method. (a): in-focus image, in which a zone displaying the structural modulation in the plane of the disk is highlighted by a dashed line. The boundaries between 90° twinned domain are marked by continuous lines. (b), (c): mean inner potential and magnetic phase shift, respectively. (d) Enlargement of the area in which structural modulation is visible. (e) Contour lines (of the phase amplified 15x) superimposed to the mean inner potential: the most part of the disk shows an in-plane magnetization, unless for the areas where the modulation is in the plane of the disk (the same area marked in (a) is highlighted as example).

As previously introduced in Section 1.4.4.1, in fact, if the composition of the material does not change the mean inner potential contribution is related to the thickness of the specimen. Moreover, this is a further demonstration that the MIP contribution is the dominant one in the phase retrieved by a single focal series and effects due to thickness change at edges can induce to wrong interpretations of the phase image. The thickness can be considered constant only at the centre of the disk and the edge effects can induce to a misleading interpretation of the experimental data obtained by Lorentz microscopy.

In Fig. 5.8e the contour map obtained by the magnetic phase shift is plotted superimposed to the mean inner potential. The map demonstrates that the central part of the disk, in which 90° lamellae are seen in the in focus image (Fig. 5.8a), shows an in-plane magnetization, oriented approximately at 45° with respect to the boundaries between the domains (in good agreement with the structural orientations in the variants with 90° lamellae, as described in the previous Chapters). On the contrary, the areas where the modulation is observed in the plane of the disk (the area marked by the dashed line can be considered as an example) show an out of plane component of the magnetization, in agreement with the structural analysis.

5.5 Martensitic phase transformation in NiMnGa disks

5.5.1 Effects of phase transformation on martensitic crystal structure

The martensitic phase transformation in the free-standing nano-disks has been investigated by a TEM analysis in function of temperature. The panel shown in Fig. 5.9 summarizes the temperature evolution of the crystal structure and martensitic microstructure of a NiMnGa disk when the temperature is raised from RT up to 513 K and then cooled down again at RT in presence or absence of an applied magnetic field.

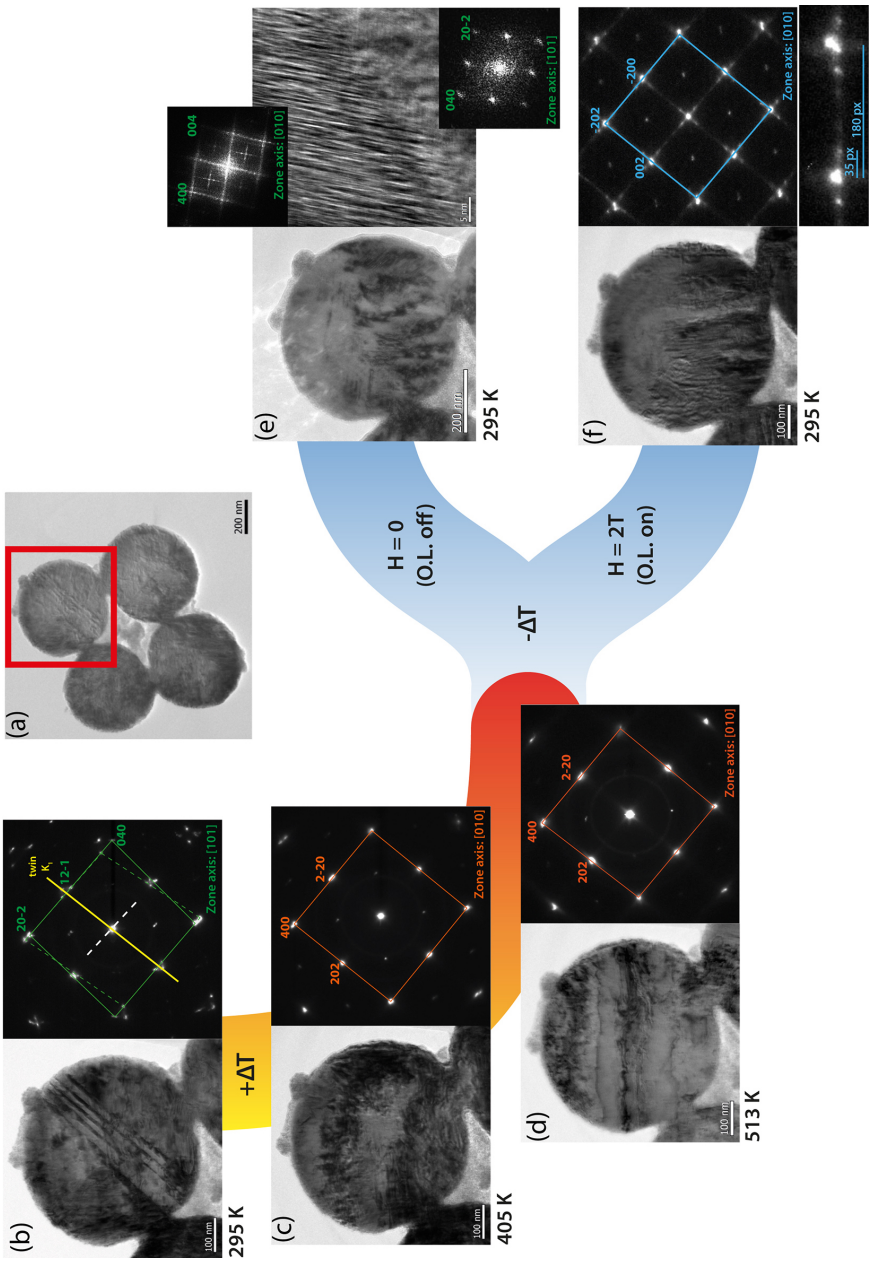

Fig. 5.9 TEM structural characterization as a function of temperature on the disks shown in (a). The behaviour of the disk marked by the red square is shown for different temperature: (b) 295K, (c) 405K, (d) 513K, (e) and (f) 295K. (e) and (f) are obtained after cooling down the sample to RT respectively in absence or presence of an applied magnetic field generated by the O.L. of the microscope (H = 2T).

The crystal structure of the martensitic phases displayed during this TEM experiment will be described using the monoclinic setting, in order to keep track of the differences with respect to the cubic austenitic phase.

It must be underline, moreover, that the temperatures given for each step of the cycle are the values detected by the thermocouple mounted on the TEM heating holder and may not exactly correspond to the effective temperature of the sample, since the thermal contact between the disks deposited on the carbon film of the TEM grid and the holder is not optimal and a poor thermal conduction is possibly achieved.

Starting from the group of NiMnGa disks shown in Fig. 5.9a, the behaviour of the system is discussed describing what happens to the structure of the disk in the red box, that is exemplificative for the phase transformations that all the NiMnGa disks undergo during the temperature cycle.

In Fig. 5.9b a low magnification bright field TEM image, together with the SAED electron diffraction pattern obtained at RT from the considered disk, is shown. As can be easily verified from electron diffraction and accordingly to the morphology visible in the image, the martensitic structure of the system is mainly constituted by 90° lamellae corresponding to an in-plane orientation of the magnetization easy axis. It must be worth to recall that the easy magnetization axis, corresponding to the c axis of the pseudo-orthorhombic setting, is along the [010] direction of the monoclinic cell. The in plane orientation of the easy axis is hence demonstrated by the diffraction spots of (040) planes visible in the DP of the disk. The reciprocal lattice cells of the primary and the twinned crystal are marked with continuous and dashed green lines, respectively. The K_1 element (plane) of the twin is schematized in the planar view of the disk by the yellow line drawn superimposed to the DP; the type-II character of the twinning plane is evidenced by the presence of a mirror plane (sketched by the white dashed line) in the reciprocal lattice, normal to the K_1 plane, accordingly to the considerations given in Chapter 4 about the symmetry elements related to a type-II twin.

Increasing the temperature up to 405K (Fig. 5.9c), a phase transformation is

observed and clearly demonstrated by the remarkable changes in the diffraction pattern of the disk. In particular, the evolution of the diffraction pattern to higher symmetry geometry is a proof of the phase transition toward the high-symmetric cubic austenitic phase. The phase transition is complete in the entire specimen at 513 K (Fig. 5.9d).

Since the TEM specimen mounted on the holder is placed among the polar pieces of the objective lens (O.L.) of the microscope, during the cooling down of the temperature back to RT it is possible to investigate the behaviour of the system in presence or absence of an applied longitudinal magnetic field by turning on or switching off the O.L., respectively.

If the cooling down process is carried out with the objective lens turned off, a new martensitic phase is obtained (Fig. 5.9e) characterized by both the two possible orientations of the monoclinic cell of the martensitic phase, i.e. with the easy axis both in the plane of the film and in an out-of-plane direction, as confirmed by the HREM image and FFTs relative to the two different zones visible in the image. In agreement to the results reported by Thomas et al. [17], the experimental observation, after a heating-cooling cycle (in which the austenitic phase is restored during the heating), of a new martensitic phase similar to the one observed at the beginning of the thermal treatment, but characterized by a different twin variants distribution, can be described as a *stray-field-induced microstructure* (SFIM). Therefore, this non-conventional thermal-actuation mechanism demonstrated by Thomas for free-standing NiMnGa thin films is active also in the confined martensitic nano-disks.

System	Lattice parameters
Monoclinic (5M) (I2/m)	a' = 4.23 Å, b' = 5.6 Å, c' = 4.18 Å ß = 90.9
Cubic (austenite) (Fm-3m)	a = 5.80 Å

Table 5.1 Experimental lattice parameters for the monoclinic 5M and cubic austenitic phases observed during the temperature cycle.

On the contrary, if the O.L. is turned on a static magnetic field with amplitude H = 2T is applied along the vertical direction of TEM column and, hence, in the perpendicular direction with respect to the plane of the disks. Cooling down the sample in such magnetic field is effective in inducing a martensitic phase with a well-defined orientation. In fact, as shown in Fig. 5.9f, a new martensitic phase characterized by a preferential orientation of the easy magnetization axis parallel to the direction of the applied magnetic field is generated in the disks. This remarkable result permits to conclude that the MIM (magnetically induced martensite, discussed in Section 1.3) effect survives at the lateral confinement of the martensitic structure and is still displayed in the free-standing 1D system.

The crystal structures and the experimental lattice parameters for the observed monoclinic 5M and austenitic phases visualized during the different steps of the temperature cycle are reported in Table 5.1.

5.5.2 Effects of phase transformation on magnetic properties

In order to study the effects of martensitic phase transformation on the magnetic properties of NiMnGa disks, a Lorentz microscopy investigation has been carried out analysing the magnetic properties of the same NiMnGa disks before and after the described temperature cycle, performing the thermal cycle with the objective lens of the microscope turned off. The analysis has been carried out on the group of three disks shown in Fig. 5.5a, which displayed a recognizable martensitic microstructure.

The in focus Lorentz image is shown in Fig 5.10a. The contour map obtained from the magnetic phase shift, superimposed to the mean inner potential, obtained by the Lorentz microscopy experiments performed on the starting RT martensitic configuration is shown in Fig. 5.10b. The same analysis performed on the disks after the thermal cycle is reported in Fig 5.10c.

The already described effect (observed in the structural measurements) of

the thermal cycle, able to induce in the free-standing disks a new martensitic phase with a different twin variants distribution, is evident. Also by the Lorentz microscopy characterization, in fact, we have a proof of the rearrangement of the twin variants that occur when the austenitic phase is restored.

The contour lines, which represent the magnetic induction flux lines, reported in Fig. 5.10c indicate that the produced martensitic phase displays a better closure of the magnetic flux lines among the magnetic domains, with respect to the martensitic phase derived from the film.

In agreement to what reported by Thomas for a free standing film, also in the laterally confined NiMnGa structures here considered, i.e. NiMnGa nano-disks, the twin variants configuration generated by the stray field induced microstructure is the one that is most effective in reducing the magnetostatic energy of the system.

On the basis of the behaviour of the investigated system, it is reasonable to think that a further reduction of the lateral size of the disks, achievable by using polymeric capping spheres with a lower size, could enable to obtain a single domain magnetic state.

5.6 Actuation mechanisms active in NiMnGa disks

The described experimental results show that the effect of lateral confinement in martensitic NiMnGa disks is to induce a modification in the martensitic structure, with the appearance, at their edges, of twin variants with the easy magnetization axis directed normal to the plane of the disks.

The reported TEM measurements demonstrate that among the three actuation mechanisms (memory shape effect, MIM and MIR), only two are active in the martensitic NiMnGa disks, being the MIR mechanisms hindered probably by the localized defects induced by the sample preparation (e.g. non-modulated tetragonal phase). No experimental evidence of MIR effect was in fact observed in Lorentz microscopy measurements (not reported here) with an apply magnetic field.

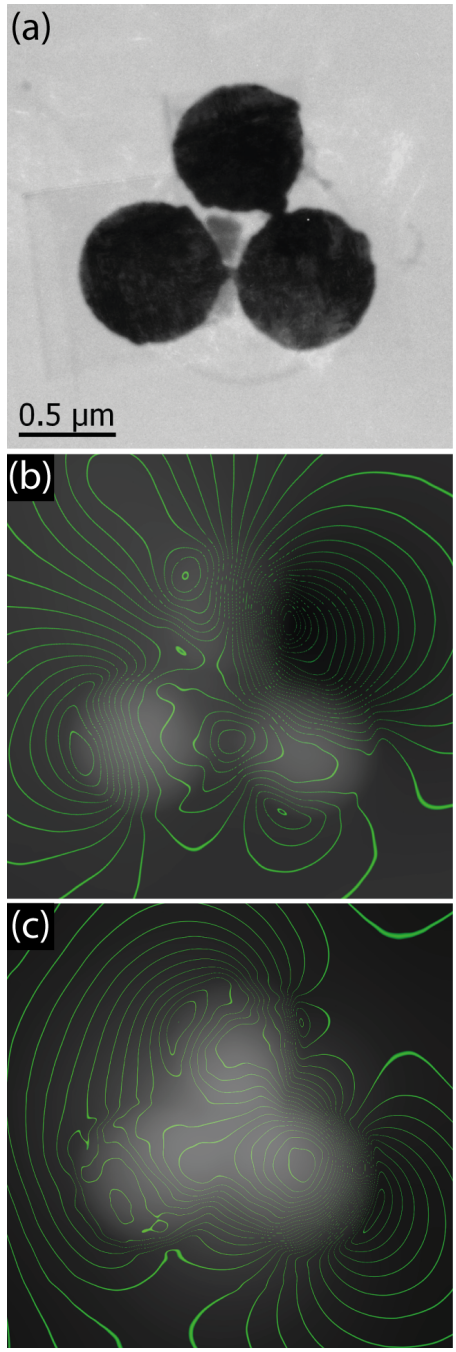

Fig. 5.10 (a) In focus Lorentz image of the group of three disks previously shown in Fig. 5.5a. Phase contours (the phase is amplified 10x) superimposed to mean inner potential as obtained by the Lorentz microscopy experiments performed respectively before (b) and after (c) the thermal cycle.

Concerning other actuation mechanisms, from temperature dependent measurements it has been demonstrated that the stray field induced microstructure and the MIM effect are still present and survive to the lateral confinement of the martensitic structure.

From the analysis of the images acquired at different temperatures, the area occupied by the ensemble of four disks shown in Fig. 5.9a can be calculated. The change in the planar area occupied by the disks can give a rough estimation about the relative strength of the active actuating mechanisms.

In particular, for the observed transition from the initial martensitic phase toward the cubic austenitic phase an increase in the area $\Delta A = + (4.3 \pm 0.5)\%$ can be estimated.

The analysis of the images acquired before and after the transition, performing a thermal cycle in which no magnetic fields are applied on the specimen, permit to estimate an increase in the area of the martensitic product phase $\Delta A = - (1.2 \pm 0.3)\%$. This effect is probably due to the increase of the amount of twin variants with the short easy axis in the plane of the film, in agreement to what reported for free-standing films [17] and confirmed by the Lorentz microscopy investigation reported in Section 5.5.2.

If the cooling down of the austenitic phase is carried out with the O.L. of the microscope on, and hence applying a magnetic field on the specimen, the establishing of a 5M phase with its easy axis preferentially oriented perpendicular to the plane of the disk induces a change in the area of the disks which is around $\Delta A = + (0.9 \pm 0.2)\%$.

The obtained results demonstrate that the shape memory effect related to the phase transition can be considered the most efficient actuating mechanisms for the described system. The lower efficiency observed for other mechanisms, as well as the absence of MIR effect, can be ascribed to the presence of defects induced by sample preparation, which have been confirmed by the structural analysis carried out by high resolution TEM and electron diffraction previously reported.

References

[1] B. Weber, S. Mahapatra, H. Ryu, S. Lee, A. Fuhrer, T. C. G. Reusch, D. L. Thompson, W. C. T. Lee, G. Klimeck, L. C. L. Hollenberg and M. Y. Simmons, *Science*, 2012, 335, 6064, 64-67.

[2] P. Smaglik, *Nature*, 2002, 418, 4-6.

[3] H. Tong, S. Ouyang, Y. Bi, N. Umezawa, M. Oshikiri and J. Ye, *Adv. Mater.*, 2012, 24, 2, 229-251.

[4] J. A. Scholl, A. L. Koh and J. A. Dionne, *Nature*, 2012, 483, 421-427.

[5] L. Cao, J. S. White, J.-S. Park, J. A. Schuller, B. M. Clemens and M. L. Brongersma, *Nat. Mater.*, 2009, 8, 643-647.

[6] L. Kuipers, *Nat. Photonics*, 2014, 8, 9-10.

[7] N. Guo, W. Hu, L. Liao, S. Yip, J. C. Ho, J. Miao, Z. Zhang, J. Zou, T. Jiang, S. Wu, X. Chen and W. Lu, *Adv. Mater.*, 2014, 26, 48, 8232.

[8] K. Uetsuki, P. Verma, P. Nordlander and S. Kawata, *Nanoscale*, 2012, 4, 5931-5935.

[9] M. J. Sailor and J.-H. Park, *Adv. Mater.*, 2012, 24, 28, 3779-3802.

[10] A. V. Boris, Y. Matiks, E. Benckiser, A. Frano, P. Popovich, V. Hinkov, P. Wochner, M. Castro-Colin, E. Detemple, V. K. Malik, C. Bernhard, T. Prokscha, A. Suter, Z. Salman, E. Morenzoni, G. Cristiani, H.-U. Habermeier and B. Keimer, *Science*, 2011, 20, 332, 6032, 937-940.

[11] M. Cahay, *Nat. Nanotech*., 2015, 10, 21–22.

[12] G. Hönig, G. Callsen, A. Schliwa, S. Kalinowski, C. Kindel, S. Kako, Y. Arakawa, D. Bimberg and Axel Hoffmann, *Nat. Comm.*, 2014, 5, 5721.

[13] T. Jungwirth, J. Wunderlich and Kamil Olejník, *Nat. Mater.*, 2012, 11, 382-390.

[14] G. Chen, J. Seo, C. Yang and P. N. Prasad, *Chem. Soc. Rev.*, 2013,42, 8304-8338.

[15] J. San Juan, M. L. Nó, and C. A. Schuh, *Adv. Mater.*, 2008, 20, 2, 272-278.

[16] C. A. Jenkins, R. Ramesh, M. Huth, T. Eichhorn, P. Pörsch, H. J. Elmers, and G. Jakob, *Appl. Phys. Lett.*, 2008, 93, 234101

[17] M. Thomas, O. Heczko, J. Buschbeck, Y. W. Lai, J. McCord, S. Kaufmann, L. Schultz and S. Fähler, *Adv. Mat.,* 2009, 21, 3708.

[18] P. Tiberto, L. Boarino, F. Celegato, M. Coisson, E. Enrico, N. de Leo, F. Vinai, P. Allia, *J. Nanopart. Res.*, 2011, 13, 9, 4211-4218.

Conclusions

In this doctoral thesis nanostructured magnetic materials have been studied by advanced transmission electron microscopy techniques, with emphasis on magnetite NPs for biomedical applications and NiMnGa shape memory alloy thin films and nanodisks.

The investigation of magnetic NPs was finalized to the comprehension of new phenomenological effects arising in the nanostructured material due to the deviation from the ideal superparamagnetic regime, being this deviation able to affect the NPs properties and hence to significantly alter the system performance in magnetic hyperthermia applications.

The characterization of NiMnGa films and disks was focused on the study of the effects of growth parameters and lateral confinement on the structure and magnetism of the martensitic phase. By properly tuning these parameters, in fact, it is possible to achieve an extraordinary control on the martensitic phase

from the atomic to the micro length scale and to tailor the thermoelastic and magnetoelastic properties of the material.

The conducted work produced new and remarkable results concerning the correlation between the microstructure of these systems and their magnetic/functional properties, from the nano to the micro and macro scales. In detail, the main results achieved during the doctoral work can be summarized as follows:

i. Employment of Lorentz microscopy to investigate the role of dipolar interactions in hyperthermia of magnetic NPs.

Magnetic NPs in the superparamagnetic state are suitable for both diagnostic and therapeutic approaches. In particular, the magnetic hyperthermia can be effectively employed to locally induce cancer cell death. In real systems, clusters of magnetic NPs with different sizes can form and the dipolar interactions that arise among NPs can strongly influence the heating ability of the colloidal suspensions. The effect of the dipolar interactions on the hyperthermic behaviour of these complex systems, however, is still not completely understood.

A better understanding of the heat generation mechanisms for magnetic NPs systems was achieved investigating their different degrees of interaction by Lorentz microscopy. With this holographic technique, in fact, it is possible to visualize and map the inter-particle interactions and to develop reliable models on the power losses mechanisms for different NPs aggregates. As a result, a deeper understanding of the interaction effects on the performance of different nanoparticles suspensions as hyperthermic mediators has been obtained.

All the TEM results were supported and complemented by magnetic characterization, which unequivocally proves that magnetic interactions play a fundamental role in the efficiency of the NPs suspensions as hyperthermic

mediators. Thanks to Lorentz microscopy the magnetic properties at the macroscopic scale were correlated to the different degrees of interaction at the nanoscale and a model for the power loss mechanisms in different aggregates was developed.

ii. Employment of advanced TEM techniques to study the effects of epitaxial strain and film thickness in the twin variants formation in NiMnGa martensitic thin films.

In martensitic thin films, the martensitic phase transition gives rise to a poly-twinned system characterized by a complex microstructure, in which two families of twin variants with different magnetic anisotropies can be displayed. The use of different substrates/buffer layers and film thicknesses can significantly modify the martensitic microstructure and consequently alter the functional properties of the obtained thin films.

Combining HRTEM, SAED and electron holography, NiMnGa thin films with thicknesses in the range 50-100 nm and grown on different substrates (i.e. MgO, MgO/Cr buffer layer) were fully characterized, in plan and cross sections geometries. The structural and magnetic properties at the nanoscale (i.e. in each martensitic twin variant) obtained by TEM analysis were compared to the morphological, structural and magnetic properties on the micrometric scale, obtained by AFM, MFM and XRD.

The described results demonstrate that the different substrates affect the strain state of the austenitic phase. Accordingly to the experimental data, a thickness dependent model based on the strain states of the austenitic phase is proposed to describe the selective twin variants formation in the martensitic phase. The model represents a powerful tool to selectively control the twin variants formation in martensitic thin films and therefore to actively tailor their magnetic structure and functional properties.

iii. A multi-scale TEM characterization to study the role of microstructure on magnetically induced reorientation of twin variants in NiMnGa 200 nm thin films

In NiMnGa alloys giant strains, whose values are one order of magnitude higher than the typical ones achievable by magnetostriction and state-of-the-art piezoelectric effects, can be obtained by a magneto-mechanical effect based on MIR process. The possibility of exploiting the martensitic distortions to create tiny machines, keeping a simple and smart design, makes these materials particularly appealing for the integration in active microsystems able to work at high actuation frequencies. However, up to now very limited MIR effects were found in NiMnGa thin films and a full comprehension and exploitation of the effect is still lacking.

In this doctoral work an in-depth TEM characterization of NiMnGa alloys thin films 200 nm thick, displaying different MIR effects, was carried out. In particular, by combining different advanced TEM techniques such as HAADF imaging, HRTEM with the comparison of the experimental images to the simulated ones, SAED and electron holography, it is possible to correlate the crystal structure to the twin variants configurations and the magnetism inside each twinning domain of the film. The different characterized thin films and the peculiar aspects of the MIR effects displayed at the macroscopic scale have been successfully related to the observed martensitic microstructures at the microscopic scale; moreover, the experimental results strongly indicate that, at the nanoscale, the twin boundaries involved in the MIR process are the type-II twins in twin plates containing 90° lamellae.

In additon, a model based on TEM results was suggested to explain the formation of an anisotropic microstructure in one of the 200 nm thick NiMnGa films grown on MgO/Cr. All the results achieved by transmission electron microscopy are supported by the findings obtained by XRD, AFM and MFM on larger lengths scale. Since the peculiar anisotropic microstructure observed in the film is at the base of the displayed huge and anisotropic MIR effect, the

proposed model is crucial for the engineering of the martensitic microstructure and for achieving substantial values of MIR in constrained thin films.

iv. Effects of the reduction of dimensionality in martensitic NiMnGa systems investigated by TEM: from thin films to nano-disks

After gaining a good understanding of the microstructure of 2D NiMnGa martensitic films, in relation to the most important properties concerning their applications, the possibility to obtain new functional properties by scaling down the dimensionality of these systems was explored. To this aim, the in-depth TEM characterization was extended to a novel class of nanostructures, i.e. NiMnGa nano-disks, to investigate their structural and magnetic properties and the effect of the lateral confinement on the martensitic phase.

By employing HRTEM, Lorentz microscopy and electron diffraction analysis as a function of temperature, it was found that the martensitic actuation mechanisms remain active with the reduction of the dimensionality of the system. This important finding opens great perspectives regarding the potential applications of such multifunctional martensitic nanostructures.

Acknowledgments

The research activities have been financed by Consorzio SPINNER within the project "SPINNER 2013 - Nanoscienze: materiali e strategie emergenti per tecnologie sostenibili", coordinated by Prof. Elisa Molinari.

First of all, I would like to thank the *Instituto dei Materiali per l'Elettronica ed il Magnetismo* of the *National Research Council* (IMEM-CNR) in Parma for hosting my Ph.D. activities and my supervisors, Dr. Lucia Nasi and Dr. Giancarlo Salviati, for giving me such opportunity.

I would like to express my heartfelt gratitude to Dr. Vincenzo Grillo for its constant and important support and for giving me countless teachings concerning all aspects of transmission electron microscopy.

A special thank goes to Dr. Cesar Magén, of the Institute of Nanoscience of Aragon (INA), for giving me access to the facilities of the *Laboratorio de Microscopías Avanzadas* (LMA) at the *Institute of Nanoscience of Aragon* (INA) of Zaragoza and offering me lots of precious teachings in the field of electron holography, Lorentz microscopy and aberration-corrected electron microscopy.

I want to extend sincere thanks to all the people of the electron microscopy group of the IMEM-CNR institute, in particular to Dr. Francesca Rossi and Dr. Giovanni Bertoni for their great availability in collaborating on experimental

activities as well as in spending jovial moments, without with these three years would not have been the same.

I want to thank Dr. Franca Albertini, as well as the other people of the magnetic materials group in the IMEM-CNR institute (Dr. Paolo Ranzieri, Dr. Simone Fabbrici, Dr. Francesca Casoli, Dr. César de Julian Fernandez, Dr. Valentina Chiesi, Dr. Roberta Ciprian and Dr. Lara Righi), for the fruitful discussions about magnetic nanostructured materials and for the great support offered during my first approach to electron holography and Lorentz microscopy techniques, never exploited before at the IMEM institute. I am also grateful to Dr. Paola Tiberto, Dr. Federica Celegato and Dr. Gabriele Barrera of *istituto Nazionale di Ricerca Metrologica* (INRIM) for the TEM specimens preparation by FIB.

I want to thanks Dr. Elena Bedogni for the strong scientific collaboration and the sincere friendship built up in these three years; a sincere thank also to Dr. Antonio Mega and Dr. Franca Bigi for the collaboration in the synthesis of the magnetic nanoparticles.

I would like to thank Dr. Claudio Ferrari and Dr. Elisa Buffagni for the precious contribution in the XRD characterizations on NMnGa thin films. A unique acknowledge goes to Dr. Elisa Bonnini, not only for collaborating in XRD measurements but also for friendly supporting me in all the difficult moments.

Grazie ai miei genitori, Fiorella e Antonio, e a mia sorella Monica, per il prezioso supporto fornito in tutti questi anni.

Infine grazie a tutti gli amici che mi sono stati vicini in questi tre anni, con cui ho trascorso spensierati momenti e indimenticabili vacanze. Un particolare grazie a Bianco, Fana, Stef, Chiara, Nenno, Molo, Taor, Cri, Martina, Gio e Zak e gli amici dei Crazy Kiwis!

Muchas gracias también a los amigos en Zaragoza: Luc, Céline, Rongrong, Bastian, Pilar, Luis, Lorena y Oscar!